Respiratory motion correction in PET/CT imaging

Schleyer, Paul

Awarding institution:
King's College London

Respiratory motion correction in PET/CT imaging

Paul Schleyer

Division of Imaging Sciences and Biomedical Imaging

King's College London

A thesis submitted for the degree of

Doctor of Philosophy

2012

Abstract

In dual modality PET-CT imaging, respiratory motion can introduce blurring in PET images and create a spatial mismatch between the PET and CT datasets. Attenuation correction errors can result from this mismatch, which can produce severe artefacts that potentially alter the clinical interpretation of the images. Various approaches of reducing these effects have been developed. Many involve respiratory gated acquisitions which generally require a measure of the respiratory cycle throughout imaging.

In this work, a retrospective respiratory gating technique was developed for both PET and CT which extracts the respiratory cycle from the acquired data itself, removing the requirement for hardware that measures respiration. This data-driven gating method was validated with phantom and patient data, and compared with a hardware based approach of gating. Extensions to the method facilitated the gating of multi-bed position, 3D clinical PET scans. Finally, 60 Ammonia cardiac PET/CT images were used to compare several different approaches of reducing respiratory induced attenuation correction errors and motion blur.

The data-driven respiratory gating method accurately substituted a hardware based approach, and no significant difference was found between images gated with either methods. Gating 11 clinical 3D whole body PET images validated the extended data-driven gating methods and demonstrated successful combination of separate PET bed-positions. All evaluated approaches to reduce respiratory motion artefacts in cardiac imaging demonstrated an average improvement in PET-CT alignment. However, cases were found where alignment

worsened and artefacts resulted. Fewer and less severe cases were produced when the 4D attenuation correction data was created from a 3D helical CT and PET derived motion fields. Full motion correction produced a small effect on average, however in this case no detrimental effects were found.

Acknowledgements

A lot of people contributed in some way to this thesis. Primarily, my supervisors. Prof. Paul Marsden enthusiastically drove this work to completion and on occasions stopped it from running off on obscure tangents. Prof. Michael O'Doherty, my second supervisor, not only facilitated this entire project, but also steered it from the perspective of a clinician.

Kris Thielemans provided brilliant guidance, much needed encouragement and an enourmous amount of technical assistance throught this work. Much of the clinical perspective came from Sally Barrington, who helped considerably with the cardiac section. Sally also went to great efforts to find patients, as did Vikki Warbey. The cardiac images were thanks to Geraint Morton, and the thoracic oncology multi-disciplinary team at Guy's and St. Thomas' recruited the lung cancer patients.

All patient imaging was performed by the team at the PET Imaging Centre, St Thomas' Hospital, particularly Stacey Baker, Joemon John and Armidita Jacob. The group went to great lengths to ensure patients were scanned using irritatingly tedious protocols.

Marc Modat from UCLH helped imensely (and immediately!) with the brilliant Nifty-reg package. A lot of technical help with the GE research tools and scanner hardware came from the engineeers at GE Healthcare, largely from Steve Ross and Chuck Stearns.

The entire PET Physics group at KCL Imaging Sciences, particulalry Lefteris Livieratos for being exceptionally (and helpfully) critical, Charalampos Tsoumpas for helping with 3D normalisation, Edward Somer for registration help, Joel Dunn for help with statistics, and Jane Mackewn for her undying support.

Finally, it seems almost customary to thank and acknowledge one's spouse; almost every thesis appears to do so. And now I know why.

Without the tireless support and encouragement of Michelle, an eternally incomplete thesis would remain. She also explained myocardial anatomy and proof read much of this dissertation. Good catch.

This thesis presents independent research awarded under NEAT (New and Emerging Applications of Technology), part of the Invention for Innovation (i4i) programme of the National Institute for Health Research (NIHR). The views expressed in this publication are those of the author and not necessarily those of the NHS, the NIHR or the Department of Health.

Publications arising from this work

Paul Schleyer, Michael O'Doherty, Victoria Warbey, Sally Barrington, and Paul Marsden. Data-driven respiratory gating for PET and CT imaging *Nuclear Medicine Communications (Abstract)*, 29(5):470, 2008.

Paul Schleyer, Michael O'Doherty, Victoria Warbey, Sally Barrington, and Paul Marsden. Retrospective data driven respiratory gating for PET/CT. *Society of Nuclear Medicine Annual Meeting Abstracts*, 49(Supplement 1):60, 2008.

Paul J Schleyer, Michael J O'Doherty, Sally F Barrington, and Paul K Marsden. Retrospective data-driven respiratory gating for PET/CT. *Physics in medicine and biology*, 54(7):1935–50, April 2009.

Paul J Schleyer, Michael J O'Doherty, and Paul K Marsden. Extension of a data-driven gating technique to 3D, whole body PET studies. *Physics in medicine and biology*, 56(13):3953–65, July 2011.

Paul Schleyer, Michael O'Doherty, and Paul Marsden. Data driven respiratory gating applied to whole body, 3D clinical FDG PET acquisitions. *Society of Nuclear Medicine Annual Meeting Abstracts*, 52(Supplement 1):152, 2011.

Paul Schleyer, Michael O'Doherty, Sally Barrington, Geraint Morton, and Paul Marsden. A comparison of approaches to reduce respiratory motion artifacts in NH3 PET/CT imaging. *Society of Nuclear Medicine Annual Meeting Abstracts*, 53(Supplement 1):484, 2012.

Contents

Contents **7**

List of Figures **11**

1 Introduction **20**

1.1 Background 20

1.1.1 PET tracers 21

1.1.2 PET 22

1.1.2.1 Attenuation 24

1.1.2.2 Randoms and scatter 26

1.1.2.3 2D and 3D PET 27

1.1.2.4 Sinogram and listmode formats 29

1.1.2.5 PET Imaging modes 30

1.1.2.6 Image reconstruction 33

1.1.3 Computed Tomography 35

1.1.3.1 CT Imaging modes 36

1.1.3.2 Imaging parameters and dosimetry 37

1.1.4 Dual modality PET/CT 39

1.1.4.1 CT based PET attenuation correction 39

1.1.4.2 PET/CT acquisition 42

1.1.5 PET/CT accuracy 43

1.2 Respiratory Motion 45

1.3 Respiratory gating PET/CT acquisitions 46

1.3.1 Measuring respiration 46

1.3.1.1 Hardware methods 47

1.3.1.2 Data-driven methods . . . 48
1.3.2 Gating approaches . . . 51
1.3.2.1 Gated CT limitations . . . 53
1.4 Respiratory motion and PET/CT Imaging . . . 55
1.4.1 Cardiac PET/CT Imaging . . . 59
1.5 Approaches to reduce respiratory motion in PET/CT . . . 59
1.5.1 *Type I* - Breath hold CT . . . 60
1.5.2 *Type I* - Shifted helical CT . . . 62
1.5.3 *Type I* - Slow rotation helical CT . . . 62
1.5.4 *Type I* - Averaged cine CT . . . 63
1.5.5 *Type II* - Selective PET acquisition . . . 64
1.5.6 *Type II* - Respiratory gating . . . 64
1.5.7 *Type II* - Pseudo gated CT . . . 66
1.5.8 *Type III* - Motion correction . . . 68
1.5.9 Summary . . . 70
1.6 Objectives of this work . . . 71

2 Data-Driven Respiratory Gating for PET/CT Imaging 73
2.1 Introduction . . . 73
2.2 Methods . . . 75
2.2.1 PET Data-Driven Gating technique . . . 75
2.2.1.1 Spectral analysis, mask generation and signal extraction . . . 75
2.2.1.2 Binning . . . 79
2.2.2 CT Gating . . . 79
2.2.2.1 Spectral Analysis - CT . . . 80
2.2.2.2 Binning - CT . . . 82
2.2.3 Phantom acquisition . . . 84
2.2.4 Patient Acquisition . . . 84
2.2.5 Parameter selection . . . 85
2.3 Results . . . 86
2.3.1 Phantom study . . . 86
2.3.2 Patient studies . . . 88

2.4 Discussion . . . 94
2.5 Conclusion . . . 101

3 Respiratory gating clinical 3D whole body PET images. 102
3.1 Introduction . . . 102
3.2 Methods . . . 103
3.2.1 3D PET . . . 104
3.2.2 Multi-bed PET . . . 104
3.2.3 Combining PET bed positions . . . 106
3.2.4 Reconstruction and Evaluation . . . 108
3.3 Results . . . 109
3.3.1 RPM comparison . . . 110
3.3.2 Combining bed positions . . . 110
3.3.3 Image evaluation . . . 112
3.4 Discussion . . . 114
3.5 Conclusion . . . 117

4 Comparing approaches to respiratory motion correction in NH_3 PET perfusion imaging 119
4.1 Introduction . . . 119
4.2 Methods . . . 121
4.2.1 Data-driven gating of NH_3 PET . . . 122
4.2.2 Attenuation Correction Methods . . . 123
4.2.3 Motion correction . . . 127
4.2.4 Evaluation . . . 129
4.2.5 Liver and myocardial edge . . . 133
4.3 Results . . . 134
4.3.1 Data-driven gated PET . . . 134
4.3.2 Gated and pseudo CT images . . . 136
4.3.3 PET - CT alignment . . . 137
4.3.4 Cardiac wall profile analysis (non-motion corrected) . . . 138
4.3.5 Motion correction . . . 146
4.4 Discussion . . . 148

4.5 Conclusion 153

5 Conclusions **155**

5.0.1 Data-driven gating parameter selection 158

5.1 Future work 160

5.1.1 Dose reduction 160

5.1.1.1 Parameter optimisation 160

5.1.1.2 Restrict additional cine CT 161

5.1.1.3 Eliminate additional CT 162

5.2 Dual gating 163

5.3 PET/MR 164

5.4 Clinical significance and application 164

Bibliography **167**

List of Figures

1.1 A positron (e^+) and a neutrino (ν) are ejected from an atom that undergoes positron decay. Two 511 keV photons are produced when the positron annihilates with an electron (e^-). If both photons are detected within a set timing window, as determined by the coincidence timing processor, then a line of response is registered. 23

1.2 PET scanners are constructed from adjacent rings of detectors. Each detector block consists of an array of scintillating crystal coupled to photomultiplier tubes. 24

1.3 (a) A true coincidence produces an LOR that passes through the decay event. (b) Random events are produced from two independent decay events detected within the coincidence timing window. (c) Photon scatter can move the LOR such that it no longer passes through the decay event. 25

1.4 Both photons must reach a detector to identify a decay event. Here, the decay event occurred at point x in object with thickness L. The probability of attenuation depends only on L and the attenuation coefficient of the material. 26

1.5 Simplified illustration of 2D and 3D PET modes. In 2D mode, each detector only accepts LORs that correspond to the same or adjacent detector rings. In 3D mode, all LORs are accepted. . . . 27

1.6 In 2D mode, random events from external activity are blocked by the septa. Removing the septa increases the likelihood of randoms events. 28

1.7 In 3D mode, more scattered events can be detected by the scanner. 28

1.8 The polar coordinate system, (r, θ), used to define LORs in 2D PET mode. A line from the origin and normal to the LOR is created. θ is defined as the angle that this line creates with the x axis, and r is defined by the distance along this line from the origin to the LOR. 30
1.9 A 2D sinogram represents the polar coordinates, r and θ, of every line of response. LORs for angle θ are shown in red, which correspond to the red line on the sinogram. This also forms one row in the projection view, which represents all axial planes at one LOR angle. 31
1.10 In 3D PET mode, LORs can cross crystal rings in the z-plane, and ϕ describes the angle between the LOR and the z axis. As ϕ increases, fewer crystal rings are included in each projection so the z-dimension decreases. 32
1.11 Static PET mode produces one frame per acquisition, with no temporal information. Dynamic mode separates a PET acquisition into a series of time-frames. Gated acquisitions are divided into a series of gates that represent one cycle of an external signal, in this case an ECG. Acquired data is moved into the appropriate gate by determining the current point in the cycle. 34
1.12 The x-ray tube and detectors are mounted on opposite sides of the CT gantry, which rotates around the patient to obtain tomographic data. 36
1.13 Illustration of cine CT mode. A time-series of each slice is produced by performing several rotations of the x-ray gantry at each position. In this example, 16 slice locations are acquired per rotation, and data is acquired for 5 seconds before the bed moves to the next position. 38
1.14 A dual modality PET/CT scanner constructed in a single gantry. The x-ray tube and CT detector rotate about the patient, and the PET detector rings are static. PET and CT images are acquired in series. 40

1.15 CT x-ray tubes produce a lower energy spectrum, typically 30-140keV for tubes operated at 140 kVp, compared with 511 keV photons resulting from positron annihilation. 41
1.16 Multi-linear transforms used to convert CT images from HU to attenuation coefficients at 511 keV on a GE Discovery VCT. Transforms for 80 - 140 kVp shown over the range 0 HU to 1500 HU. . 41
1.17 Helical CT image (a) and the corresponding CT attenuation correction map (b). The CTAC has been spatially filtered and transformed to μ_{511} values. 42
1.18 Illustration of PET/CT half body acquisition protocol. The CT is acquired in < 30 s, where as the overlapping PET bed positions typically take < 20 min min for the entire study. 43
1.19 During inspiration, the diaphragm contracts and moves downwards, and the intercostal muscles move the chest wall upwards and outwards, increasing the thoracic volume. During expiration, these muscles relax and the thoracic volume is restored. 45
1.20 Illustration of gating methods. Gate numbers are determined by dividing the respiratory signal into time or variable time divisions, phase or amplitude divisions, or into variable amplitude divisions which maintains an equal amount of signal in each division. . . . 52
1.21 Example of artefact in gated cine CT that results from inter cycle variations in respiratory amplitude. A spatial discontinuity is seen on the superior edge of the liver. 54
1.22 A white band attenuation correction artefact, caused by PET-CT spatial mismatch, is seen at the diaphragm above the liver and spleen in the attenuation corrected PET image. 56
1.23 Example of respiratory motion artefact in FDG clinical imaging. PET-CT mismatch due to respiration led to the upper section of the liver being attenuation corrected with lung values. As a result the lung tumour, seen in the non attenuation corrected image and CT, appears as a lung mass of normal uptake in the attenuation corrected image. 58

1.24 Summary of the three approaches to reducing respiratory motion artefact, including the standard method where a helical CT acquired at an unknown point in the respiratory cycle is used for attenuation correction. 61
1.25 The PET gate which matches the respiratory position of the helical CT is registered to the remaining PET gates. A psuedo gated CT is produced by applying the resulting transformations to the helical CT. 67
1.26 (a) Non-gated 3D FDG PET acquired at 5 minutes per bed position, demonstrates less noise than gate 4 from the amplitude gated sequence (b). (c) The standard deviation of the liver ROI shown for each gate (blue squares), and the standard deviation measured on the non-gated image using the identical ROI (red line). 69

2.1 The sum of values in an ROI placed over the edge of the moving object represents the amplitude of displacement. 74
2.2 Typical magnitude spectrum for PET, detailing the initial spectral window f_1, f_2 and the peak Λ within the window, the reference window f_3 and mean reference value λ, and the threshold κ. Overall values f_{resp} and the associated restricted window $f_{resp} - \delta < f < f_{resp} + \delta$ are also shown. 78
2.3 Sagittal CT showing 6 bed steps and the respiratory curve segment, $\hat{\rho}$, produced from each step. Curve segments and the true curve are shown as a sinusoid for clarity. As $\hat{\rho}$ is related indirectly to displacement, an increase in $\hat{\rho}_0$, $\hat{\rho}_2$ $\hat{\rho}_3$ and $\hat{\rho}_5$ infers motion in the $+z$ direction, however an increase in $\hat{\rho}_1$ and $\hat{\rho}_4$ infer motion in the $-z$ direction, indicating that these two segments are flipped. . . . 83
2.4 The first projection angle of the PET phase weighted mask generated from the phantom experiment. The edge of the phantom normal to the direction of motion was accurately located, and the leading and trailing edges of the spheres are correctly weighted as positive (blue) and negative (red) respectively. 87

2.5 Data-driven (blue) and RPM based (red) respiratory curves for PET component of phantom acquisition. 87
2.6 Bins 0 and 6 of the gated CT for the phantom image. Red line shown for spatial reference. 89
2.7 Attenuation corrected PET MIPs for bins 0 and 6 of the gated phantom acquisition. Gated images contain less motion blur, but more noise than the non-gated image. Red lines shown for spatial reference. 90
2.8 Patient 1. Coronal (top) and sagittal (bottom) fused PET and CT images, bins 3, 5, 8 (left to right). 90
2.9 Patient 3. Coronal (top) and sagittal (bottom) fused PET and CT images, bins 2, 5, 8 (left to right). 91
2.10 PET normalised RPM curve (red) overlaid with normalised data-driven curve (black). 92
2.11 CT normalised RPM curve (red) overlaid with normalised data-driven curve (black). 93
2.12 Centre of mass of the counts within a volume of interest defined over the tumour on non-attenuation corrected PET images. The COM along the z axis is shown, for images gated with the RPM signal (diamond) and the data-driven signal (square). 95
2.13 Centre of mass of a volume of interest defined over the tumour CT images gated with the RPM trace (diamond) and the data-driven signal (square). The COM along the z axis is shown. 96
2.14 PET zCOM range (left) and nRMSE values (right) calculated from images created with parameter variations 97
2.15 CT zCOM range (left) and nRMSE values (right) calculated from images created with parameter variations 97
2.16 Coronal CT images for patients 1 bin 5 and patient 3 bin 6, RPM derived image demonstrating respiratory motion artefact, particularly at the diaphragm; data-driven image demonstrates reduced artefact. 98

3.1 Flow chart describing the method to correct the direction of the gates in a given bed position. A simple, 1D registration is used to determine the z-direction of movement in the MIP images, which are produced from 2D (SSRB), normalised reconstructed images. If the direction is determined as negative, the gated series are reversed. 107

3.2 Amplitude normalised RPM (red) and data-driven (blue) respiratory curves for 6 bed positions, patient 11. Positions 1 and 6, acquired over the pelvis and head respectively. Clipped peaks exist where the amplitude exceeds the 95% outlier limit. RPM and DDG signals for bed positions 2, 3 and 4 appear to match closely, and bed positions 1 and 6 - where no motion was visible in either NAC image dataset, matched poorly. NRMS error values were calculated as 1: 27%, 2: 7%, 3: 17%, 4: 11%, 5: 29%, 6: 34%. . . 111

3.3 Mean NRMS error between data-driven and RPM curves for each bed position. The error bars indicate 1 standard deviation. Five bed positions which contained failed RPM data were removed. Less error is seen for central bed positions. All patients scanned from feet to head. 112

3.4 Data-driven gated (top row) and RPM gated (bottom row) attenuation corrected MIP images for patient 1. The non-gated image is shown on the far left, followed by gates 1, 4 and 8 from left to right. Horizontal lines which cross displaced structures are shown for reference. Bed positions are indicated by numbers on the left. 113

3.5 Bland-Altman plot comparing the total COM displacement in VOIs defined on the data-driven and RPM gated datasets. On average, the data-driven gated images produced greater COM displacement, however no significant difference was found between the two methods ($p = 0.13$). 114

4.1 An example of a phase weighted mask overlaid on a projection image for an NH_3 cardiac PET image acquired from 6 to 26 min post injection. Uptake in the liver and myocardium both contribute to the respiratory signal. 122

4.2 Data-driven curve for patient 1 (top). Decay corrected curve (middle) contains gradual decrease in baseline. A 4th order polynomial fitted to the decay corrected curve (shown in red). The decay corrected curve was *straightened* by normalising to the polynomial (bottom). 124
4.3 An example of a cine CT slice overlaid with the mask that identifies respiratory motion (green) and cardiac motion (red). 125
4.4 (a) The CT gating method used in chapter 2, gates are populated with images acquired when the signal matches the amplitude range for each gate. (b) The method used in this chapter, the longest continuous and monotonic section of the respiratory cycle is used to populate the gates. Missing data is filled with the nearest neighbour. 126
4.5 Flowchart describing the simulation of a cine CT by registering the PET gate which matches the helical CTAC to all remaining PET gates. The resulting transformation vectors are then applied to the helical CTAC. 128
4.6 Cardiac wall intensity was determined as the height of profiles defined on short axis images. 131
4.7 (a) Replacing CT1, which aligns correctly with the PET image, with CT2, which aligns poorly with the PET image, results in worse PET-CT alignment. Incorrectly using lung attenuation correction values for a region of the myocardium in PET (labeled *LV PET*) reduces the anterior wall activity in PET images. (b) Improved PET-CT alignment results when CT1 is replaced with CT2, resulting in an increase in anterior wall activity in attenuation corrected PET. (c) A positive correlation between the change in alignment and the change in anterior wall intensity is expected. 132
4.8 PET-CT alignment of the liver. A profile was defined along the z-axis over the liver edge in both datasets, and a straight line was fit to the section ranging from 0.8 to 0.2 of the intensity normalised profile. Alignment was defined as the z-axis separation between the two straight lines at y = 0.5. 134

4.9 Bland Altman plot of the range of myocardial wall motion (first to last gate) of NAC PET images gated with the data-driven gating method, and the RPM gating method. No significant difference was found between the two methods when comparing the motion range (p = 0.052). 135
4.10 Patient 38, rest scan. RPM (red) overlaid with the data-driven curve (blue). The RPM curve demonstrates a gradual baseline increase throughout the duration of the scan. Larger displacement across the gates was measured on the data-driven gated images (9.8 mm) than the RPM gated method (6.7 mm). 136
4.11 Cardiac wall position for gated cine CT (red dashed) and pseudo gated CT (green dotted) for an example scan with approximately 2.8 mm of cardiac contractile motion in the gated cine sequence. Displacement from contractile motion was estimated by fitting a straight line (shown in blue) between points either side of the undulation, and finding the maximum offset to the image derived displacement curve. 137
4.12 PET-CT alignment error averaged over all scans and all gates, at the anterior wall of the myocardium (top) and liver (bottom) for the helical CT, gated, average and pseudo gated CT CTs displayed as histograms. The helical CT produces the most errors, and the pseudo gated CT produces the least. 139
4.13 When the helical CT is replaced with the ACT, GCT or pseudo gated CT, the resulting change in PET-CT alignment of the myocardial wall correlates well with the resulting change in anterior wall intensity measured on the attenuation corrected PET. Generally, an improvement in alignment (a positive change) creates an increase in anterior wall intensity, and a worse alignment (a negative change) produces a decrease in anterior wall intensity. . . 141
4.14 The percentage change in cardiac anterior and lateral wall intensities in PET images when the helical CTAC was replaced with the average, gated and pseudo gated CTACs. More of a positive bias is seen with the AC_{pseudo} images. 143

4.15 An example where PET-CT alignment improved from 7.9 mm with the helical CT to 3.0 mm and 0.6 mm for the gated and pseudo gated CTs respectively. Anterior apical defect on the AC_{HCT} PET images is not present in AC_{GCT} and AC_{pseudo}, and the anterior wall increased by 43% and 46% respectively. 144
4.16 Cardiac PET-CT alignment is decreased from 0.3 mm with the helical CT to 11.5 mm with the gated cine CT. A 37% decrease in the anterior wall of the AC_{gated} AC PET images appears as a defect. Cardiac PET-CT alignment for the pseudo gated is 1.6 mm, and no anterior wall defect is seen. 145
4.17 For the anterior and inferior walls, a significant ($p < 0.05$) correlation was found between the effect of motion correction (the change in profile maximum measured on $ACReg_{GCT}$ and $ACReg_{pseudo}$) and the range of respiratory induced motion measured on NAC gated PET images. No correlation was found for the septal and lateral walls. 147
4.18 Short axis slices for the non-registered AC_{GCT} (left) and registered $ACReg_{GCT}$ (right) PET images. Registration increased the anterior and inferior wall maximum by 26% and 19% respectively. . . 148
4.19 Histograms of relative displacement based on respiratory curves from 3 example patients, all with a cardiac respiratory displacement range of 11 mm (determined on NAC PET images). Type 2 curve on the left demonstrated 27% improvement from motion correction, and the type 1 curve in the centre demonstrated a 3% improvement. On the right however, another type 2 curve produced only 5% improvement. 152

Chapter 1

Introduction

In combined positron emission tomography (PET) / computed tomography (CT) imaging, respiratory motion can introduce severe artefacts that alter the clinical interpretation of images. A range of approaches to reduce these artefacts have been developed, and these vary in efficacy and complexity. In this work, a new method of acquiring artefact-reduced images is developed and validated using clinical PET/CT images. This method is automatic, and derives an estimate of the respiratory cycle from the acquired dynamic data itself rather than from hardware required by conventional methods. Several approaches of artefact reduction, some incorporating this new method, are compared using clinical cardiac images.

In this chapter, a brief overview of PET scanner principles is presented, followed by CT and dual modality PET/CT. Respiratory motion, and its effect on PET/CT imaging is then described. Following this, the various existing approaches to reduce respiratory motion induced artefacts are reviewed.

1.1 Background

As a functional imaging modality, positron emission tomography (PET) was initially used exclusively for research imaging. Now, PET has a widespread presence in both research and clinical imaging. The primary reason for PET becoming a diagnostic imaging modality was the development of $[^{18}F]$-flourodeoxyglucose

Isotope	Half-life (min)	Common tracer and use
^{15}O	2.03	Water, perfusion studies (neurology)
^{11}C	20.3	Methionine, protein synthesis (oncology)
^{13}N	9.97	Ammonia, myocardial perfusion
^{18}F	109.8	FDG, glucose metabolism (oncology, cardiology, neurology)

Table 1.1: Common positron emitting isotopes used in PET imaging and common associated tracers and their applications.

(FDG), a tracer that provides a means of imaging the glucose metabolism.

Compared with alternative functional imaging modalities such as single photon emission computed tomography (SPECT), PET offers several advantages including greater sensitivity and quantitative accuracy. Additionally, most positron emitting isotopes are short lived which allows acquisition of high count rate images while maintaining a relatively low radiation dose to the patient. These benefits extend to both research and clinical domains.

1.1.1 PET tracers

Commonly used PET isotopes are listed in table 1.1, with typically associated tracers and applications. The two PET tracers used in this work are FDG and $[^{13}N]$Ammonia (NH_3).

The glucose analogue, FDG, is the most commonly used PET tracer for clinical imaging. FDG follows a similar metabolic pathway to glucose, however after phosphorylation the molecule remains trapped within the cell. After allowing enough time, typically 60 - 90 min, for the injected FDG to move into cells and reach this trapped state, an image of the FDG distribution provides information on glucose metabolism. While this has applications in neurology and cardiology, its most frequent use is in oncology as many cancer cell types are known to hypermetabolise glucose. In this context, FDG is mostly used in disease staging and for monitoring response to treatment.

In cardiology, FDG provides an indication of myocardial viability which is often combined with perfusion imaging to assess myocardial disease. While

$[^{15}O]$water can be regarded as the ideal tracer for perfusion imaging, its short half life makes this impractical for clinical use. An alternative to $[^{15}O]$water is $[^{13}N]$Ammonia which is extracted from blood into the myocardium and becomes trapped in the glutamic acid-glutamate metabolic pathway, providing a mechanism to image myocardial perfusion.

1.1.2 PET

An unstable isotope that undergoes positron decay releases a positron and a neutrino. When the positron interacts with an electron and the pair annihilate, their rest masses are converted into two 511 keV photons which are released simultaneously and in opposite directions, as illustrated in figure 1.1. The average distance of the annihilation event from the decay process, i.e. the positron path length, depends on the positron energy and is on average less than 0.5 mm for F-18 and C-11 in water [25, 37].

A PET scanner detects both of the 511 keV photons and determines the line, or *line of response* (LOR), which intersects the scanner crystals that detected each photon. Providing both photons arrived at the detectors without interacting with the traversed material, the LOR also approximately intersects the positron annihilation event.

A typical PET scanner, illustrated in figure 1.2, is constructed from a contiguous series of detector rings, commonly spanning a total of 15-25 cm in the axial direction. Each detector unit, referred to as a block detector, usually consists of a section of scintillating crystal, usually lutetium orthosilicate (LSO) or bismuth germanate (BGO), separated into individual elements. This crystal array is optically coupled to a collection of photomultiplier tubes (PMTs). Due to size constraints, one-to-one coupling of crystal elements and PMTs is not possible, and several crystal elements are generally coupled to one PMT. A photon that interacts with a crystal element causes the crystal to scintillate and release a pulse of visible or near visible light. An electrical pulse is then generated from this scintillating light by the PMTs, and the crystal element in which the interaction occurred is determined by calculating the weighted average of the signal produced by each PMT in the block detector. These crystal coordinates of one

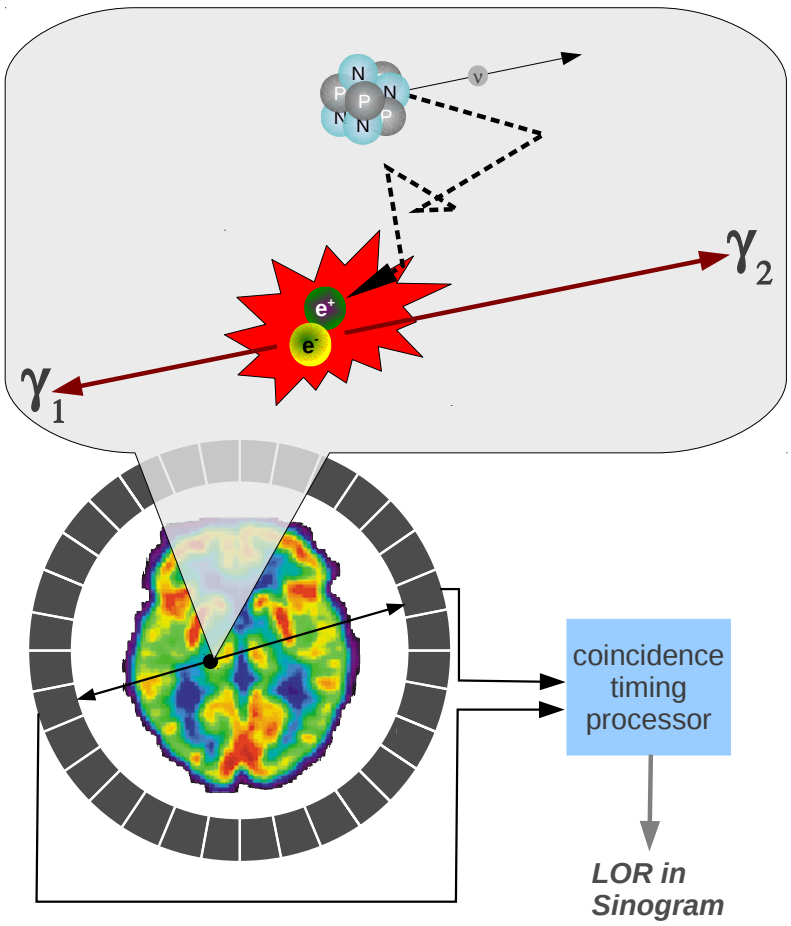

Figure 1.1: A positron (e^+) and a neutrino (ν) are ejected from an atom that undergoes positron decay. Two 511 keV photons are produced when the positron annihilates with an electron (e^-). If both photons are detected within a set timing window, as determined by the coincidence timing processor, then a line of response is registered.

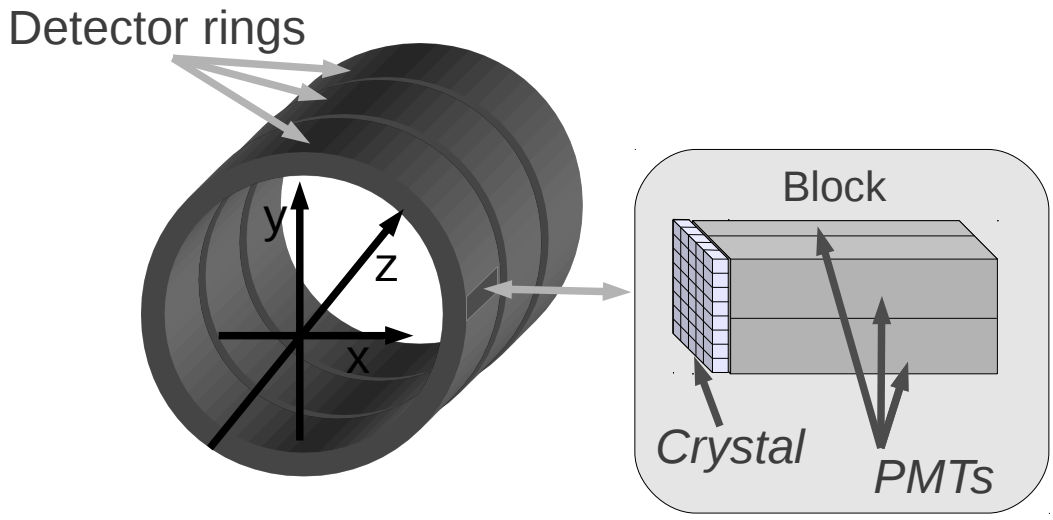

Figure 1.2: PET scanners are constructed from adjacent rings of detectors. Each detector block consists of an array of scintillating crystal coupled to photomultiplier tubes.

detected photon are parameters of a *"single"* event.

To identify two single events which originate from one decay process (and determine the LOR), a coincidence timing window is defined. Pairs of single events that are detected within this temporal window (typically 0.5 to 10 ns) are defined as *coincident* events, and the corresponding LOR is recorded.

An LOR describes the location of two detected photons originating from one decay process known as a true coincidence event (figure 1.3a). However, not all photons reach the detectors without interaction, photons can either be scattered or fail to reach the detector entirely (attenuation). Additionally, two photons from different decay processes can be incorrectly identified as originating from the same original decay. This LOR is known as a *"random"* coincident event.

1.1.2.1 Attenuation

The probability, P_{single}, of a single 511 keV photon travelling through a substance without interaction depends on the distance traveled through the material, x, and

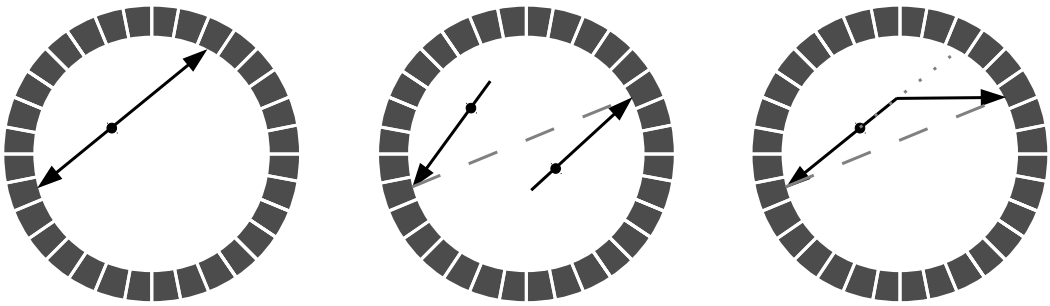

Figure 1.3: (a) A true coincidence produces an LOR that passes through the decay event. (b) Random events are produced from two independent decay events detected within the coincidence timing window. (c) Photon scatter can move the LOR such that it no longer passes through the decay event.

the attenuation coefficient of the material at 511 keV, μ,

$$P_{single} = e^{-\mu x} \tag{1.1}$$

In PET, the identification of a decay event relies on two 511 keV photons reaching the detectors. In figure 1.4, a decay event occurs at depth x in an object with thickness L and of uniform attenuation coefficient. The probability of both photons being detected is the product of the individual probabilities,

$$P_{pair} = e^{-\mu x} e^{-\mu(L-x)} = e^{-\mu L} \tag{1.2}$$

which is independent of the position, x, along the line of response. The probability of attenuation is therefore only dependent on the thickness, L, and attenuation coefficient μ of the material. When these two factors are known, an attenuation correction factor can be defined for each LOR to correct for the loss of detected events resulting from attenuation.

On older dedicated PET systems, this was typically done by acquiring a transmission map of the patient by using an emission source such as positron emitting ^{68}Ge or 662 keV gamma emitting ^{137}Cs. Given the low radioactivity used in

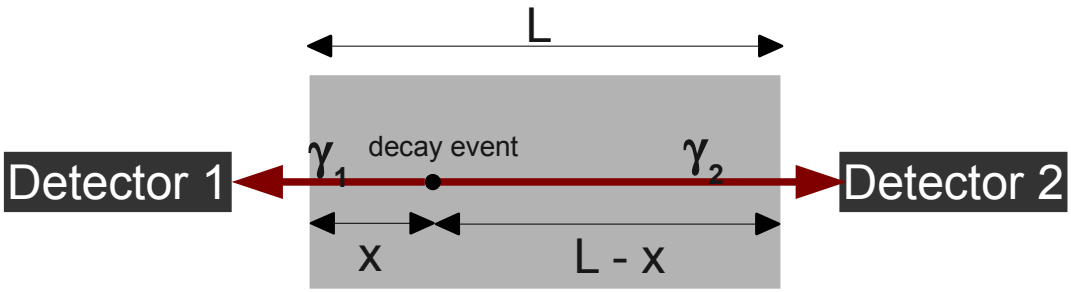

Figure 1.4: Both photons must reach a detector to identify a decay event. Here, the decay event occurred at point x in object with thickness L. The probability of attenuation depends only on L and the attenuation coefficient of the material.

these sources, transmission images generally required approximately 3 minutes to acquire enough statistics to form an attenuation correction map, thus adding considerable time to clinical imaging protocols.

Combined PET/CT scanners sequentially acquire CT and PET data with the patient remaining on the same scanner couch. In the absence of voluntary and involuntary motion, these two data sets are spatially aligned, and an attenuation correction map derived from the CT can supersede the transmission scan. This is described in section 1.1.4.1.

1.1.2.2 Randoms and scatter

While attenuation reduces the number of events detected by the scanner, randoms and scatter produce noise in the acquired data. A *random* event (figure 1.3b) occurs when two independent photons are detected by the PET scanner within the coincidence timing window, and the scanner incorrectly identifies an LOR.

Also, a photon can deviate from its trajectory if it undergoes a Compton scattering event. As illustrated in figure 1.3 c, this can displace the defined LOR such that it does not pass through the point of the decay process. The likelihood of scattered coincidence events primarily depends on the total path length and

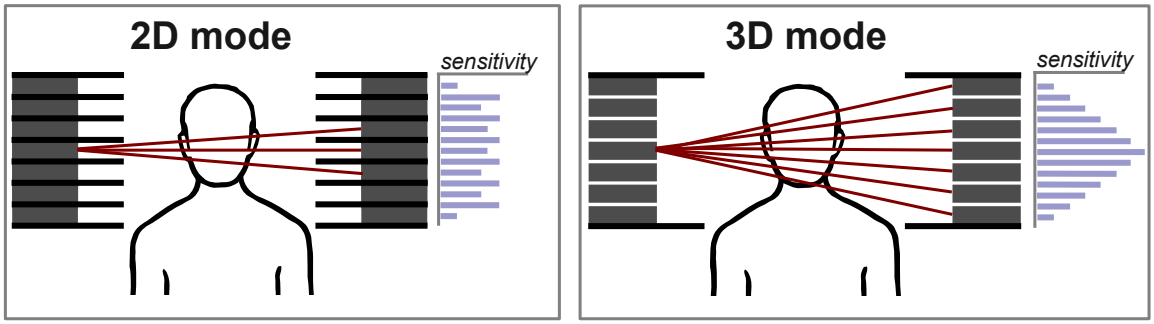

Figure 1.5: Simplified illustration of 2D and 3D PET modes. In 2D mode, each detector only accepts LORs that correspond to the same or adjacent detector rings. In 3D mode, all LORs are accepted.

attenuation characteristics of the material which the LORs traverse.

1.1.2.3 2D and 3D PET

Although not available on all modern commercial PET scanners, some older systems are capable of acquiring PET data in 2D and 3D modes. As illustrated in figure 1.5, in 2D mode, retractable lead or tungsten septa is used to only allow coincident events from within the same or adjacent crystal rings. When imaging in 3D mode, the septa are removed and coincident events between any crystal ring pairs are allowed. An increase in overall sensitivity is therefore achieved when 3D mode is used [20].

Most PET scanners re-bin the LORs which cross one adjacent crystal ring into an image slice forming an indirect plane in between the two adjacent direct-planes. As a result, a slight variation in sensitivity exists across the axial field of view in 2D mode, as shown in figure 1.5. In 3D, the sensitivity across the scanner field of view becomes more non-uniform because crystal rings in the centre of the scanner are coupled with more crystal rings than rings located towards the end of the scanner. The variation in sensitivity in the axial direction for 2D and 3D mode is illustrated in figure 1.5.

While 3D mode increases the sensitivity to true events, the sensitivity to randoms and scatter also increases. In 2D mode, the septa block singles from

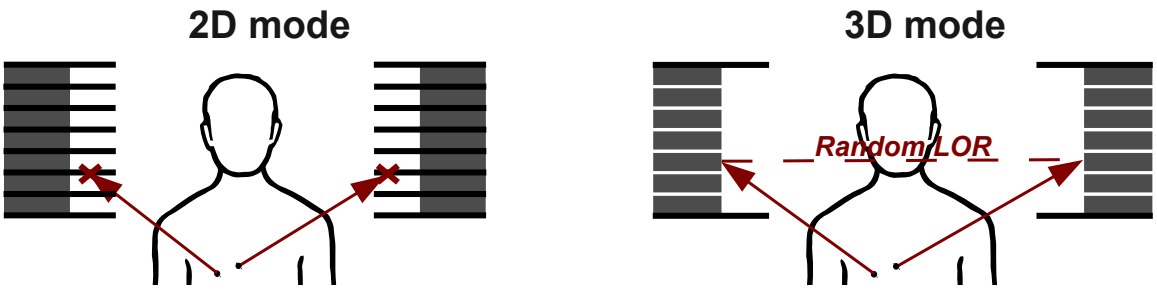

Figure 1.6: In 2D mode, random events from external activity are blocked by the septa. Removing the septa increases the likelihood of randoms events.

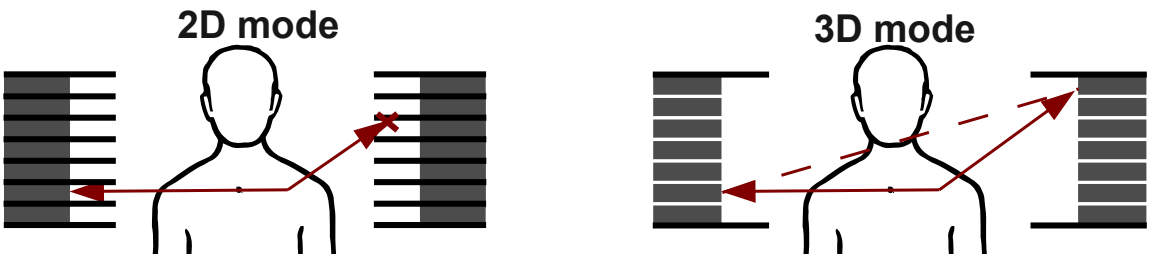

Figure 1.7: In 3D mode, more scattered events can be detected by the scanner.

high activity regions outside the scanner, thereby reducing the randoms rate. When the septa are removed however, more single events outside the scanner can reach the detectors and the randoms rate is increased. This is illustrated in figure 1.6.

Similarly, only scattered photons that remain within the same ring of detectors will register as an LOR when scanning in 2D mode. When the septa are removed however, a larger proportion of scattered photons are able to be detected by the scanner, as illustrated in figure 1.7.

This increase in scatter and randoms rates depends on scanner and patient geometry, and the distribution of activity inside and outside the field of view.

Imaging in 3D mode with BGO scanners has been shown to produce higher quality images for the brain where a lower volume of tissue inside the field of view exists [21, 126]. For the thorax and abdomen, however, the larger volume of tissue and the presence of activity outside the image field of view results poorer quality images for 3D than 2D in some cases [5, 75].

In comparison to BGO scanners, the faster scintillation decay time and higher energy resolution of PET scanners with LSO crystals reduce detected random and scatter coincidences. In this case whole body PET imaging in 3D can produce superior quality images to 2D [82, 142]. Additionally, recent improvements to PET reconstruction have included randoms and scatter corrections into an iterative reconstruction algorithm, substantially improving the effectiveness of these corrections [56]. In BGO PET scanners, 3D whole body images reconstructed using this improved algorithm are generally better quality than 2D images, even for large patients [70].

1.1.2.4 Sinogram and listmode formats

Raw PET data is commonly stored in sinogram format, where each detectable LOR is represented in polar coordinates (r, θ) (for 2D PET). The polar coordinate system for 2D PET is illustrated in figure 1.8, where a line is defined that is normal to the LOR and passes through the scanner centre (axis origin). The angle that this line creates with the x axis defines θ, and the distance along this line from the origin to the LOR defines r.

As a histogram, a sinogram describes the total number of events detected during an acquisition. Sinograms for 2D PET acquisitions are defined as a 3-dimensional stack of sinograms, with one sinogram per axial plane. As shown in figure 1.9, each row of the sinogram represents a projection angle of the data. A 2D projection of the activity distribution can therefore be obtained by considering one projection angle over all axial planes. The coordinate system used to describe 2D sinograms in this work defines the LOR angle and radial position as θ and r respectively, and the slice number or image plane as z.

For 3D PET acquisitions, sinograms include a 4th dimension to record the angle, ϕ, that describes the number of detector rings crossed by the LOR in the

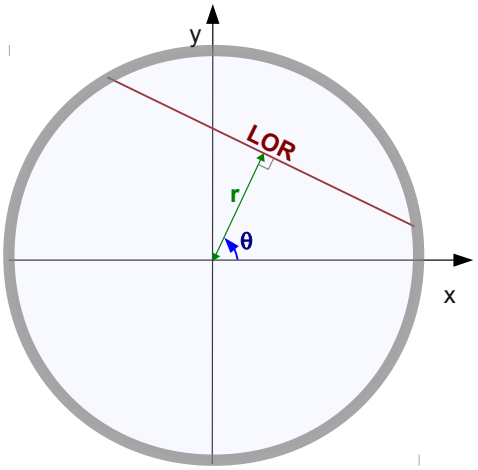

Figure 1.8: The polar coordinate system, (r, θ), used to define LORs in 2D PET mode. A line from the origin and normal to the LOR is created. θ is defined as the angle that this line creates with the x axis, and r is defined by the distance along this line from the origin to the LOR.

axial direction, as illustrated in figure 1.10.

In dynamic PET imaging, a sinogram must be created for each acquired frame resulting in a large amount of data when short time frames are acquired over a long time period. As an alternative to creating histograms of each time frame, every detected coincident event can be recorded with the time of detection in a listmode file. As 4D data, listmode files provide flexibility to retrospectively re-bin, or *unlist* the recorded coincident events into sinograms of any temporal duration (within the temporal resolution of the listmode format, typically 1 ms).

1.1.2.5 PET Imaging modes

Most modern commercial PET systems are capable of acquiring PET data in 3 modes, static, dynamic and gated. These modes are illustrated in figure 1.11. At present, no commercial PET scanners can image with the bed moving continuously through the field of view. Images can only be acquired as single *bed positions*, with the scanner bed remaining in one position for the duration of the frame. Several bed positions can be joined together to extend the imaged area.

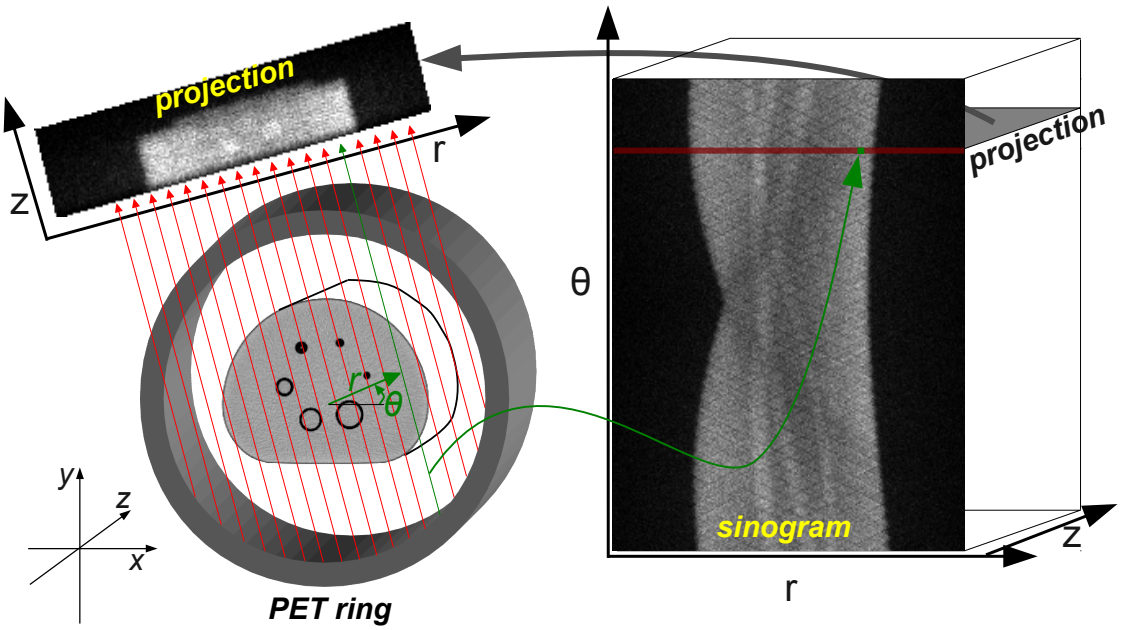

Figure 1.9: A 2D sinogram represents the polar coordinates, r and θ, of every line of response. LORs for angle θ are shown in red, which correspond to the red line on the sinogram. This also forms one row in the projection view, which represents all axial planes at one LOR angle.

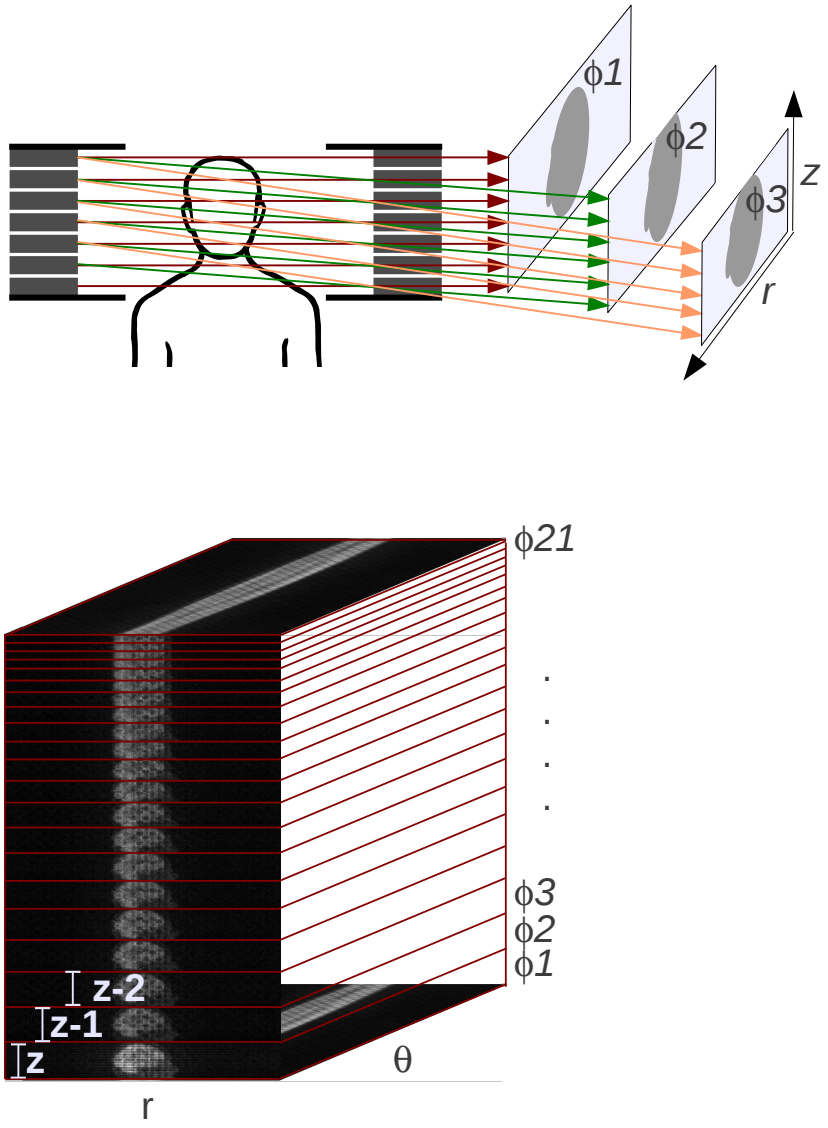

Figure 1.10: In 3D PET mode, LORs can cross crystal rings in the z-plane, and ϕ describes the angle between the LOR and the z axis. As ϕ increases, fewer crystal rings are included in each projection so the z-dimension decreases.

- **Static** Generally, most clinical PET acquisitions are performed in static mode. At each bed position, only one image volume is produced, representing spatial dimensions only (although temporal information can be stored if listmode format is used. See section 1.1.2.4.)

- **Dynamic** PET images can be acquired dynamically by dividing data into separate, continuous time frames. In the example shown in figure 1.11 a 5 min acquisition is separated into 9 frames, providing 6×10 s frames, 2×1 min frames, and 1×2 min frame.

- **Gated** PET images can also be divided into separate sections, or gates, according to an external periodic signal which usually either represents the respiratory or cardiac cycle. On initialising an acquisition, a series of empty sinograms (typically 6-8 for cardiac imaging), referred to as gates, are created which represent one cycle of the motion. Throughout the acquisition, the signal is referenced to determine the current point in the cycle, and the acquired data is added to the corresponding sinogram gate. Different parameters of the signal can be used to determine the current point in the cycle and these are discussed in section 1.3.2 in the context of respiratory gating. For cardiac gating, as illustrated in the example in figure 1.11, the electro-cardiogram (ECG) period is usually divided into equally spaced temporal sections to determine the point in the cardiac cycle. The detection of an R-wave generates a trigger signal to cause the PET scanner to restart the sequence for the next cardiac cycle.

1.1.2.6 Image reconstruction

PET scanners record events as lines of response, and this data can be described as projections of the imaged activity distribution (see section 1.1.2.4). An approximate image of the activity distribution can be reconstructed from this projection data, and two main reconstruction methods are commonly used in clinical PET imaging. The first method is filtered back projection (FBP), where projection data is filtered and then back projected to obtain a reconstructed image. The process can be performed in real space or in frequency space. FBP is a linear

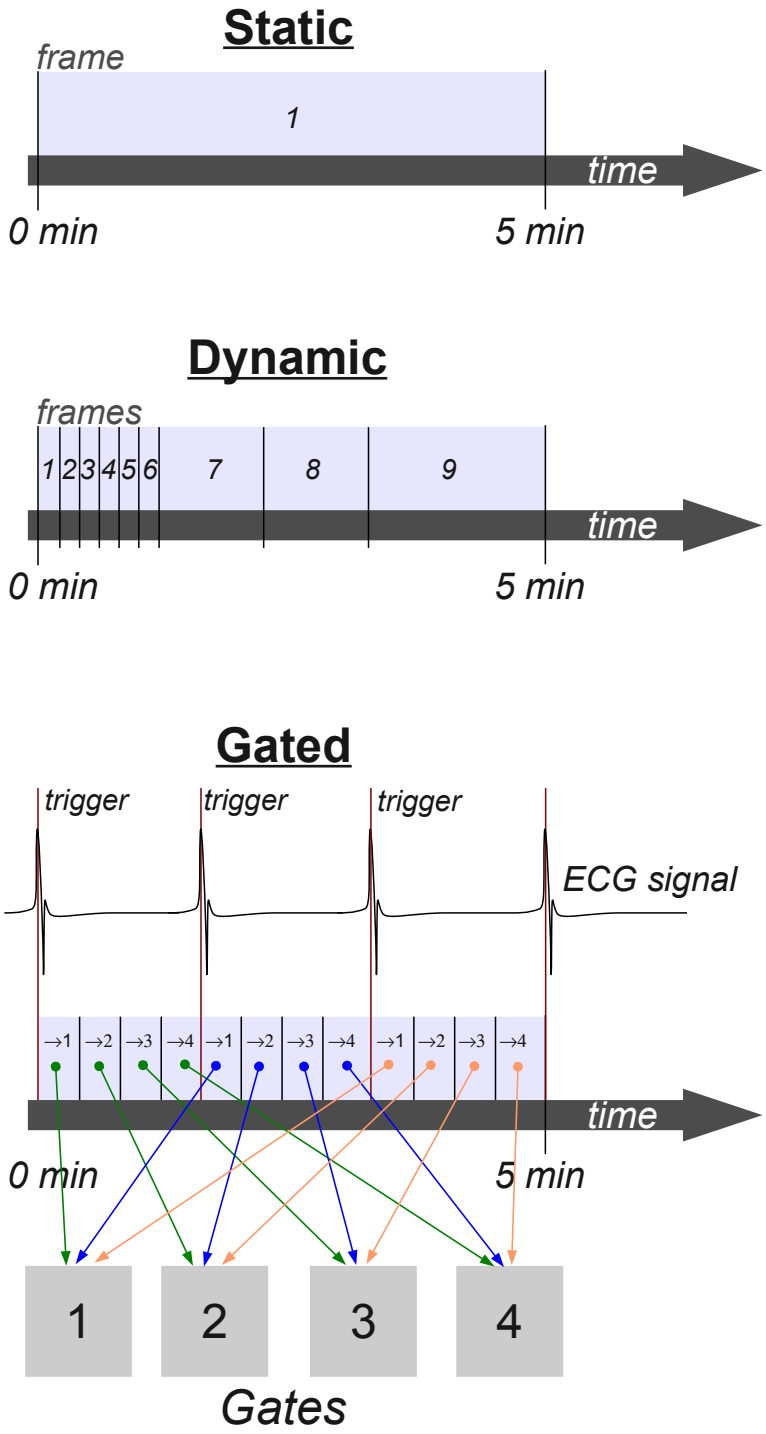

Figure 1.11: Static PET mode produces one frame per acquisition, with no temporal information. Dynamic mode separates a PET acquisition into a series of time-frames. Gated acquisitions are divided into a series of gates that represent one cycle of an external signal, in this case an ECG. Acquired data is moved into the appropriate gate by determining the current point in the cycle.

transformation, however *star* and *streak* artefacts are common characteristics in the presence of noise.

The second method is iterative reconstruction. These methods iteratively update an estimate of the activity distribution, forward project the estimate into sinogram space and then compare the projection with the original noisy sinogram data. A common implementation of iterative reconstruction on commercial PET scanners is ordered subsets expectation maximisation (OSEM) [54]. Images reconstructed with iterative methods generally contain less noise than images reconstructed with FBP, however OSEM is a non-linear process, i.e. adding and then reconstructing sinograms can produce a different result to reconstructing and then adding the images.

1.1.3 Computed Tomography

Computed tomography (CT) scanners measure the amount of x-ray radiation transmitted through an object being scanned. X-rays are produced by bombarding an anode, typically tungsten, with a beam of electrons produced by a heated cathode. The electrons are accelerated in a vacuum, across a voltage potential, and when the electrons collide with the cathode bremsstrahlung x-ray radiation is produced. The x-rays are filtered to remove low energy photons and collimated to produce a beam that is directed through the object being scanned. A projection image which describes the attenuation properties of the object is formed by measuring the proportion of x-ray photons which are transmitted through the object.

To obtain a tomographic acquisition, the x-ray tube and detectors are mounted on a rotating gantry, as illustrated in figure 1.12. Multiple projections are then acquired as the gantry rotates, and a 3D image volume is reconstructed from the projections, usually by using filtered backprojection (see section 1.1.2.6).

CT images are described in Hounsfield Units (HU),

$$HU_x = \frac{\mu_x - \mu_{water}}{\mu_{water}} \times 1000 \tag{1.3}$$

where HU_x is the HU value for a material with linear attenuation coefficient μ_x.

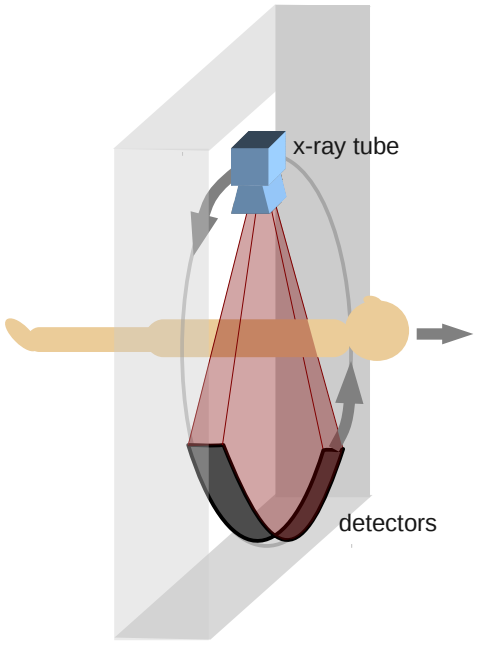

Figure 1.12: The x-ray tube and detectors are mounted on opposite sides of the CT gantry, which rotates around the patient to obtain tomographic data.

1.1.3.1 CT Imaging modes

Modern CT scanners are *multi-slice*, such that several axial acquisitions can be acquired during each gantry rotation. CT scanners are usually capable of imaging in axial, helical, and cine modes.

- **Axial** In axial mode scanning, the gantry is rotated once to obtain a series of image slices (in the case of multi-slice scanners). The scanner bed then moves to the next position and the gantry rotates once, producing another series of images. This is repeated until the required axial coverage has been acquired.

- **Helical** Rather than stepping the bed to each required position after a single tube rotation and acquiring a series of images, in helical mode imaging the gantry rotates continuously with the x-ray tube energised, while the scanner couch moves the patient through the scanner at a constant speed. The acquisition time of helical scans is generally much shorter than axial

mode imaging.

- **Cine** Where axial and helical mode scans generally produce a single 2D image at each slice location, a cine CT scan produces a time-series of 2D slices at each location. Cine mode is similar to axial mode, except rather than rotating the tube once at each position, several rotations are performed. This is illustrated in figure 1.13

- **Gated** CT acquisitions can be gated according to an external periodic signal that usually represents the cardiac or respiratory cycle. Gating can be performed prospectively or retrospectively. In prospective gating, the x-ray tube is activated only during a particular section of the motion signal, for example the end diastole state of the cardiac cycle. In retrospective gating, a cine CT is acquired and synchronised with the external cardiac or respiratory signal. Images are reconstructed, and then by referencing the signal they are sorted according to the point in the cycle that each image was acquired, creating one full sequence of the cycle for each cine position. Gating 4D helical CT scans is also possible [60], but this is not available on most commercial PET/CT scanners.

1.1.3.2 Imaging parameters and dosimetry

The amount of radiation dose that a patient absorbs from a CT scan depends largely on the parameters used during the acquisition. Imaging parameters adjust the noise and contrast of the images by varying the characteristics of the x-ray beam, the configuration of the detectors, and the acquisition rate. Generally, a reduction in image noise (while maintaining slice thickness) is achieved by increasing the x-ray flux, which consequently increases patient dose. The main acquisition parameters include,

- **Tube voltage (kVp)** Increasing the voltage of the x-ray tube produces more x-ray photons and increases the mean x-ray photon energy. A higher photon energy results in a greater penetration of the x-ray beam, thus increasing the exposure to central organs and increasing the overall absorbed

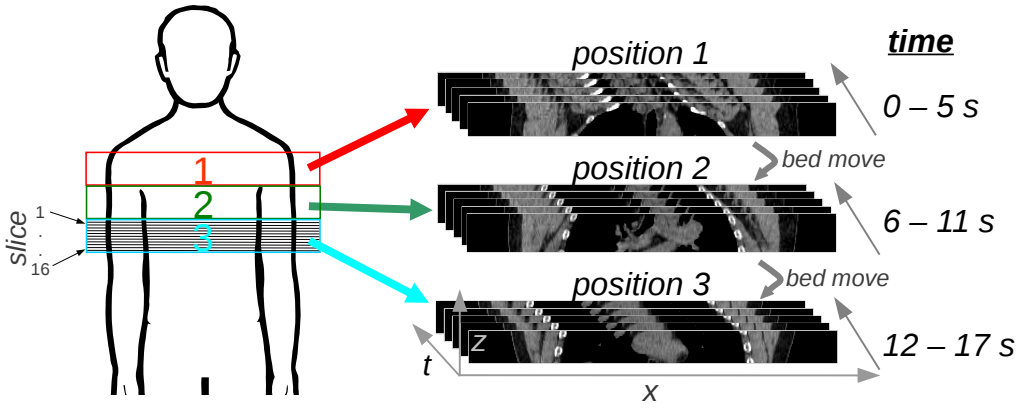

Figure 1.13: Illustration of cine CT mode. A time-series of each slice is produced by performing several rotations of the x-ray gantry at each position. In this example, 16 slice locations are acquired per rotation, and data is acquired for 5 seconds before the bed moves to the next position.

dose. A non-linear relationship exists between the tube voltage and patient dose.

- **Beam current (mA)** By increasing the current to the x-ray tube, more electrons are released from the cathode. Under normal operating conditions of CT scanners, the x-ray flux is linearly proportional to the x-ray tube current. Tube current is therefore also linearly proportional to patient dose.

- **Rotation time (sec)** This describes the time which the gantry takes to rotate 360°. Exposure is commonly described as the product of rotation time and beam current (mA.s), which is linearly proportional to patient absorbed dose. Acquisitions in cine mode generally impose a considerably higher dose than an axial or helical scans because several tube rotations are performed at each position.

- **Collimation** Multi-slice CT scanners usually allow the adjustment of the x-ray beam axial width and the configuration of detectors in the axial direction. A wide beam is generally more dose efficient than a narrow beam.

This is attributed to the penumbra, or shoulder sections of the beam profile which is not used in image production but that does impose a dose to the patient. When a narrow beam width is used, the penumbra forms a larger proportion of the total beam than when a larger beam width is used.

- **Pitch**. In helical mode, the x-ray beam forms a helical path as the bed moves through the gantry. Pitch describes the separation between each turn of the helix, and is defined as

$$pitch = \frac{d_{rot}}{w} \tag{1.4}$$

where d_{rot} is the distance that the bed travels for each rotation, and w is the beam width. Increasing the pitch therefore decreases the exposure over a given scan range.

1.1.4 Dual modality PET/CT

Modern PET scanners generally co-exist in series with CT units, forming dual modality PET/CT scanners, as illustrated in figure 1.14. With these scanners, PET and CT images can be acquired in sequence while the patient remains in one position [10]. The advantage here is twofold: the additional anatomical information which the CT image provides has been shown to improve the diagnostic quality compared to PET imaging alone [7, 19, 50, 74, 121], and the CT is also used to attenuation correct the PET data.

1.1.4.1 CT based PET attenuation correction

A CT image describes the linear attenuation coefficients of the scanned material, however direct use of these data to attenuation correct PET acquisitions is not possible. X-ray tubes produce a spectrum of photon energies typically in the range of 30 keV to 140 keV, compared with positron annihilation which produces 511 keV photons. This is illustrated in figure 1.15. At lower CT energies, both photoelectric and Compton interactions occur. For 511 keV PET photons however, all first interactions occur as Compton scatter. As the total attenuation coefficient of a material is the sum of contributions from all interactions

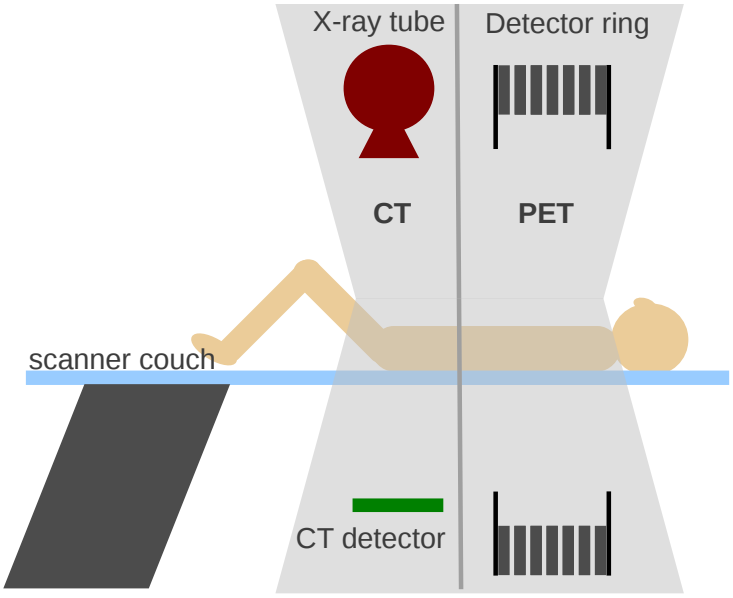

Figure 1.14: A dual modality PET/CT scanner constructed in a single gantry. The x-ray tube and CT detector rotate about the patient, and the PET detector rings are static. PET and CT images are acquired in series.

including Compton and photoelectric, a given material will posses different linear attenuation coefficients at CT and PET energies.

To attenuation correct PET data with CT images, the CT derived attenuation coefficients must first be transformed to 511 keV attenuation coefficients (μ_{511}) [66]. A multi-linear transform is commonly used to achieve this, which assumes that CT values ranging from -1000 to 0 represent a mixture of air and soft tissue, and values ranging from 0 to 1000 represent a mixture of soft tissue and bone [16]. Each of these groups are scaled from HU to μ_{511} using different gradients. As the x-ray energy spectrum varies with tube voltage, the transformation function must be defined at each available voltage. Figure 1.16 shows the multi-linear functions for tube voltage settings of 80, 100, 120 and 140 kVp for a GE Discovery VCT.

Following conversion to μ_{511} attenuation coefficients, a spatial filter is applied to match the lower spatial resolution of PET. Figure 1.17 shows a coronal slice from a CT image with the corresponding CT attenuation correction (CTAC) image following multi-linear transformation and spatial filtering. Attenuation correction maps are then integrated along the path of each line of response to

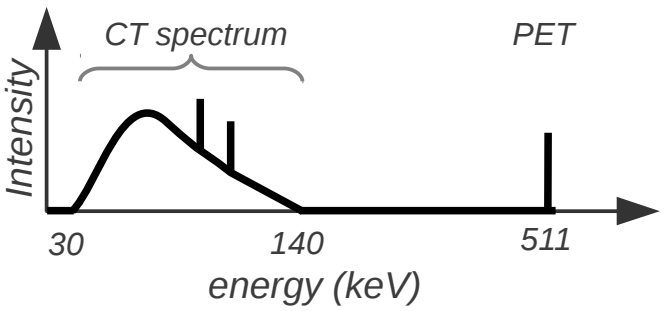

Figure 1.15: CT x-ray tubes produce a lower energy spectrum, typically 30-140keV for tubes operated at 140 kVp, compared with 511 keV photons resulting from positron annihilation.

.

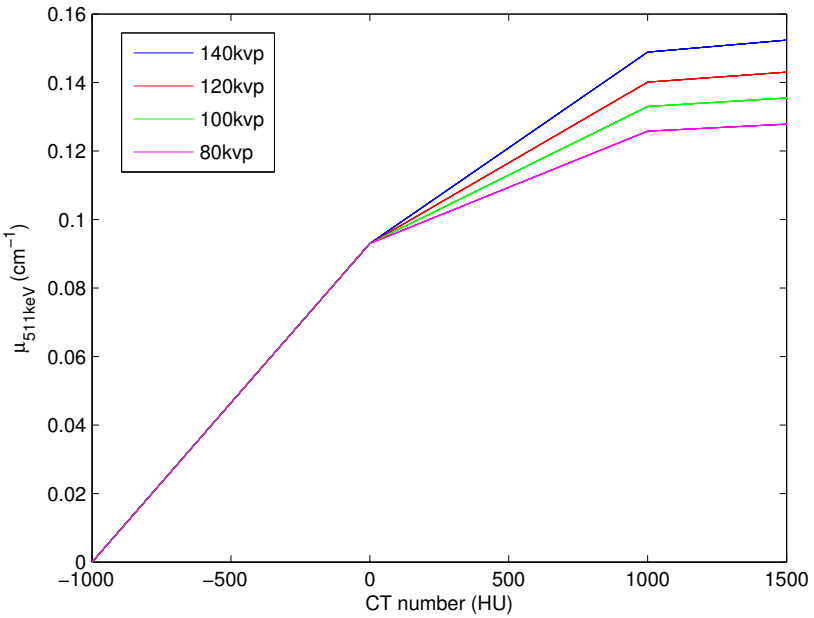

Figure 1.16: Multi-linear transforms used to convert CT images from HU to attenuation coefficients at 511 keV on a GE Discovery VCT. Transforms for 80 - 140 kVp shown over the range 0 HU to 1500 HU.

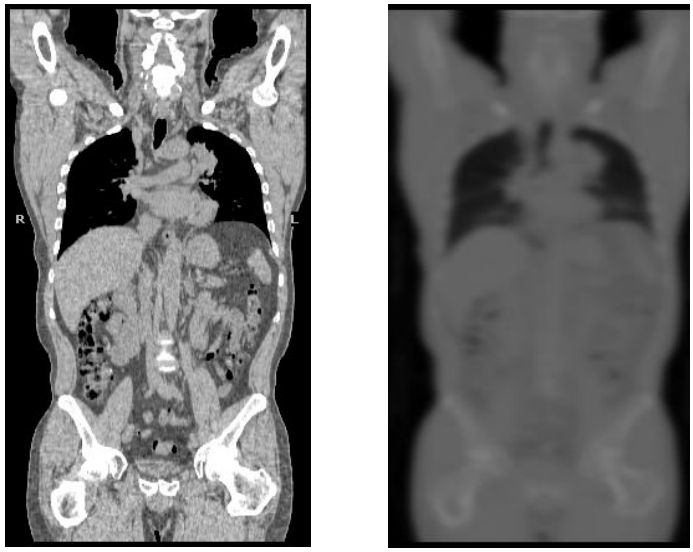

Figure 1.17: Helical CT image (a) and the corresponding CT attenuation correction map (b). The CTAC has been spatially filtered and transformed to μ_{511} values.

obtain a correction factor for acquired PET data.

1.1.4.2 PET/CT acquisition

For routine clinical whole body imaging, a helical CT image is usually acquired for anatomical information and for attenuation correction. The use of oral and intravenous CT contrast is often avoided because of the potential artefacts resulting from attenuation correction errors [3, 4]. On a GE Discovery VCT, a helical CT from the base of the brain to mid thigh can be acquired in less than 10 seconds using a rotation speed of 0.4 s, pitch of 1.375 and a beam width of 40 mm. Following the CT, a series of PET bed positions are acquired, where each bed position is usually 2-4 minutes in duration. Figure 1.18 illustrates a typical oncology half-body PET acquisition protocol.

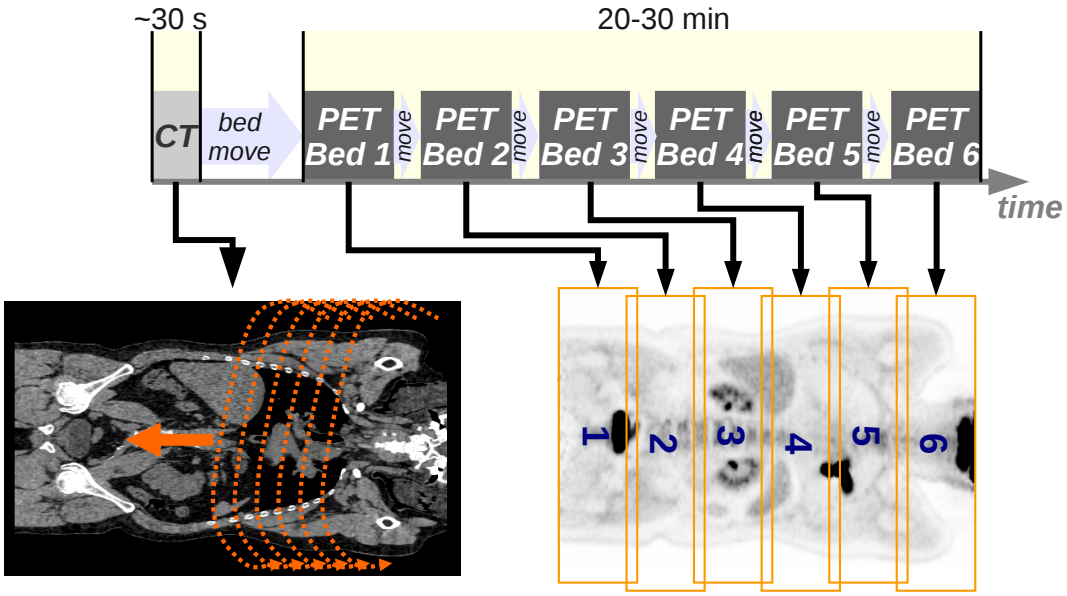

Figure 1.18: Illustration of PET/CT half body acquisition protocol. The CT is acquired in < 30 s, where as the overlapping PET bed positions typically take < 20 min min for the entire study.

To account for the non-uniform axial sensitivity across the PET field of view, each PET bed position overlaps by 25% to 50% when imaging in 3D mode. In 2D mode, where a more uniform sensitivity exists, this overlap is typically reduced to less than 10% of the axial extent.

1.1.5 PET/CT accuracy

Compared with other radioisotope-based functional imaging modalities such as SPECT, PET provides the ability to accurately correct for attenuation. Quantification of PET images is therefore possible, and some form of quantification is common in both clinical and research imaging.

For example, in the management of lymphoma treatment, FDG PET can be used to assess response to chemotherapy at the end of treatment [58] and to predict prognosis by acquiring PET scans mid treatment [44, 45, 55]. While response assessment from PET/CT images can be performed visually, response is often quantified [45, 55, 57, 95] and this has been shown to improve accuracy in predicting survival [78]. In clinical FDG PET imaging, quantification is generally

achieved with the standard uptake value (SUV). SUV describes the concentration of tracer in a localised region relative to the average concentration of FDG in the whole body. This is defined as

$$SUV = \frac{A_{ROI}w}{ID} \tag{1.5}$$

where A_{ROI} is the activity concentration measured in a region of interest defined on the image (decay corrected to the time of injection), and ID is the activity injected into the patient with body weight w.

Quantitative comparison of multiple imaging time-points relies on repeatable imaging techniques; a change in SUV could reflect either physiological response or error in the measurement. Several factors can affect reproducible SUV measurements, including uptake time [83] and patient blood glucose concentration [49], and these are considered when designing imaging protocols. Additionally, the stability and accuracy of imaging equipment contributes to SUV measurement reproducibility, and manufacturers stipulate quality control (QC) and quality assurance (QA) procedures accordingly. Detailed QC programs have also been developed for multi-centre trials [8, 12, 124], and these have been shown to reduce SUV variability [137].

Several factors contribute to loss in quantitative and qualitative accuracy in PET images. Quantification in PET is affected by partial volume effects. When the size of an object is smaller than twice the resolution of the scanner ($2 \times FWHM$), then the image-measured activity concentration in the object is inaccurate [22]. Further to this, as discussed in section 1.1.2.2, scatter and randoms contribute to image noise, and a direct analytical solution to these effects is not possible. Recent improvements to reconstruction methods have led to more accurate scatter and randoms correction and image noise reduction, however these phenomena still degrade image quality.

Attenuation (see section 1.1.2.1) causes a substantial loss of detected counts, and in PET imaging this loss can be corrected. However, this correction can be limited by the ability to accurately measure attenuation maps. A potential cause of errors in the generation of attenuation correction maps is patient respiratory motion.

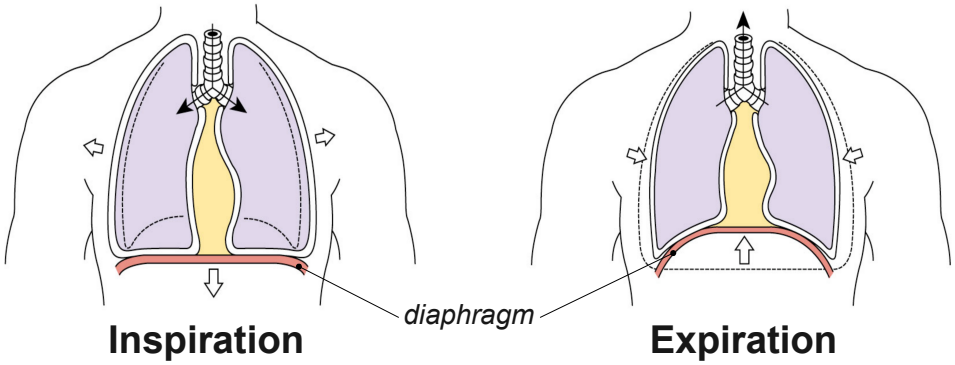

Figure 1.19: During inspiration, the diaphragm contracts and moves downwards, and the intercostal muscles move the chest wall upwards and outwards, increasing the thoracic volume. During expiration, these muscles relax and the thoracic volume is restored.

1.2 Respiratory Motion

The primary muscles involved with respiration are the diaphragm and the intercostal muscles. During inspiration, the diaphragm contracts and moves downwards, and the external intercostal muscles contract moving the chest wall upwards and outwards as illustrated in figure 1.19. This increases the thoracic volume which reduces pressure in the lungs, causing air to flow into the lungs. During exhalation, the muscles relax and restore the thoracic volume. This increases the pressure in the lungs, causing the evacuation of air.

During normal respiration, organ motion extends throughout the thorax and abdomen [73]. Expansion and contraction of the diaphragm causes displacement of the abdominal organs in the inferior and anterior direction [122]. Liver motion is predominantly in the superior-inferior (SI) direction and is typically 25 mm in amplitude, but can vary from 10 mm to 40 mm under normal respiration, and up to 80 mm during deep breathing [129]. Average kidney motion amplitude is 19 mm (range 10 mm to 40 mm) under normal breathing conditions, increasing

to 40 mm (range 20 mm to 70 mm) under heavy breathing [129]. Respiratory motion is also known to affect the prostate, creating 3.3 mm of movement on average, but up to 10.2 mm of motion is possible [86].

In the lungs, significantly more motion is present in the lower regions than the upper regions, and the presence of lung tumours can significantly reduce lung motion [112]. Lung tumours are affected by respiratory motion in a complicated manner in the SI, left-right (LR) and anterior-posterior (AP) directions [61], and can include hysteresis of up to 5 mm [123]. Respiratory induced movement of the heart is mostly in the SI direction, with approximately 18 mm of motion at the inferior margin and 16 mm at the apex [145].

1.3 Respiratory gating PET/CT acquisitions

As described in sections 1.1.2.5 and 1.1.3.1, PET and CT acquisitions can be gated according to an external periodic signal to produce a series of images, or gates, that represent one cycle of the signal. To gate for respiration, the external signal must represent the respiratory cycle.

1.3.1 Measuring respiration

To directly measure respiration, changes in lung volume can be determined with the use of a spirometer. These devices measure the entire volume of air inhaled and exhaled, so all breathing must be performed through hoses that attach to the device. As such, these devices are generally not practical for clinical imaging, and are often not tolerated well by patients [53]. An alternative approach is to measure a different parameter which can be used as a surrogate of respiration, and in most imaging applications the displacement of the abdominal or chest wall is used. This is usually measured with additional hardware, however methods which derive the respiratory signal directly from the acquired data itself have also been developed.

1.3.1.1 Hardware methods

Hardware based gating methods use physical measurements to obtain a respiratory signal. Typically, chest or abdominal wall movement is used as a surrogate for respiratory motion [67, 91], however the use of temperature sensors to measure airflow has also been demonstrated [13]. Currently, two hardware based methods of measuring respiration during PET/CT imaging are commercially available and supported by scanner manufacturers. Both of these systems use the physical displacement of the chest wall or abdominal wall to produce a 1-dimensional signal that represents respiration.

Anzai (Anzai medical co.,ltd, Tokyo, Japan) produce a device which uses a pressure sensor integrated into a belt that is fitted to the chest or abdomen. Varian (Palo Alto, CA) produce the real-time position management (RPM) system, which consists of an infrared camera that tracks the vertical displacement of a small reflective box which is placed on the abdominal or chest wall of the patient. The system records the respiratory signal, and produces a transistor-transistor logic (TTL) pulse once per respiratory cycle. This signal can be used to prospectively or retrospectively gate PET and CT acquisitions. The RPM system has been successfully used to respiratory gate CT [77, 108, 116, 136], PET [104], and combined PET/CT acquisitions [39, 99, 100].

Other hardware based methods have been developed for CT and radiotherapy which extract multi-dimensional respiratory data without requiring hardware that directly contacts the patient. The stereoscopic GateCT® system (Vision RT, London) acquires a dynamic 3D surface of the patient and can seperately measure the thoracic and abdominal components of respiration [130]. Time of flight cameras have also been used to produce a similar 3D dynamic surface map which can be used for respiratory gating [119].

Several limitations of hardware based gating must be considered. The cost of purchasing these devices, along with installation, staff training, and time required to configure each patient is not negligible. Additionally, the RPM device relies on an uninterrupted line-of-sight between the optical camera and the reflective box, and on static positioning of both the reflective box and the camera for continuous operation. Failure of these conditions is not uncommon, and in studies

by other groups a considerable number of RPM traces were unusable due to failure [80, 147].

To respiratory gate PET/CT acquisitions, the signal used for gating must represent the physical position of the anatomical region being imaged. These hardware based methods rely on the principle that anterior-posterior movement or circumferential expansion of the outer surface of the body describes all respiratory motion throughout the body. This is not necessarily always true, and movement of the outer surface of the body has been shown to provide an inaccurate indication of the movement of internal structures [42]. Lung volume measured with spirometry provides a better indication of lung tumour position than abdominal wall displacement, however both of these metrics have been shown to correlate poorly with tumour position in some cases [53, 107]. Time varying differences between spirometry derived lung volume and chest wall displacement measurements also exist, and a phase difference between the two measurements of 60° that reduces to 0° over 2 min has been shown [107].

1.3.1.2 Data-driven methods

An alternative to obtaining the respiratory signal from an external surrogate measurement is to extract the signal directly from the acquired imaging data itself. This removes the requirement for additional equipment, and potentially provides a more accurate signal given that the signal is derived from the moving structures in the field of view, rather than the movement of the outer surface of the body.

One method of obtaining motion information from an image is by locating pixels which represent the moving object, and integrating the value of these pixels over time to produce a time-counts curve. Visvikis et al demonstrated recovery of the respiratory signal from simulated phantoms, by defining regions of interest (ROIs) over regions of moving activity in reconstructed images [141]. A similar approach of defining ROIs over tumours in reconstructed dynamic frames, and using the centre of mass to determine the respiratory signal has also been demonstrated [15]. Both of these methods require reconstructed dynamic frames of short duration. A total of 5 min of PET data would require 3000 images, each

of 100 msec duration to be reconstructed, which is impractical in the clinical environment.

Several methods which derive the respiratory signal from raw, non-reconstructed data have been proposed. Schleyer et al developed a method for planar nuclear medicine scanning which uses a spectral analysis to determine which sinogram pixels are subject to respiratory motion [120]. These pixels are weighted according to the relative direction that motion locally occurs, and integrated over time to form the respiratory signal.

Kesner et al developed a related concept where all pixels in the raw data are considered, and the time-activity curve from each pixel is added, subtracted, or ignored such that the standard deviation of the combined time-activity curve from all pixels increases [63]. This has been shown to produce accurate respiratory signals comparable to hardware derived methods [62].

He et al developed a simple method which exploits the non-uniform sensitivity profile of the PET scanner and estimates the respiratory signal from the change in PET count rate over time [52]. Another similar technique considers the change of overall centre of mass of the counts in the raw PET data to represent respiratory amplitude [17]. While acceptable accuracy of these methods has been demonstrated with FDG cardiac PET data [17], both of these concepts assume that a single area of activity, such as the myocardium, is moving within the field of view during imaging. Unpredictable results are likely if another region of activity enters the PET field of view. For example, if 2 tumours exist, and one leaves the field of view as the other enters, then the net change in count rate would be zero.

A solution to this limitation was presented by Büther et al, who used a manually defined volume of interest (VOI) over the motion affected tumour on a reconstructed image [14]. The VOI was projected into sinogram space, applied to the raw dynamic PET data and the ROI centre of mass used to estimate the respiratory signal. Images gated with this approach recovered significantly more motion and produced significantly higher SUV_{max} measurements than the original centre of mass approach. Limitations remain however, as manual interaction is required, and a region of focal tracer uptake which is separated from any surrounding structures must exist.

Recently, Thielemans et al have produced a fully automated respiratory gating method for both PET and CT, which requires no *a priori* information [134]. This technique uses principle component analysis (PCA) of the raw PET data, which finds a set of orthogonal, basis vectors that explain temporal change in data. In six patient images, the first principle component was found to produce a signal which closely resembled a hardware derived respiratory signal. Requiring no *a priori* information, no parameter tuning is necessary for this technique. This method also offers fast processing, approximately 30 s is required for a single bed position PET image.

CT only data-driven gating methods have also been described. Pan et al. [108] produced a method which used manually defined ROIs on CT images acquired in cine mode. Regions were placed on structures known to move with respiratory motion including the diaphragm, sternum, rib cage and muscles under the skin. The summation of the CT numbers in these regions was used to estimate the respiratory cycle. An automated method for CT gating has also been developed by Zeng et al which uses an iterative sorting method to produce respiratory gated volumes from cine CT data [150]. This was shown to perform successfully on 5 patient datasets, and unlike the method from Pan, this requires no user interaction to define ROIs. Li et al also developed a method that sorts cine CT images into a respiratory sequence based on combining measures of lung air content, lung area, lung density and body area [76]. Compared with hardware gated images, this method demonstrated fewer image artefacts when irregular breathing occurred, however only phase based gating (see section 1.3.2) was possible because the respiratory signal from each individual CT bed position was of undetermined scale.

Another approach by Carnes et al sorts cine CT bed positions by maximising the normalised cross correlation of overlapping sections of the scan [18]. This provides a means of joining gated CT bed positions and was shown to reduce artefacts when compared with RPM gated images, however the inclusion of overlap increased the radiation dose by approximately 33% to 18 mSv.

In a different approach, Wu et al [148] acquired a reference helical CT over the thorax under breath hold, and a free breathing cine CT over the same region. Each slice of the cine CT series was registered to the reference CT, and

a respiratory signal was derived from the series of transformations at each cine CT bed position. A 4D CT sequence was then generated by applying the motion transformations to the reference CT.

1.3.2 Gating approaches

Most hardware and data-driven methods produce a 1-dimensional signal which represents the point in the respiratory cycle over time. In gated imaging applications, the physical position of the organs being imaged is usually required, and this must be derived from the 1-D respiratory signal. In gated cardiac imaging, the time point between two cardiac cycles is measured with an ECG and used to determine the point in the cardiac cycle. In the case of respiration however, the cycle duration can be consciously varied and temporal based referencing can result in portions of the cycle being discarded. To use the respiratory signal to gate PET acquisitions, usually either variable time, phase or amplitude divisions of the respiratory signal are used to indicate position. Alternatively, variable sized amplitude divisions can be used. These approaches are illustrated in figure 1.20 where 4 gates are used to simplify the diagram, and described as follows:

- **Time divisions** The average cycle duration is calculated and divided by the number of gates required. This determines the time duration of each gate, which are ordered sequentially and synchronised to the start of each cycle in the respiratory signal. If an individual cycle is longer than the average cycle duration, then the remainder of the cycle is discarded. Variations in the total volume inspired or expired, represented by the signal amplitude, are not considered with this approach. As such, data during an unusually deep breath is incorrectly combined with data from a smaller breath.

- **Variable time divisions** Rather than defining a gate duration based on the average cycle period, each individual cycle is is divided into equally sized temporal segments, starting from the point of maximum inhalation. Each gate is ordered sequentially and synchronised with the start of each cycle, and no data is discarded. Inter-cycle variations in respiratory amplitude are also disregarded by this approach.

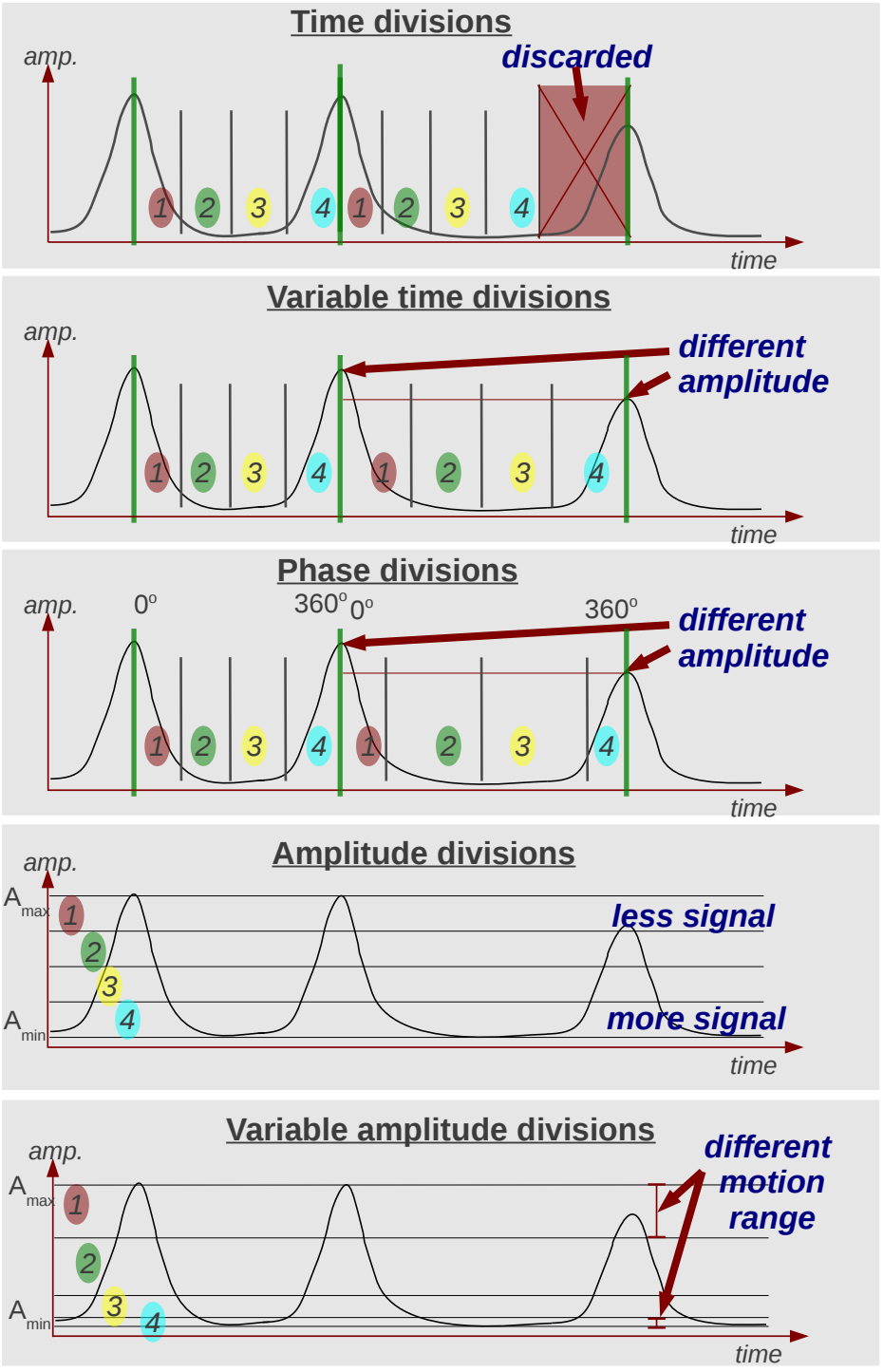

Figure 1.20: Illustration of gating methods. Gate numbers are determined by dividing the respiratory signal into time or variable time divisions, phase or amplitude divisions, or into variable amplitude divisions which maintains an equal amount of signal in each division.

- **Phase divisions** Each cycle is considered independently and gates are formed according to the phase in the cycle. This requires analysis of the curve shape to determine the point in the cycle. Variations in amplitude are not considered.

- **Respiratory amplitude divisions** Respiratory cycle duration and phase is disregarded, and signal amplitude is used to reference the point in the respiratory cycle by dividing the amplitude range of the respiratory signal into the number of gates required. Variations in either the depth of breathing or the cycle duration do not result in incorrect binning of data, and no data is discarded. However, the amount of time spent in each amplitude range (gate) can be different, for example more time can be spent at the expiratory phase than at full inspiration. In this case, the image gate that represents expiration will contain less noise than the inspiration gate. Additionally, data at a particular respiratory amplitude is summed, regardless of whether in the inspiratory or expiratory phase of the cycle. Hysteresis is therefore not considered by this approach.

- **Variable amplitude divisions** Rather than equally dividing the full amplitude range into gates, the range of each gate is varied to maintain an equal amount of time spent in each range. This produces gates with equal noise, however some gates represent a larger range of motion than others, resulting in a non-uniform distribution of motion blur in the gated images.

The advantage of amplitude based gating was demonstrated by Dawood et al [34], who found a 30% improvement in capturing motion when amplitude based gating was performed in comparison to time-based gating. The authors also suggested that varying the size of the amplitude gates produces more evenly distributed noise across the gates.

1.3.2.1 Gated CT limitations

The amplitude and period of respiration is known to vary from cycle to cycle in some cases [46, 84, 100, 123], even when coaching is used [100]. Both of these variations can cause artefacts in gated cine CT.

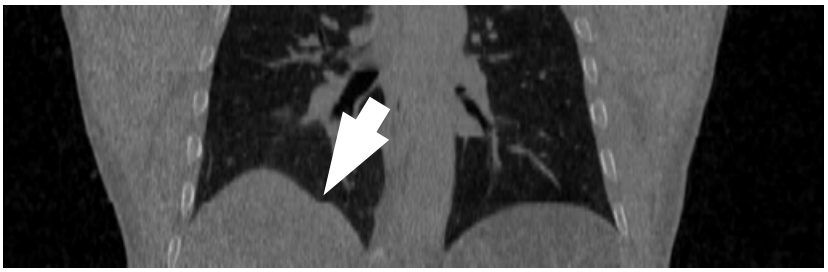

Figure 1.21: Example of artefact in gated cine CT that results from inter cycle variations in respiratory amplitude. A spatial discontinuity is seen on the superior edge of the liver.

For gated cine CT, each position is typically acquired for approximately 5-6 s to include at least one respiratory cycle. Variations in cycle duration can extend a single cycle beyond the cine duration such that a portion of the respiratory cycle is not acquired. This results in gaps in the gated sequence for some cine positions.

Similarly, inter-cycle variations in amplitude between different cine CT positions can produce errors. Where amplitude gating is used, this can result in missing data. Where phase based gating is used, gated cine positions can incorrectly represent a different amplitude of the motion cycle.

The resulting artefacts from these issues generally present as a discontinuity at the interface between cine CT bed positions. An example of this is shown in figure 1.21. McClelland et al developed a computational model to construct a single sequence of gates that represent an average respiratory cycle, largely overcoming artefacts that result from cycle to cycle variations [90]. This approach requires cine CT data acquired over several respiratory cycles however, and the increased patient dose resulting from the 20 s cine duration limits this approach to use in radiotherapy where the increased dose is low relative to radiation therapy treatment.

1.4 Respiratory motion and PET/CT Imaging

Dual modality PET/CT scanners acquire separate CT and PET acquisitions in series, in one imaging session. In the ideal case, where no patient movement exists, this results in spatially aligned PET and CT images. As described in section 1.1.4, the aligned CT is used for anatomical localisation and to produce attenuation correction maps for PET.

In clinical PET/CT imaging, a considerable difference in temporal resolution exists between the modalities. A helical CT which is used for anatomical localisation and attenuation correction is typically acquired much faster than the corresponding PET image. A CT scan acquired with a 40 mm beam width, a pitch of 1.5 and rotation speed of 0.4 seconds, would image 15 cm of the patient per second. Conversely, PET images are acquired as a series of discrete overlapping bed positions, each approximately 15 cm - 20 cm in length. Depending on the imaging protocol, each position is usually acquired for 2-4 minutes.

Considering that the respiratory cycle is, on average, 5 to 12 seconds [144], and each CT slice (typically 2.5 mm thick) is acquired in a fraction of a second, the CT approximates a *snap-shot* of part of the respiratory cycle. Each PET bed position, however, is acquired over several respiratory cycles, effecting an average of the respiratory motion over the duration of the scan. Two adverse effects are introduced as a result.

Firstly, the motion-averaging effect during the PET acquisition produces blur in the image. The extent of blur will depend on the amplitude and trajectory of the motion, however considering the resolution of reconstructed PET images is approximately 4 mm, the net effect is loss of spatial resolution [31] and spatial distortion of areas of focal tracer uptake.

Secondly, the disparity in temporal resolution between the sequentially acquired PET and CT scans can result in spatial mismatch between the two modalities. This loss of PET/CT alignment introduces error in localising PET uptake with the corresponding CT, and also, compromises the accuracy of the CT derived attenuation correction map.

A PET-CT spatial mismatch of an air-tissue boundary can result in the incorrect assignment of attenuation correction values, and on average 10.2 mm

Figure 1.22: A white band attenuation correction artefact, caused by PET-CT spatial mismatch, is seen at the diaphragm above the liver and spleen in the attenuation corrected PET image.

of respiratory motion induced spatial mismatch has been reported in the lower lung[27]. Attenuation correction of the lung with soft tissue μ values can result in over-correction, increasing the activity concentration of the over-corrected lung region in the PET images. Conversely, attenuation correction of the liver with lung μ values results in incorrectly decreased activity concentration in the under-corrected liver region in PET. This is can occur along the diaphragm when the CT is acquired during inspiration, and the liver position in the CT image is inferior to the liver in the PET data. This commonly results in a characteristic *white band* artefact [106]. An example of this is shown in figure 1.22, where the helical CT was acquired under free breathing and a white band artefact appears at the diaphragm above the spleen and liver.

Beyer et al found respiratory motion artefact in 98% of clinical PET/CT images acquired [11], although it is likely that some of these artefacts were due to acquiring CT images on now obsolete single and dual slice CT scanners. On single and dual slice CT scanners the narrow x-ray beam width limits the acquisition rate of the scan, and when the speed of the liver is greater than the speed that the patient moves through the scanner (in helical mode) then the dome of the

liver can appear in several slices of the image. This produces a *mushroom* artefact which can manifest as an attenuation correction artefact in PET [47].

Figure 1.23 contains an example of a clinical FDG PET scan demonstrating severe respiratory motion artefact. In the coronal images shown, no unusual uptake is present on the attenuation corrected PET (AC), whereas abnormal uptake in the dome of the liver is clearly presented on the non attenuation corrected (NAC) PET. This area of uptake in the liver corresponds with a structure of normal uptake in the AC image which appears to be in the mediastinum. Respiratory induced mis-registration of the diaphragm position has resulted in the superior section of the liver, including the tumour, being under-attenuation corrected with lung μ values.

Both motion blur and attenuation correction errors resulting from motion induced PET-CT mismatch can degrade the accurate representation of tumours in oncological PET images. Phantom experiments have shown that respiratory motion decreases tumour activity measured on motion affected PET images. The amount of reduction is inversely related to tumour size, and Boucher et al demonstrated a reduction in measured activity of 21.1 % for a 19.4 ml sphere and 41 % for a 1.2 ml sphere [13]. By including attenuating material similar to lungs into moving phantom studies, attenuation correction errors resulting from respiratory motion have been shown to further reduce the measured activity concentration of tumours to 75% [111].

In human imaging, Erdi et al showed that respiratory motion results in a reduction in SUVs of lung nodules by up to 30% and an over estimate of PET derived tumour volumes by up to 21% [39]. The magnitude of these effects depends on the amplitude of motion, tumour size, and the breathing pattern. These variables were characterised by Liu et al [80], who found smaller tumour size and larger amplitude of respiratory motion both contributed to a greater effect of respiratory motion on PET images. Liu also categorised 1295 patient respiratory traces according to the breathing pattern used, and found that PET images of patients who spent a large portion of the respiratory cycle at expiration phase were less affected by respiratory motion than images of patients with irregular breathing patterns.

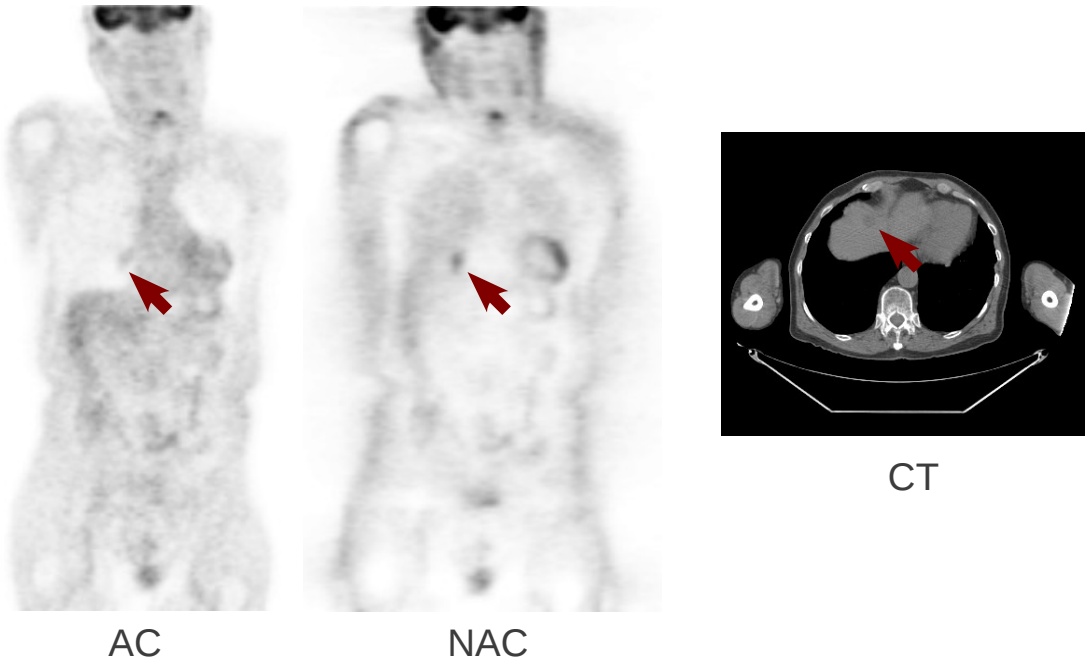

Figure 1.23: Example of respiratory motion artefact in FDG clinical imaging. PET-CT mismatch due to respiration led to the upper section of the liver being attenuation corrected with lung values. As a result the lung tumour, seen in the non attenuation corrected image and CT, appears as a lung mass of normal uptake in the attenuation corrected image.

1.4.1 Cardiac PET/CT Imaging

The heart undergoes both respiratory motion and cardiac contractile motion. Cardiac contractile motion can displace the left coronary arteries by, on average, 8 mm to 13 mm [127, 146], however displacement of up to 20 mm for the left coronary arteries, and up to 42 mm for the right coronary arteries has been shown [146]. This is comparable to respiratory motion, which produces approximately 16 mm to 18 mm of motion in the SI direction [145]

On dedicated PET-only scanners, respiratory motion and cardiac contractile motion, either combined or independently, can create artificial regions of significant heterogeneity in the myocardium [132]. This results from blurring during the PET acquisition. Combined cardiac and respiratory gating has been suggested as a requirement to produce reliable quantitative cardiac PET images [81, 132], and successful dual gating has been demonstrated with phantom, animal and patient studies [67, 69, 72, 131].

Further to this, respiratory motion induced artefacts that result from PET-CT misalignment have also shown to present in cardiac PET/CT imaging [94]. A spatial PET/CT misalignment of approximately 8 mm or more can lead to severe artefacts, producing false positive defects in up to 40% of cases [48, 88]. Artefacts typically appear as reduced uptake in the anterior and lateral walls, where spatial misalignment of the myocardium results in the incorrect use of lung attenuation coefficients to attenuation correct the myocardium. Bias in septal [93] and inferior [24, 48] walls have also been reported where liver misalignment exists, including over-correction where the liver position in the CT is superior to the liver position in the PET.

1.5 Approaches to reduce respiratory motion in PET/CT

Approaches to reducing the effects of respiratory motion can be generalised into three categories. The first, *type I*, attempts to produce a single attenuation correction map that more closely represents the average respiratory position in the corresponding PET acquisition. This reduces motion induced attenuation

correction errors by improving PET-CT alignment, but does not consider the effect of motion in the PET acquisition.

The second approach, *type II*, separates the PET and CT according to respiratory phase or amplitude, such that the PET and attenuation correction map both represent the same point in the respiratory cycle. This can be achieved by gating the PET and CT acquisitions, and then attenuation correcting each PET gate with the CT gate from the matching point in the respiratory cycle. This produces a series of attenuation corrected PET images with reduced artefacts from attenuation correction errors and motion blur, however distributing the acquired PET counts across the series of gates increases the noise in the individual image gates. Attenuation corrected gates can be summed to produce a single PET image with low noise and reduced attenuation correction artefacts, but retaining motion blur.

To reduce noise, motion blur, and attenuation correction artefact, the third approach, *type III*, uses motion correction to register and then recombine gated and attenuation corrected PET data into a single, motion-free image. Figure 1.24 summarises the three approaches including the standard method of using a helical CT for attenuation correction.

1.5.1 *Type I* - Breath hold CT

Maximum inspiration breath hold represents an amplitude of respiratory motion outside the range of normal respiration, and is therefore not suitable to attenuation correct a PET image which is acquired under free breathing. To produce a breath hold image which more closely represents the average respiratory position in PET, limited breath hold techniques have been proposed where the patient is instructed to breath hold on partial expiration. These methods have been shown to reduce spatial mismatch between PET and CT [11, 47, 144]. However, limited breath hold techniques are prone to error, and a PET-CT misalignment of more than 2cm image has been found in 34% of patients when this method is used [110]. Moreover, breath hold CT does not address respiratory induced blurring in the PET image.

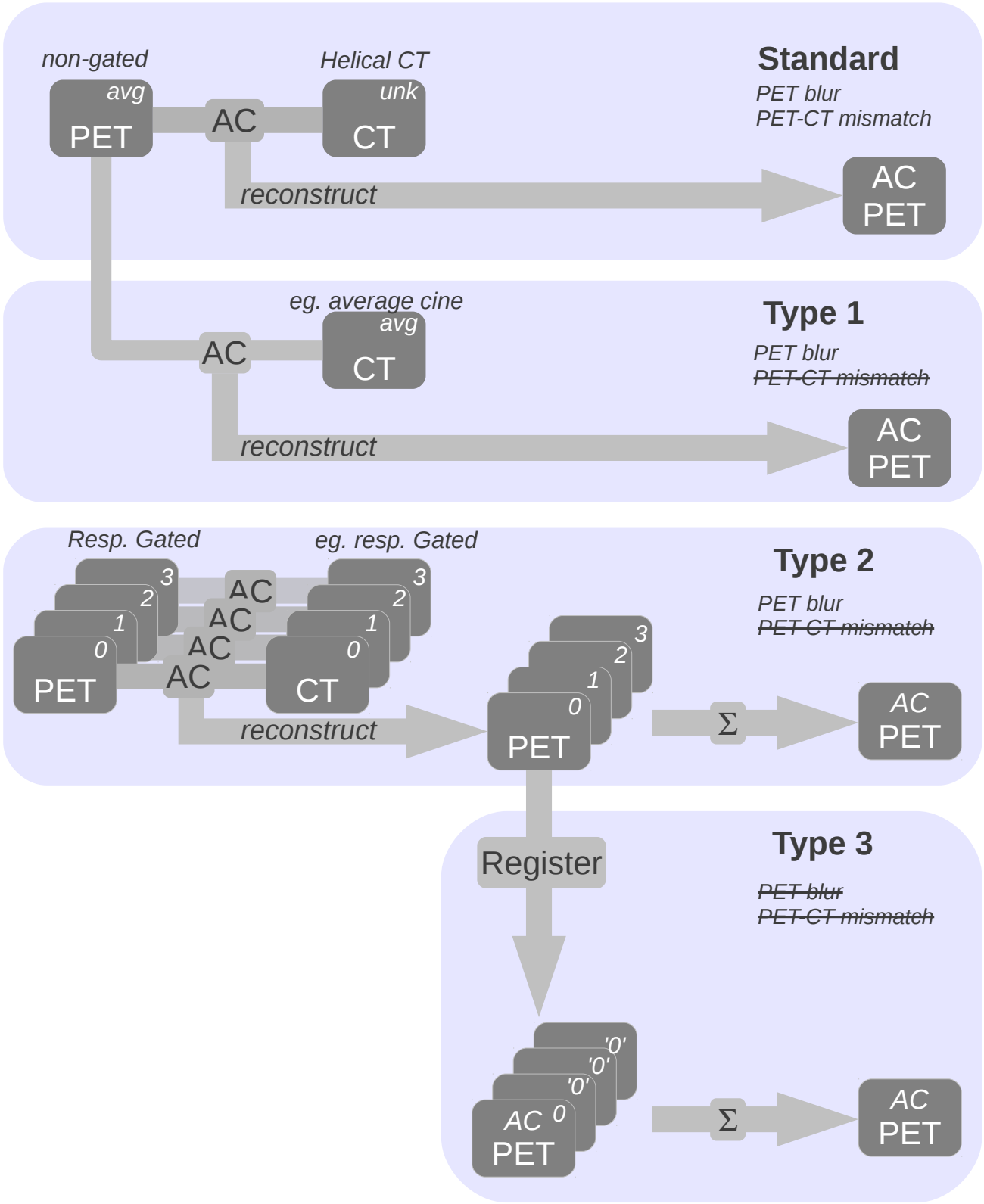

Figure 1.24: Summary of the three approaches to reducing respiratory motion artefact, including the standard method where a helical CT acquired at an unknown point in the respiratory cycle is used for attenuation correction.

1.5.2 *Type I* - Shifted helical CT

In cardiac imaging, visual alignment of PET images and helical CT scans can be achieved by translating the helical CT, and then attenuation correcting the PET data with the shifted CT. While manual [88] and automatic [64] translation of a helical CT has been shown to remove artefactual cardiac defects in NH_3 perfusion PET/CT images, Gould et al found that a helical CT can not always be transformed with rigid body translations to match the averaged respiratory position of the myocardium represented in PET [48]. The relative position of the liver and heart is known to vary during respiration, which is a source of artefact in PET [48, 93]. Rigid body translation of the CT does not account for this. Additionally, while the attenuation correction of the myocardium may be correct, mis-registration between the CT and PET of organs other than the heart are likely after a rigid body transformation is used to correct a non-rigid displacement. A further consideration is the operator dependence of the manual transformation which could reduce accurate reproducibility of the resulting image.

1.5.3 *Type I* - Slow rotation helical CT

One approach to acquiring a CT that approximates the average respiratory position, is to slow the CT helical acquisition so the image is acquired over several respiratory cycles. This is analoguous to rod-source transmission scans acquired for attenuation correction on stand-alone PET scanners, which are acquired over several minutes. In cardiac imaging, slow helical CTs of up to 29 s acquired during breathing have been shown to significantly reduce artefactual defects induced by PET-CT mis-registration when compared with fast helical CTs acquired at expiration breath hold [48, 105]. However, these CT images are prone to *layering* artefacts which can propagate to attenuation corrected PET images [48, 128].

Generally, a slow rotation CT can be acquired on most commercial PET/CT scanners and used to attenuation correct PET data.

1.5.4 *Type I* - **Averaged cine CT**

Another approach to producing a CT that represents the average respiratory position similar to rod source transmission acquisitions, is to average a series of CT slices that are acquired at different points in the respiratory cycle. Initially, this was demonstrated with respiratory phase-gated 4D CT data by Pan et al [110]. Pan retrospectively gated a cine CT into 10 respiratory phases, and averaged across all phases to produce the average CT (ACT). This was shown to reduce breathing artefacts, and improve tumour quantification. Replacing the thoracic component of a helical CT with the ACT significantly improved PET-CT alignment and reduced the associated white-band artefact over the lower right thorax in whole-body FDG PET imaging. A 50% or greater change in SUV was also found for 4 out of 13 tumours analysed. Two disadvantages arise from this method however. Firstly, using the suggested imaging parameters, the patients received a radiation dose of approximately 23 to 70 mGy from the extended CT imaging duration which is not practical for routine use. Secondly, additional respiratory monitoring hardware is required to acquire a gated CT.

A solution to both of these issues was later proposed by Pan, who generated the averaged CT from a low dose, non-gated cine CT [109], by averaging all slices acquired at each position regardless of the respiratory cycle. Using acquisition parameters of 10 mA and 120 kVp with a cine duration of 5.9 s, the patient dose was reduced to 5 mSv for a 15 cm acquisition. This approach was also demonstrated in canine cardiac imaging [29], and in human studies by Alessio et al, who used the average cine CT to attenuation correct myocardial perfusion PET/CT scans [2]. Alessio found that the ACT produced acceptable alignment in 77% of cases, however this improved to 88% when, rather than averaging pixels in the slice series, an intensity-maximum of each pixel was used. Alessio also noted a tendency for the ACT to under-correct where motion-blurred boundaries in the CT are converted to erroneous PET attenuation correction values.

Another solution to reducing the dose of ACT was investigated by Chi et al, who suggested that gated images representing fewer than 10 phases were required to produce the averaged CT [23]. Chi showed that reducing the number of phases used in the ACT to 4 (end inspiration, mid expiration, end expiration,

and mid-expiration), the tumour SUV and tumour volume measurements were only degraded by 1% and 2% respectively when compared with the 10 phase ACT. This reduced the dose from 50 mGy to 17 mGy, however prospective respiratory gating hardware was required which is not commonly available on commercial systems. Chi also compared the 10 phase ACT with averaged low dose cine (10 mA, resulting in 5 mGy), and found only a marginal decrease of SUV and tumour volume accuracy to 1% and 3% respectively.

Currently, most modern commercial PET/CT systems are capable of attenuation correcting PET with an averaged cine CT.

1.5.5 *Type II* - Selective PET acquisition

This concept involves recording PET data only during a desired section of the respiratory cycle, and discarding the remaining PET data. Two approaches have been suggested. Firstly, repeated breath holds during PET can accurately reproduce a consistent amplitude of respiratory motion. This was demonstrated in a study by Nehmeh et al [102], in which PET data from nine, 20 second, breath holds were summed, and attenuation corrected using a single breath hold helical CT. The 3 minutes of breath hold PET were acquired over, on average, a total of 6 minutes. The second approach is to allow the patient to breath freely during the PET acquisition, but to retain only the data which corresponds to the quiescent phase of the respiratory cycle [79, 101]. This method usually requires additional hardware to monitor the respiratory state of the patient during acquisition, and also extends the total acquisition time.

These methods are advantageous in that the PET data acquired is from a restricted range of the respiratory cycle which reduces the amount of respiratory motion in the PET image. The disadvantage, however, is that much of the PET data is discarded. A trade-off therefore exists between increasing total imaging time, increasing image noise, or increasing the amount of motion artefacts.

1.5.6 *Type II* - Respiratory gating

To avoid discarding PET data, respiratory gating can be used to separate an acquisition into a series of near motion-free images, each corresponding to a section

of the complete respiratory cycle (see section 1.1.2.5). The patient's respiratory signal, which is acquired during the acquisition, is divided into a continuous series of sections, referred to as bins or gates, according to either respiratory phase or amplitude, as described in section 1.3.2. Each imaging time point is then associated with the gate corresponding to the phase or amplitude section at the image time, by referencing the respiratory signal. By adding each imaging time point to the corresponding gate, the resulting sequence of gates represents one cycle of respiration.

By respiratory gating both CT and PET acquisitions, matched attenuation correction becomes possible [97, 99, 114]. In this, each PET gate is paired with the CT gate from the corresponding phase or amplitude section of the respiratory cycle. In the ideal case, each attenuation corrected PET gate is then free of respiratory motion induced PET blur, PET-CT spatial mis-alignment, and attenuation correction errors. Given that the effective acquisition duration of each gate is non-zero, some residual motion is still expected in each gate. Further to this, the CT and PET are not acquired simultaneously, and any variations in respiratory motion characteristics between the two modalities such as those described in section 1.3.2.1 could result in spatial PET-CT mismatch [100].

Respiratory gating of PET/CT therefore reduces motion blur in PET, and improves the accuracy of attenuation correction by reducing PET-CT mismatch. As a result, both quantification and volume definition of regions of focal tracer uptake should be improved. In phantom experiments, gated PET/CT was shown to reduce overestimated volumes, defined on PET images, from up to 370% overestimation in the non-gated images to within 1.5% of the true volume [97]. Gating phantom images also improves the spatial localisation of PET regions in CT, and improves the image-measured activity concentration by 17% to 75% [97, 111].

After validating a gating method with phantoms [98], Nehmeh et al performed respiratory gating on patient FDG PET images on a dedicated PET scanner, and investigated the effect on lung tumours [104]. Gating reduced lung tumour volumes by 14% to 35%, and increased tumour SUV_{max} by 7% to 156%. In a later study, Nehmeh et al [99] gated both PET and CT components and demonstrated respiratory matched attenuation correction, referred to as respiratory correlated attenuation correction. Compared with using helical CT for attenuation cor-

rection, respiratory matched attenuation correction improved spatial PET-CT registration by up to 41%, and increased SUV_{max} by up to 16%. When tumour volumes were defined on PET images, gating reduced the volumes by up to 42%. However when gated CT images were used for tumour volume definition rather than the helical CT, an increase in volume was found in 2 patients (up to 35%) and a decrease (up to -79%) was found on the remaining 2. A suggested reason for this discrepancy was the random nature associated with acquiring the helical CT during respiration. The structure could increase in size if the direction of respiratory motion was opposite to the bed motion, or decrease in size if it was in the same direction as the bed motion. However, this study was performed with a 10 mm beam width and a rotation speed of 0.8 sec/rot; this is comparatively slow relative to a modern 64 slice CT scanner which offers a 40 mm beam width and less than 0.4 sec/rot.

1.5.7 *Type II* - Pseudo gated CT

Gated CT introduces considerable additional dose to a routine clinical PET/CT acquisition because of the extended imaging duration required to capture the temporal information. A 16 cm cine CT over the chest acquired using 140 kVp and 10 mA with a cine duration of 5.5 s imposes a dose of approximately 3 mSv. A helical CT over the same region does not require an extended imaging duration, and if acquired at 140 kVp and 8 mAs which is suitable for CT attenuation correction [59], a radiation dose of approximately 0.5 mSv results.

As a low-dose alternative to a gated cine CT, an artificial or *pseudo* gated CT can be produced from a single low dose helical CT scan (non-dynamic). This can be achieved by deforming the helical CT to different points of the respiratory cycle such that in sequence, the deformed images include the full range of respiratory motion. Motion fields used to deform the helical CT can be derived from gated PET images, which are not corrected for attenuation to avoid bias resulting from PET-CT mismatch. This process is illustrated in figure 1.25, where the PET gate that matches the respiratory position of the helical CT is registered to the remaining PET gates. The resulting transformations are then applied to the helical scan to create the pseudo gated CT series.

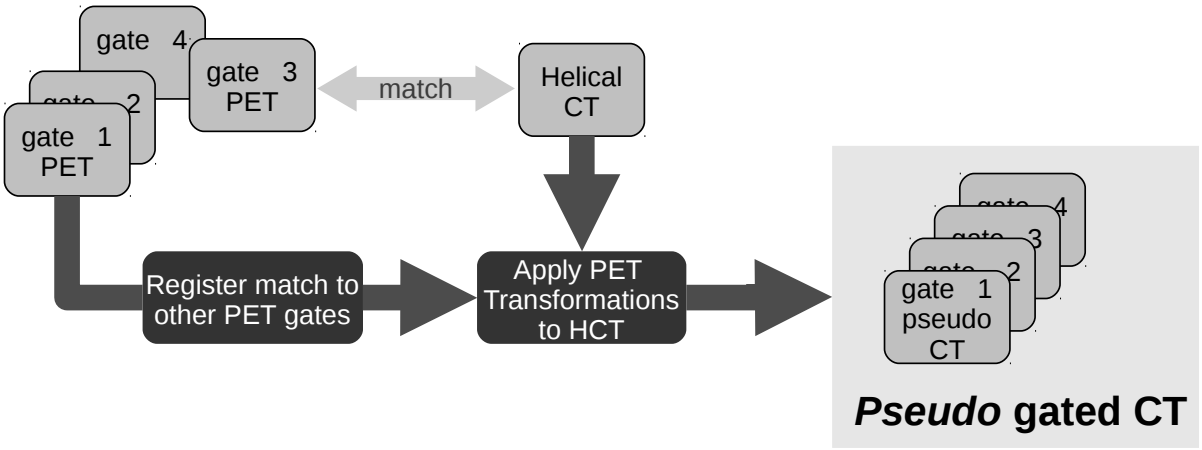

Figure 1.25: The PET gate which matches the respiratory position of the helical CT is registered to the remaining PET gates. A psuedo gated CT is produced by applying the resulting transformations to the helical CT.

This approach was demonstrated with simulated and patient data by Dawood et al, who used optical flow methods to derive non-rigid motion fields from gated PET data, and applied the transformations to a static CT [32]. Similar methods were also used in thoracic imaging by Fayad et al [41]. In cardiac PET/CT imaging, simple, manual rigid registration of the helical CT has been used to create pseudo CT data, however rigid body translation only accounts for cardiac misalignment and not misalignment of the liver or lungs [147]. A more complicated method using respiratory motion models described by McQuaid et al, has also been used to create pseudo gated CT data [92].

An additional benefit of generating a 4D CT from the PET motion fields, is the elimination of error introduced by an intra-cycle change in respiratory characteristics during the cine acquired for gated CT (see section 1.3.2.1). Further to this, an advantage of pseudo gated CT is also introduced where data-driven respiratory gating is used for PET. By removing the requirement for a cine CT, the possibility to retrospectively produce 4D PET data with respiratory matched attenuation correction from a routine clinical imaging protocol is introduced.

Importantly, however, accurate generation of a pseudo gated CT relies on good spatial alignment between the helical CT and one of the gated PET frames.

This may not occur if the patient takes an unusually deep breath during the helical CT acquisition.

1.5.8 *Type III* - Motion correction

Gated PET acquisitions provide motion-reduced frames, which in sequence, represent a single respiratory cycle. While the blurring and attenuation correction errors induced by respiratory motion are corrected in the individual gates, the counts collected in the acquisition are divided across all of the gates. Greater noise is therefore expected in the gated frames when compared with the non-gated image. This is demonstrated in figure 1.26, which shows increased noise in a single frame of a gated image compared with the non-gated image containing all counts. The variation of noise across the entire gated sequence is highlighted by the standard deviation of a region of interest placed over the liver on each PET gate.

As a result of the increase in noise, the loss of imaging statistics in gated images compromises the benefits of the gating [140]. It would therefore be desirable to produce a motion-free image of comparable imaging statistics to the non-corrected image, without extending imaging time.

This can possibly be achieved by motion correcting and combining gated data. There are several approaches to this concept. In one approach, gated PET data that have been attenuation corrected and reconstructed can be registered and then summed to produce the single, motion corrected 3D image, or alternatively, the registration can be included into the reconstruction step.

In the first approach, PET sinogram gates are attenuation corrected with the matching CT gate, and reconstructed. One PET gate is identified as a reference, to which all remaining gates are registered. By summing the motion corrected gated images, a single image is produced, providing similar noise characteristics to the non-corrected image. Kinahan et al demonstrated a significant reduction in PET image noise by summing registered and phase-matched attenuation corrected PET images with simulated data [65]. This approach is simple to implement, however a caveat is the non-linear nature of iterative reconstruction, i.e. summing sinograms and then reconstruction is not necessarily equal to re-

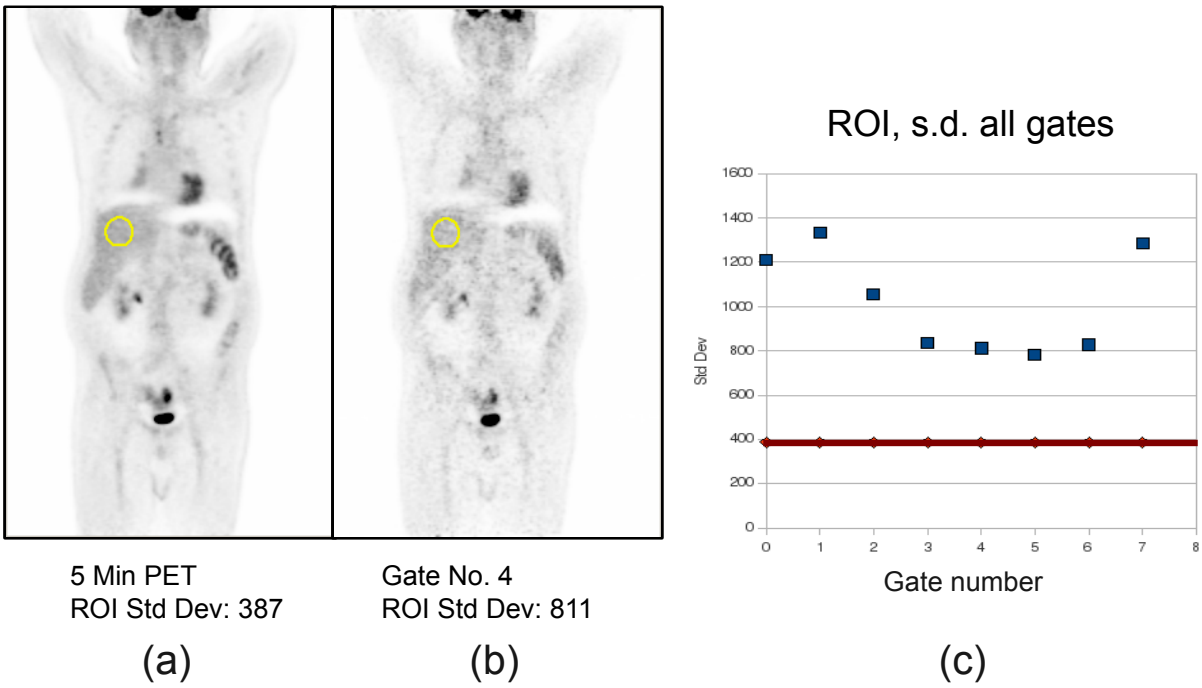

Figure 1.26: (a) Non-gated 3D FDG PET acquired at 5 minutes per bed position, demonstrates less noise than gate 4 from the amplitude gated sequence (b). (c) The standard deviation of the liver ROI shown for each gate (blue squares), and the standard deviation measured on the non-gated image using the identical ROI (red line).

constructing and then summing.

To overcome this issue, motion fields describing respiratory motion can be included in the system matrix used to iteratively reconstruct the PET data. This approach utilises all acquired PET data in the reconstruction step rather than reconstructing each gate separately, and results in reduced image noise. This method has been shown to produce more quantitatively accurate PET images in comparison to registering and summing gated PET images [87, 133]. Motion fields can either been obtained from gated CT images [71, 77, 115] or from non-attenuation corrected PET images [33].

1.5.9 Summary

Respiratory motion introduces 2 degrading effects in PET/CT imaging, attenuation correction errors that result from PET-CT mismatch, and motion blur in PET. Various approaches to reducing respiratory motion artefacts have been described, and all *type I* and *type II* methods consider only PET-CT mismatch. *Type I* approaches attempt to produce a CT that closely matches the average respiratory position in PET. CT breath hold techniques achieve this however they are prone to error, and while manually shifted CT images can improve PET-CT alignment, non-rigid deformations are not accounted for and this can result in artefacts. Alternatively, a CT that is acquired over several respiratory cycles can be acquired with a slow rotation CT, or by averaging a cine CT which is less prone to artefacts. Averaged cine CT methods impose a large patient radiation dose, however they are advantageous in that no user-interaction is required and most modern PET/CT scanners support this approach.

Type II approaches reduce attenuation correction artefacts by gating the PET image and attenuation correcting each PET gate with a CT image from a matching point in the respiratory cycle. This is possible with gated cine CT and gated PET, however gated cine CT imposes a large patient dose and the images are prone to artefacts that result from inter-cycle variations in the respiratory cycle. Alternatively, a *pseudo* gated CT can be produced by deforming a low dose helical CT to match each respiratory position of the gated PET series. This resolves both limitations of gated cine CT, however the low dose helical CT must match the

respiratory position of one PET gate, and motion fields that accurately describe respiration must be obtained from the gated PET image series.

Individual frames of gated and attenuation corrected PET images created with the *type II* approach contain reduced motion blur and reduced attenuation correction artefacts, however image noise is increased. Gated images can be combined to reduce the image noise, however motion blur is then reintroduced.

Both attenuation correction errors and motion blur are considered with the *type III* approach. In this approach, PET images are gated, and attenuation corrected with matching gated or pseudo gated CT data, and then registered to a common point in the respiratory cycle. When these images are combined, this approach produces a single, motion corrected image of similar statistics to the original, non-corrected image. While this approach potentially provides an ideal solution to respiratory motion, it relies on accurate motion fields derived from either gated PET or CT images.

1.6 Objectives of this work

Modern PET scanners can provide a resolution of approximately 4 mm (transaxial resolution of a GE Discovery 710 using *VUE Point HD* reconstruction), and the blurring effect of respiratory motion, which can be over 2 cm at the diaphragm, can reduce the effective resolution of affected images. Respiratory induced attenuation correction and localisation errors further degrade PET/CT image quality. Several approaches to reduce the effects of respiratory motion have been discussed above and for the majority of these, respiratory gating is required to achieve motion corrected images without extending imaging duration or increasing image noise.

Respiratory gating methods can separate PET and CT images into a sequence of near motion-free gates which represent one respiratory cycle. PET and CT gates can be matched so that each PET gate is attenuation corrected with CT data from the matching section of the respiratory cycle, providing a means to overcome respiratory related attenuation correction artefacts. Non-rigid motion correction can then be used to align and combine gated and attenuation corrected PET data into a single, motion-free frame, of equal or similar statistics to the

non corrected image.

Data-driven gating methods offer advantages over hardware based methods, however, apart from the very recently developed method from Thielemans et al [134] published after the related work in this dissertation, no single data-driven gating method exists for both PET and CT. The first objective of this work, described in chapter 2, was to develop and validate a fully automated data-driven respiratory gating method for PET and CT imaging. Validation was performed by comparing the data-driven method with a hardware based method using phantom images and 4 single bed position 2D PET/CT images of lung cancer patients.

In clinical PET imaging, typical protocols include multiple bed position 3D PET acquisitions, and the second aim of this work was to extend the gating method to operate with these data. In chapter 3 the modifications required to gate 3D PET data, and a method to join the separately acquired PET positions are described.

Helical CTs are typically used for attenuation correction, and a respiratory induced spatial mismatch between the helical CT and PET has been shown to produce erroneous results. In cardiac PET/CT imaging, these errors can lead to clinically significant artefacts. Several approaches of reducing these errors have been suggested, of varying complexity, however a direct comparison using clinical data has not been performed. The third aim of this work was to compare and evaluate methods from each category described in section 1.5. This is described in chapter 4, where 60 cardiac perfusion NH_3 PET/CT scans were used to evaluate 4 approaches of correcting for respiratory motion. An average cine CT was used as a *Type I* approach, and data-driven gated PET and cine CT with matched attenuation correction formed a *Type II* approach. Given the disadvantage of cine CT in regard to increased patient radiation dose, a *pseudo* gated CT was generated from a helical CT to produce a second *Type II* method for evaluation. Non-rigid registration of both gated CT and pseudo gated CT attenuation corrected PET image datasets were performed to evaluate a *Type III* approach.

Finally, concluding remarks and commentary on future work are discussed in chapter 5.

Chapter 2

Data-Driven Respiratory Gating for PET/CT Imaging

2.1 Introduction

Respiratory motion has been shown to be a cause of artefact in PET/CT imaging. Relative to the respiratory cycle, the long imaging duration in typical PET protocols results in blurring. Additionally, respiratory induced spatial mismatch between PET and the corresponding CT result in incorrect anatomical cross referencing and erroneous attenuation correction. Combined, these effects qualitatively and quantitatively impact on clinical PET/CT scans.

Respiratory gating divides an acquisition into a series of motion reduced frames which, sequentially, represent one respiratory cycle. These frames are approximately free of motion, and the series of frames provides additional temporal data describing the trajectory of structures subject to respiratory motion. By gating PET acquisitions, respiratory induced blurring is reduced in each frame, and attenuation correction errors can be reduced by matching each PET gate with gated CT images. Several hardware based gating techniques exist for PET and CT such as the Varian RPM system described in section 1.3.1.1, which estimates the respiratory state by measuring a physical parameter of the patient, however these have been shown to be potentially inaccurate [42, 80, 147] and require additional hardware to be configured prior to imaging. Alternatively, data-driven

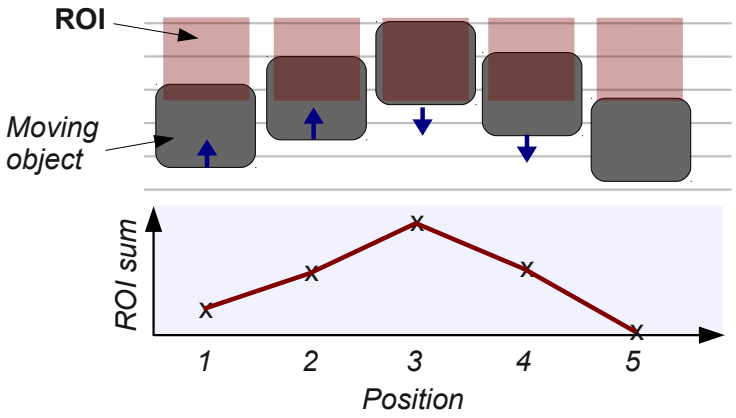

Figure 2.1: The sum of values in an ROI placed over the edge of the moving object represents the amplitude of displacement.

gating techniques can be employed which use the acquired data itself to estimate the respiratory state. This can provide a direct estimate of the respiratory state of a moving region from analysis of the region itself.

In this chapter, the basic principles of a method previously developed by Schleyer for planar gamma camera and SPECT imaging [120] were adapted to produce a data-driven gating system for both PET and CT. This method relies on the principle, as do methods from Visvikis [143] and Pan [108], that if the edge of an object moves within a defined region on a dynamic scan, then the integrated counts within the region will vary approximately linearly with the displacement of the edge. This is illustrated in figure 2.1.

Rather than manual definition of these regions, the method developed by Schleyer uses a spectral analysis to automatically define masks that consist of pixels in planar images or SPECT projections. The sum of the pixel values within the mask over time produce an estimate of the respiratory signal for the patient. As leading and trailing edges of a moving object could both contribute to the signal, the method weights the masked pixels according to phase to prevent cancellation of the two opposing signals (see section 2.2.1.1). In this work, these principles have been used to produce a method that gates raw PET acqui-

sitions and CT images. A major advantage of this new method is that the PET component of the processing is performed in sinogram space, which removes the requirement to reconstruct large numbers of dynamic PET volumes. The gating method was validated against a hardware based method with single bed position 2D PET and corresponding cine CT data from 4 lung cancer patients.

2.2 Methods

The data-driven gating method requires dynamic PET and CT data. Regions within the data which are likely to be subject to respiratory motion are determined by analysing the Fourier spectrum of each image or sinogram pixel. A pixel which lies on a non-homogeneous region which is subject to periodic motion, will exhibit a peak in the frequency spectrum for that pixel - at the dominant frequency of the periodic motion. This principle is used to define motion affected regions within the data, and the total counts in these regions over time is used as an estimate of the respiratory signal.

The technique consists of two steps: 1- The localisation of respiratory motion in sinogram space, generation of weighted masks and extraction of the respiratory signal; 2- Binning the original list mode PET or cine CT data according to the estimated respiratory signal. This section describes the PET specific gating technique followed by the CT specific gating technique.

2.2.1 PET Data-Driven Gating technique

PET data is acquired in listmode, and spectral analysis, mask generation, and signal extraction are performed in sinogram space.

2.2.1.1 Spectral analysis, mask generation and signal extraction

The listmode data is unlisted into a 4D sinogram $p(r, z, \theta, t)$, with a temporal period of T, where θ defines the 2D angle of the projection. A 4D Gaussian kernel is then applied to the data to reduce high frequency spatial and temporal noise,

$$p_s(r, z, \theta, t) = p(r, z, \theta, t) \star H \tag{2.1}$$

where $p_s(r, z, \theta, t)$ defines the smoothed sinogram series, and H is the 4D Gaussian kernel.

The Fourier transform of the smoothed sinogram series is calculated in the temporal domain only by using the Fast Fourier Transform (FFT) [30]

$$P_s(r, z, \theta, u) = FFT\{p_s(r, z, \theta, t)\} \tag{2.2}$$

where u is the index of the Fourier transform and relates to the frequency component f of the signal by

$$f = \frac{u}{TN} \qquad (Hz); \qquad \{u \mid u\epsilon\mathbb{N} \mid [0, \frac{N}{2} - 1]\} \tag{2.3}$$

for even values of N, where N is the number of samples in the series.

To identify pixels in the data which are likely to be subject to respiratory motion, a spectral window and threshold is applied to the magnitude spectrum at each pixel location (r, z, θ). The spectral peak within this window is denoted as Λ, such that

$$\Lambda(r, z, \theta) = max\{|P_s(r, z, \theta, u)|\} \qquad \{u \mid u\epsilon\mathbb{N} \mid [\upsilon_1, \upsilon_2]\} \tag{2.4}$$

where υ_1 and υ_2 are the lower and upper indices of the spectral window respectively. If the ratio of $\Lambda(r, z, \theta)$ to a reference value $\lambda(r, z, \theta)$ is above a given threshold κ, then the sinogram location (r, z, θ) is assumed to exhibit respiratory motion characteristics, and is included in the initial binary mask $A_{init}(r, z, \theta)$.

$$A_{init}(r, z, \theta) = \begin{cases} 1 & if \quad \frac{\Lambda(r,z,\theta)}{\lambda(r,z,\theta)} \geq \kappa \\ 0 & if \quad else \end{cases} \tag{2.5}$$

where the reference value λ is defined as

$$\lambda(r, z, \theta) = mean\{|P_s(r, z, \theta, u)|\} \qquad \{u \mid u\epsilon\mathbb{N} \mid [\upsilon_3, \frac{N}{2} - 1]\} \tag{2.6}$$

and predetermined value υ_3 is the start of the reference window that represents frequencies higher than expected respiratory values. The value of κ is determined iteratively so that a pre-determined proportion of the mask is filled. A value for

κ is calculated for each projection angle θ.

The spectral index location u_{peak}, of the maximum value within the window, Λ, is calculated for each sinogram location where κ is exceeded. The most commonly occurring peak index is then determined,

$$u_{resp} = mode\{u_{peak}(r, z, \theta)\} \tag{2.7}$$

and is assumed to be the index of the dominant frequency component of respiration f_{resp}. The binary mask $A_{init}(r, z, \theta)$ is then refined to only include pixels where $u_{peak}(r, z, \theta)$ falls within a restrictive window around the respiratory frequency

$$u_{resp} - \delta < u < u_{resp} + \delta \tag{2.8}$$

where δ is a pre-determined value which defines the size of the restrictive index window. This forms the binary mask, $A(r, z, \theta)$ which eliminates pixels in the sinograms which are not subject to respiratory motion. The spectral windowing and thresholding method is shown graphically in figure 2.2.

The integrated counts within the regions in the mask will vary approximately linearly with the displacement of an edge moving within the region. Factors such as blurring of the edge, curved trajectories, and incorrect definition of the mask will in practice degrade this relationship. However as demonstrated below, the integrated counts in the mask over time does correlate with a physical measure of displacement. If we consider the case where the leading and trailing edges of an object both move across regions in the mask, then the two edges would generate opposing signals in the overall integrated counts series, which would act to cancel each other out. Phase discrimination is therefore required to sensitize the mask to relative phase differences within the data.

The phase of $P_s(r, z, \theta, u)$ is found at the dominant frequency u_{resp} for all pixels that meet the criteria in equation 2.8,

$$\phi(r, z, \theta) = arg\{P_s(r, z, \theta, u_{resp})\ \ A(r, z, \theta)\} \tag{2.9}$$

A histogram of the phase values ϕ is calculated using a histogram bin size of $\frac{\pi}{8}$, and the dominant phase at f_{resp} is found at the histogram peak, Φ_{max}. A

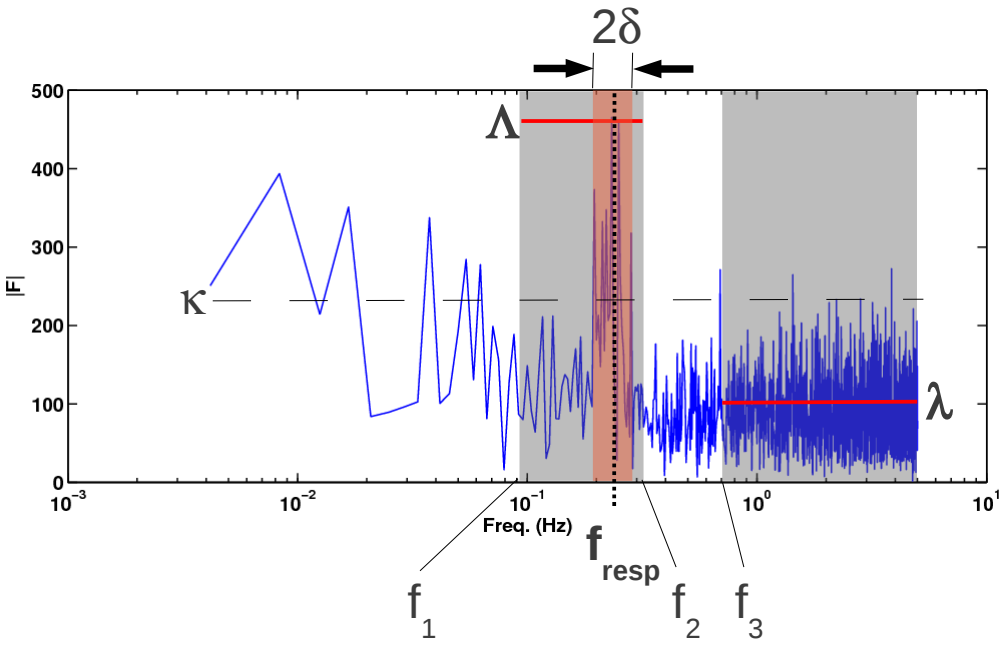

Figure 2.2: Typical magnitude spectrum for PET, detailing the initial spectral window f_1, f_2 and the peak Λ within the window, the reference window f_3 and mean reference value λ, and the threshold κ. Overall values f_{resp} and the associated restricted window $f_{resp} - \delta < f < f_{resp} + \delta$ are also shown.

weighting system is then used to penalise the mask's regions that associate with edges not moving in phase with the edge related to Φ_{max}.

$$\Omega(r, z, \theta) = cos(\phi(r, z, \theta) - \Phi_{max}) \tag{2.10}$$

which defines the phase weighted mask Ω. A region associated with an edge moving exactly in phase with Φ_{max} will receive a weight of 1, and one moving 180° out of phase to ϕ_{max} will receive a weight value of -1. This allows both leading and trailing edges of a moving object to constructively contribute to the respiratory trace, and points which are of phase orthogonal to Φ_{max} are ignored. Figure 2.4 shows an example phase weighted mask for the first projection angle of the phantom experiment.

Finally, an estimate of the respiratory trace, $r(t)$, is then produced by applying the phase weighted mask to p_s, and summing the counts in each sinogram,

$$r(t) = \sum_{r=0}^{r_{max}-1} \sum_{z=0}^{z_{max}-1} \sum_{\theta=0}^{\theta_{max}-1} p_s(r, z, \theta, t)\ \Omega(r, z, \theta) \tag{2.11}$$

where r_{max}, z_{max} and θ_{max} are the dimensions of the sinogram.

2.2.1.2 Binning

Amplitude binning is used to unlist the listmode data into B bins. A low pass filter with cutoff frequency of f_{resp} is applied to $r(t)$ to reduce high frequency noise, and outliers are removed by applying a 95% histogram threshold. The resulting series $r_s(t)$, is then divided into B equally spaced amplitude divisions, and a sinogram bin created for each amplitude division. Each original listmode event is unlisted into the sinogram bin which corresponds to the amplitude division that the smoothed trace intercepts at the time of the list mode event. This creates B near motion-free sinograms.

2.2.2 CT Gating

CT data is acquired in cine mode which produces a continuous time-series of images at each scanned location (see section 1.1.3.1. Images are separated by

sampling period T seconds resulting in a total of N reconstructed images per z location, where z increases in the superior to inferior direction. Depending on the CT camera design and the collimation settings used, S images over the z dimension are acquired simultaneously, which is referred to as a bed-step. Therefore a scan covering a distance of l mm in the z-direction would be acquired in $l/(SW)$ bed steps, where W is the x-ray beam width. Images at a given bed location, are acquired for the total cine duration until the bed moves to the next position to acquire the next spatially contiguous series.

Gating reconstructed CT images rather than projections reduces the temporal resolution of the data to the rotation time of the tube (if images are reconstructed with 1 full rotation per slice). However, projection data from most CT cameras is not easily accessed, so in this work CT image data is gated. Each bed step is analysed individually, however u_{resp} as described in equation 2.7 is determined globally by assessing all bed steps. A single bed step is described as

$$g(x, y, z, t) \qquad \{z \mid z\epsilon\mathbb{N} \mid [0, S-1]\} \tag{2.12}$$

Prior to spectral analysis, a 2D low pass filter is applied by convolving the series with a Gaussian filter, $H(x, y)$. Images are thresholded such that CT values below K_{min} are set to 0, and CT values above K_{max} are held at K_{max}

2.2.2.1 Spectral Analysis - CT

The FFT is calculated in the temporal domain for the time-series produced at a bed position

$$G_s(x, y, z, u) = FFT\{g_s(x, y, z, t)\} \tag{2.13}$$

where $g_s(x, y, z, t)$ describes the filtered and thresholded image series at a bed location, and the index of the FFT, u, is described by equation 2.3. Analogous to section 2.2.1.1, the peak of the spectral window is found,

$$\Lambda(x, y, z) = max\{|G_s(x, y, z, u)|\} \qquad \{u \mid u\epsilon\mathbb{N} \mid [\upsilon_1, \upsilon_2]\} \tag{2.14}$$

Translating equation 2.5 to the image domain, if the ratio Λ to the reference value λ is greater than a given threshold κ, then the pixel (x, y, z) is included

in the binary mask $A_{init}(x, y, z)$, where λ represents the higher frequency range starting at the pre-determined value υ_3 for a given bed location. The value for κ is determined iteratively as described in section 2.2.1.1, such that a pre-determined proportion of the image space is included by the mask. A value for κ is determined for each image bed location.

The most commonly occurring peak location within the window Λ is found where κ is exceeded at each image pixel, across all bed locations,

$$u_{resp} = mode\{u_{peak}(x, y, z)\} \qquad \{z \mid z\epsilon\mathbb{N} \mid [0, Z-1]\} \tag{2.15}$$

where Z is the total number of z-locations acquired over all bed positions.

The binary mask is then restricted according to equation 2.8. To phase weight the mask, the phase angle, ϕ, at each pixel in the masked data is found at the respiratory frequency u_{resp},

$$\phi(x, y, z) = arg\{G'_s(x, y, z, u_{resp})\} \tag{2.16}$$

where G'_s is the result of applying the binary mask to G_s. The most abundant phase at each bed position is then found,

$$\Phi_{max} = mode\{\phi\} \tag{2.17}$$

and a phase weighted mask is generated for each bed position

$$\Omega(x, y, z) = cos(arg\{G'(x, y, z, u)\} - \Phi_{max}) \tag{2.18}$$

The phase weighted mask is then applied to the pre-processed CT series g_s, to produce a respiratory curve segment for each z position of the bed location,

$$\rho(t, z) = \sum_{x=0}^{x_{max}-1} \sum_{y=0}^{y_{max}-1} g'_s(x, y, z, t) \tag{2.19}$$

where x_{max} and y_{max} are the reconstructed image dimensions, $S - 1$, and g'_s is the result of applying phase weighted mask Ω to g_s. The mean curve, $\hat{\rho}(t)$, is calculated to produce the respiratory curve segment for the bed location.

2.2.2.2 Binning - CT

Each segment of the respiratory cycle is sampled over a unique time period and is extracted from a unique anatomical dataset, resulting in an arbitrary relationship between the dominant phase Φ_{max} measured at each bed position. As $\hat{\rho}$ is related indirectly to displacement, an increase in $\hat{\rho}_1(t)$ for bed position 1 may therefore relate to motion in the $+z$ direction, whilst an increase in $\hat{\rho}_2(t)$ for bed position 2 may relate to motion in the $-z$ direction. This is detailed in figure 2.3. A relationship between the change in HU values of the masked images and the direction of motion is therefore required for each bed position. To determine this relationship, $\hat{\rho}(t)$ is used to sort the images into ascending order of amplitude. These images are then thresholded such that pixels less than -624 HU are set to 0 and pixels above -624 HU are set to 1. This provides an image which consistently defines the outline of the body surface.

The mean level of the anterior wall, and mean distance between the left and right walls is calculated at each slice series of the amplitude-sorted cine CT image series $f(x, y, z, t)$,

$$Y(z,t) = \frac{\sum_{x=0}^{xdim-1} max_y g(x,y,z,t)}{xdim} \tag{2.20}$$

$$D(z,t) = \frac{\sum_{y=0}^{ydim-1} max_x f(x,y,z,t) - min_x f(x,y,z,t)}{ydim} \tag{2.21}$$

where min_x and max_x find the location of lowest and highest non-zero pixels in the image $f(x, y)$ in the x direction, and max_y finds the maximum non-zero location in the y direction. A straight line is fitted to the diagonal component of the points, $\sqrt{Y^2 + D^2}$. The sign of the resulting gradient, ∇_ζ determines the direction of motion with respect to change in amplitude of $\hat{\rho_\zeta}(t)$, at bed location ζ. Where necessary, $\hat{\rho(t)}$ from each bed position is inverted such that $sgn\{\nabla_\zeta\}$ remains constant for all ζ.

The respiratory signal that corresponds to each bed position is normalised such that the mean value is 0, and the range is $[-1, 1]$. An overall respiratory curve $r(t)$ is created by sequentially combining $\hat{\rho}(t)$ from each bed position. Outliers are removed by applying a 95% histogram threshold, and amplitude based binning is performed on the original cine CT images as described in section 2.2.1.2.

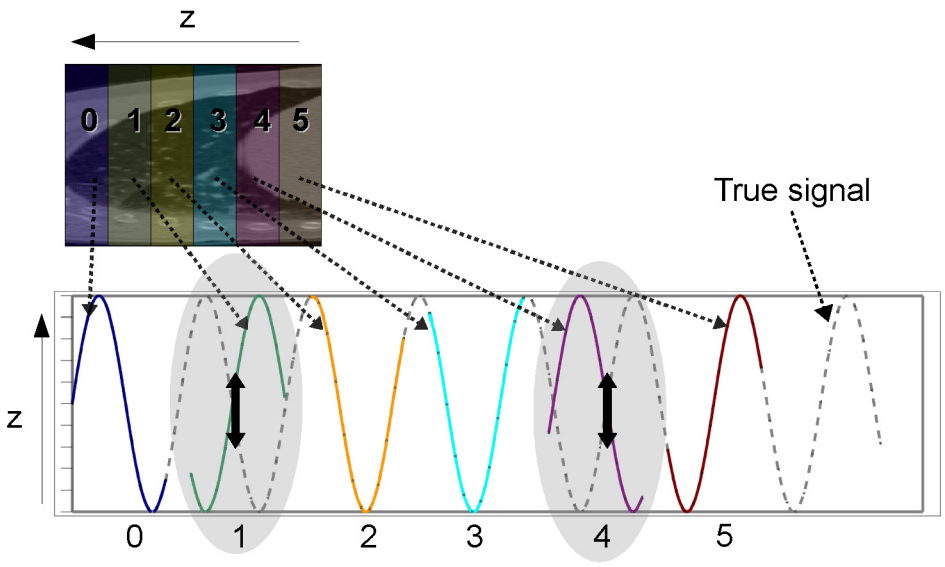

Figure 2.3: Sagittal CT showing 6 bed steps and the respiratory curve segment, $\hat{\rho}$, produced from each step. Curve segments and the true curve are shown as a sinusoid for clarity. As $\hat{\rho}$ is related indirectly to displacement, an increase in $\hat{\rho}_0$, $\hat{\rho}_2$ $\hat{\rho}_3$ and $\hat{\rho}_5$ infers motion in the $+z$ direction, however an increase in $\hat{\rho}_1$ and $\hat{\rho}_4$ infer motion in the $-z$ direction, indicating that these two segments are flipped.

Where multiple images are assigned to a single image bin, only the final image written to the bin is recorded. When data is not available for a time point of a given bin, the image data from the nearest bin is duplicated.

2.2.3 Phantom acquisition

Prior to evaluating the gating technique on patients, a simple mechanical 4D phantom was used to test the data acquisition and gating procedures. A 6 L cylindrical perspex phantom with 6 spherical, fillable inserts was attached to a stepper motor which was programmed to periodically drive the phantom in and out of the scanner in the axial direction. A semi-sinusoidal pattern of motion was used, such that a higher velocity and acceleration was used to drive the phantom into the scanner, and the reverse movement was performed with reduced velocity and acceleration. A real-time position management (RPM) gating system (Varian Medical Systems, Palo Alto, CA) hardware based respiratory gating system was used to acquire hardware derived signal for comparison with the signal derived from the data-driven gating method. Images were acquired on a GE Discovery ST (General Electric Medical Systems, Waukesha, WI) BGO, 4 slice PET/CT scanner.

The spheres were filled with approximately 25 kBq/ml, and the 6L background with approximately 5 kBq/ml. A 16 cm cine CT and a 5 min 2D PET were acquired as described in section 2.2.4.

2.2.4 Patient Acquisition

Ethics approval was granted by the national research ethics process. Four patients with lung lesions known or suspected to be cancer consented to take part in this study. All images were acquired on the GE Discovery ST also used for phantom acquisitions.

CT images were acquired over a 16 cm axial field of view to approximately match the PET scan over a known lesion in the patient's chest. The collimator was set to 4×2.5 mm, such that sixteen 1 cm bed positions were acquired, with a rotation speed of 0.5 sec, and a cine duration of 5.5 sec, producing 12 reconstructed images per z-location. 5.5 seconds was used as the cine duration

to provide a high likelihood of obtaining at least half of a respiratory cycle (from inspiration to expiration or vice versa) while maintaining a relatively low patient dose. A tube voltage of 140 kVp and current of 20 mA was used. Images were reconstructed to a 512×512 matrix, and a total of 64 z-slices were acquired. The approximate radiation dose to the patient from the cine CT was 5 mSv.

One PET bed position was acquired over a 15.4 cm axial field of view, in 2D, for 5 min, and in listmode. Sinogram data was analysed using a temporal period of 100 msec.

Each PET sinogram frame was attenuation corrected using the corresponding CT frame [66]. PET sinogram frames were reconstructed using OSEM with 15 subsets, and 2 iterations, using the ASPIRE library [43].

Respiratory signals recorded with the RPM device were compared with the respiratory signals extracted using the described data-driven methods. Signals were z-score normalised prior to comparison:

$$r_n(t) = \frac{r_s(t) - \mu}{\sigma} \tag{2.22}$$

where μ and σ are the respective mean and standard deviation of the signal $r_s(t)$, and $r_n(t)$ is the normalised signal. To produce a measure of similarity between the two signals, a percentage error between the z-score normalised rpm (r_{rpm}) and data-driven (r_{ddg}) signals was calculated as the normalised RMS error (nRMSE),

$$nRMSE = \frac{\sqrt{\frac{\Sigma(r_{rpm} - r_{ddg})^2}{n}}}{r_{max} - r_{min}} \tag{2.23}$$

where n is the number of points in the respiratory signal, and r_{max} and r_{min} define the maximum and minimum of the respiratory signals.

2.2.5 Parameter selection

A common set of the PET and CT gating parameters described above were initially chosen experimentally such that accurate results were produced for all patients. PET analysis was performed using a temporal sampling of $T = 100$ msec. To avoid de-sensitising the mask to regions affected by both cardiac and res-

piratory motion, the reference window defined by index υ_3 was set to 1.67 Hz, corresponding to a heart-rate of 100 bpm. A θ step of 7 was implemented to minimise computational demand such that only every 7th projection angle analysed after the low pass filter had been applied. The spectral window υ_1, υ_2 was defined as $f_1 = 0.125$ Hz (8 second period), $f_2 = 0.375$ Hz (2.7 second period).

CT thresholds of $K_{min} = -624$ (HU) and $K_{max} = -424$ (HU) were chosen by manually adjusting the values until the lung structure was retained. The sampling period of the CT data was 450 msec resulting in a Nyquist frequency of 1.1 Hz and a frequency resolution of 0.185 Hz in the Fourier spectrum, given that 12 images were produced per z-location. The spectral window limits were set to $\upsilon_1 = 1$ and $\upsilon_2 = 2$, corresponding to 0.185 Hz (5.4 second period) and 0.37 Hz (2.7 second period) respectively and a reference index of $\upsilon_3 = 4$ corresponding to 0.74 Hz (1.35 second period) was used. Given the low frequency resolution of the spectral data, the restrictive window was reduced such that only one index location was used in the restricted binary mask A, i.e. $\delta = 0$.

To investigate the sensitivity of the gating system to the parameters which characterise the spatial filter, restrictive window, and mask activation percentage, signal extraction was performed with different sets of parameters with widely varying values. The values assigned to these parameters are listed in table 2.1.

2.3 Results

2.3.1 Phantom study

The phase weighted mask, shown in figure 2.4, accurately located the edge of the phantom that was normal to the direction of motion, and the correctly weighted the leading and trailing edges of the spheres.

The respiratory curves obtained with the data-driven and RPM methods were closely matched (figure 2.5), with 8% difference between the curves. Visually, no difference between the PET images gated with the two methods could be seen.

PET and CT data were successfully gated, and each PET sinogram bin was attenuation corrected with corresponding CT bin. Figure 2.6 contains bins 0 and 6 of the CT image set, demonstrating the displacement of the spheres. Maximum

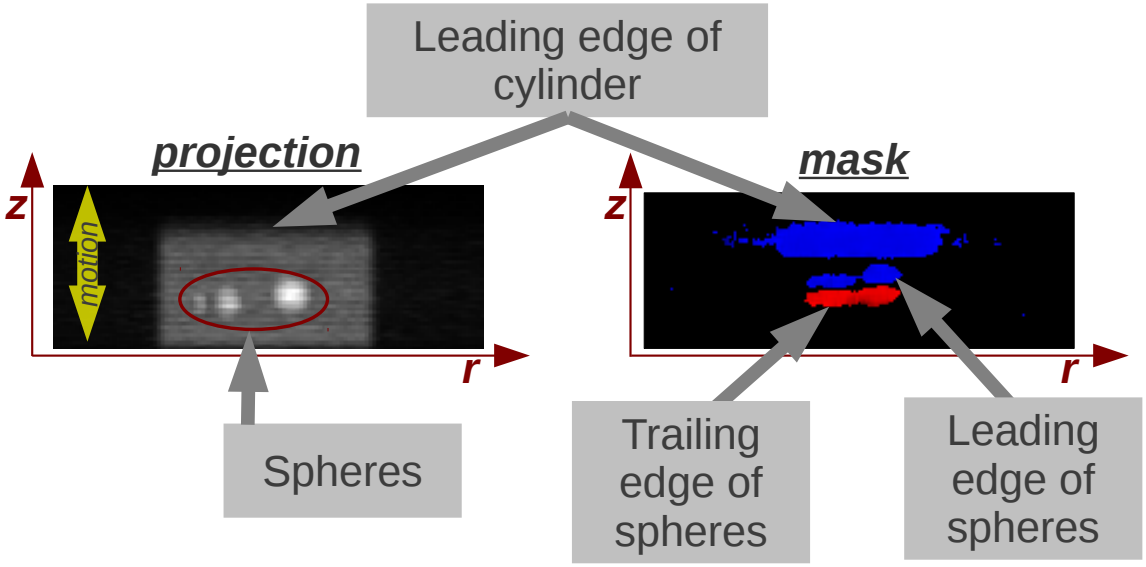

Figure 2.4: The first projection angle of the PET phase weighted mask generated from the phantom experiment. The edge of the phantom normal to the direction of motion was accurately located, and the leading and trailing edges of the spheres are correctly weighted as positive (blue) and negative (red) respectively.

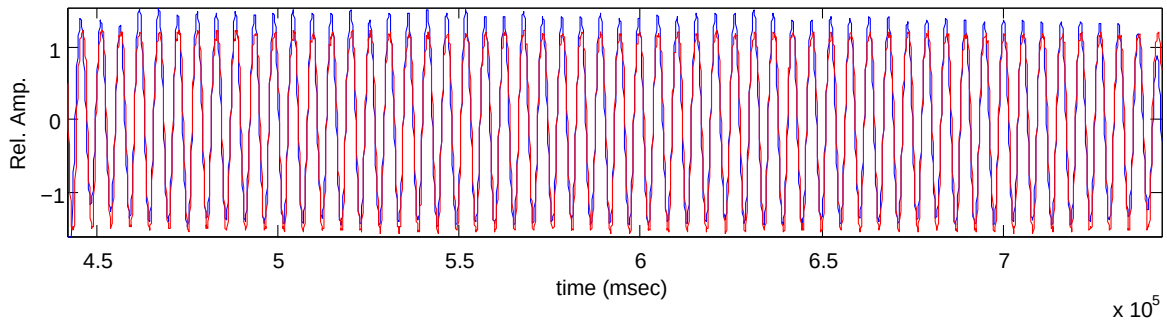

Figure 2.5: Data-driven (blue) and RPM based (red) respiratory curves for PET component of phantom acquisition.

	H_r	H_z	H_θ	H_t	H_x	H_y	δ	$\%_{mask}$	N_{bins}
A_{PET}	13	13	35	5	-	-	0.1 Hz	10%	8
B_{PET}	11	11	30	5	-	-	0.1 Hz	10%	8
C_{PET}	17	17	50	5	-	-	0.1 Hz	10%	8
D_{PET}	13	13	35	5	-	-	0.1 Hz	0.2 %	8
E_{PET}	13	13	35	5	-	-	0.1 Hz	2%	8
F_{PET}	13	13	35	5	-	-	0.02 Hz	10%	8
G_{PET}	13	13	35	5	-	-	0.2 Hz	10%	8
A_{CT}	-	-	-	-	7	7	0	5%	8
B_{CT}	-	-	-	-	7	7	0	0.1%	8
C_{CT}	-	-	-	-	7	7	0	10%	8
D_{CT}	-	-	-	-	4	4	0	5%	8
E_{CT}	-	-	-	-	14	14	0	5%	8

Table 2.1: PET and CT parameter groups used for signal extraction. Filter parameters H define the kernel size. $H_{r,z,t}$ and $H_{x,y}$ have equal Gaussian full-width-half-maximum (FWHM), and H_θ has an infinite FWHM effecting an average filter.

intensity projections (MIPs) of attenuation corrected PET bins 0 and 6 are shown in figure 2.7 along side the non-gated PET, highlighting the displacement between bin 0 and 6. While the non-gated image contains less noise than each bin, the gated images contain less motion artefact. This is particularly notable on the smallest sphere.

2.3.2 Patient studies

Results shown are those generated with parameter set A unless otherwise stated.

The respiratory frequency f_{resp}, calculated for each patient from the PET and CT data sets is shown in table 2.2. Visual inspection of the gated PET and CT images demonstrated that the gating was successful on all four patients. Respiratory motion was evident and monotonic from first to last bin at the site of disease. The direction of motion from bin 1 to 8 appeared consistent across all 16 CT bed positions for all patients. Coronal and sagittal fused PET and CT images for patient 1 and 3 are shown in figures 2.8 and 2.9 respectively. Bins 1 and 2 for patient 1, and bin 1 for patient 3 are not shown as they recorded low

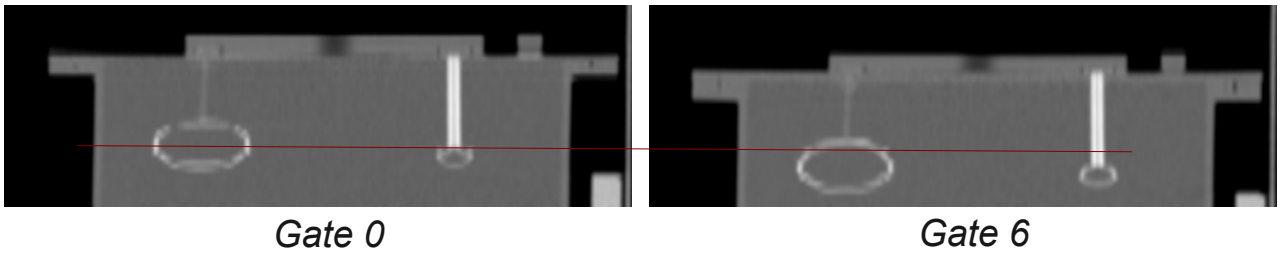

Figure 2.6: Bins 0 and 6 of the gated CT for the phantom image. Red line shown for spatial reference.

Pat.	CT	PET
1	2.7 sec (0.37 Hz)	2.9 sec (0.34 Hz)
2	5.3 sec (0.19 Hz)	7.7 sec (0.13 Hz)
3	2.7 sec (0.37 Hz)	4.2 sec (0.24 Hz)
4	5.3 sec (0.19 Hz)	8.3 sec (0.12 Hz)

Table 2.2: Calculated respiratory frequency f_{resp}, CT and PET.

PET counts.

The z-score normalised RPM recorded signal was overlaid with the normalised data-driven signal for the PET (figure 2.10) and CT (figure 2.11) components of the study. These figures visually demonstrate a strong correlation between the two signals in both PET and CT signals, for all four patients. The normalised RMS error between the RPM signal and data-driven signal ranged from 13.5% to 18.0% for the CT series, and 5.9% to 10.5% for the PET series, as shown in table 2.3.

To determine the amount of displacement between each of the gated bins, a volume of interest was defined over the tumour on the gated images and the centre of mass projected onto the z-axis (zCOM) calculated for each bin. The range of displacement over the bins provides an indication of the amount of motion of the tumour that is resolved by the technique. Non-attenuation corrected PET images

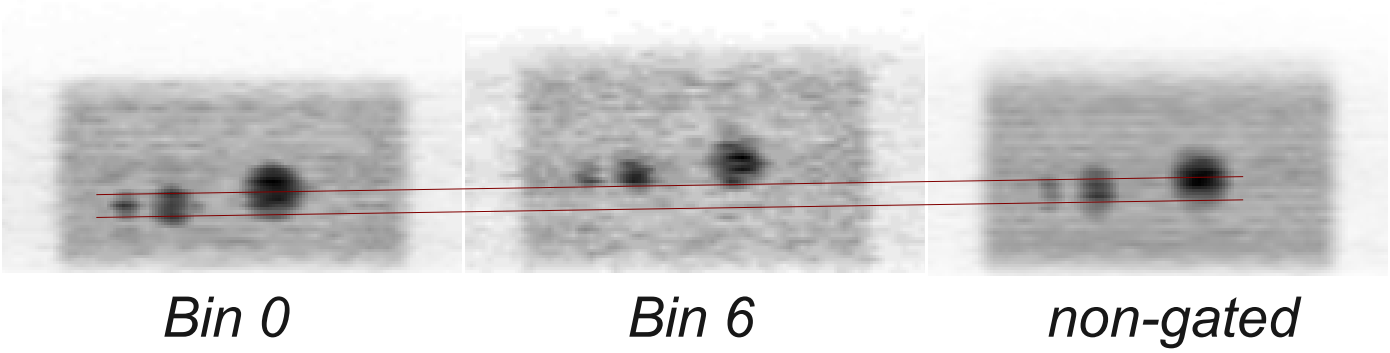

Figure 2.7: Attenuation corrected PET MIPs for bins 0 and 6 of the gated phantom acquisition. Gated images contain less motion blur, but more noise than the non-gated image. Red lines shown for spatial reference.

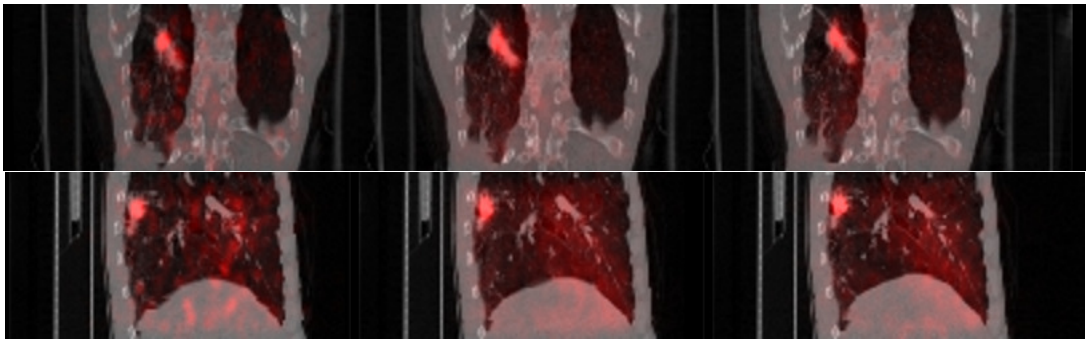

Figure 2.8: Patient 1. Coronal (top) and sagittal (bottom) fused PET and CT images, bins 3, 5, 8 (left to right).

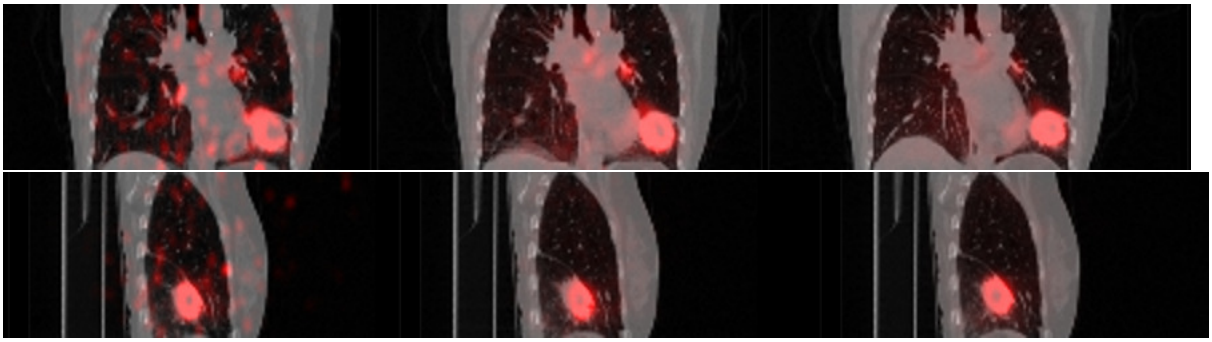

Figure 2.9: Patient 3. Coronal (top) and sagittal (bottom) fused PET and CT images, bins 2, 5, 8 (left to right).

Pat.	CT	PET
1	16.6 %	10.5 %
2	13.5 %	5.9 %
3	18.0 %	10.0 %
4	13.5 %	7.3 %

Table 2.3: Normalised RMS error between RPM and data-driven signals, CT and PET.

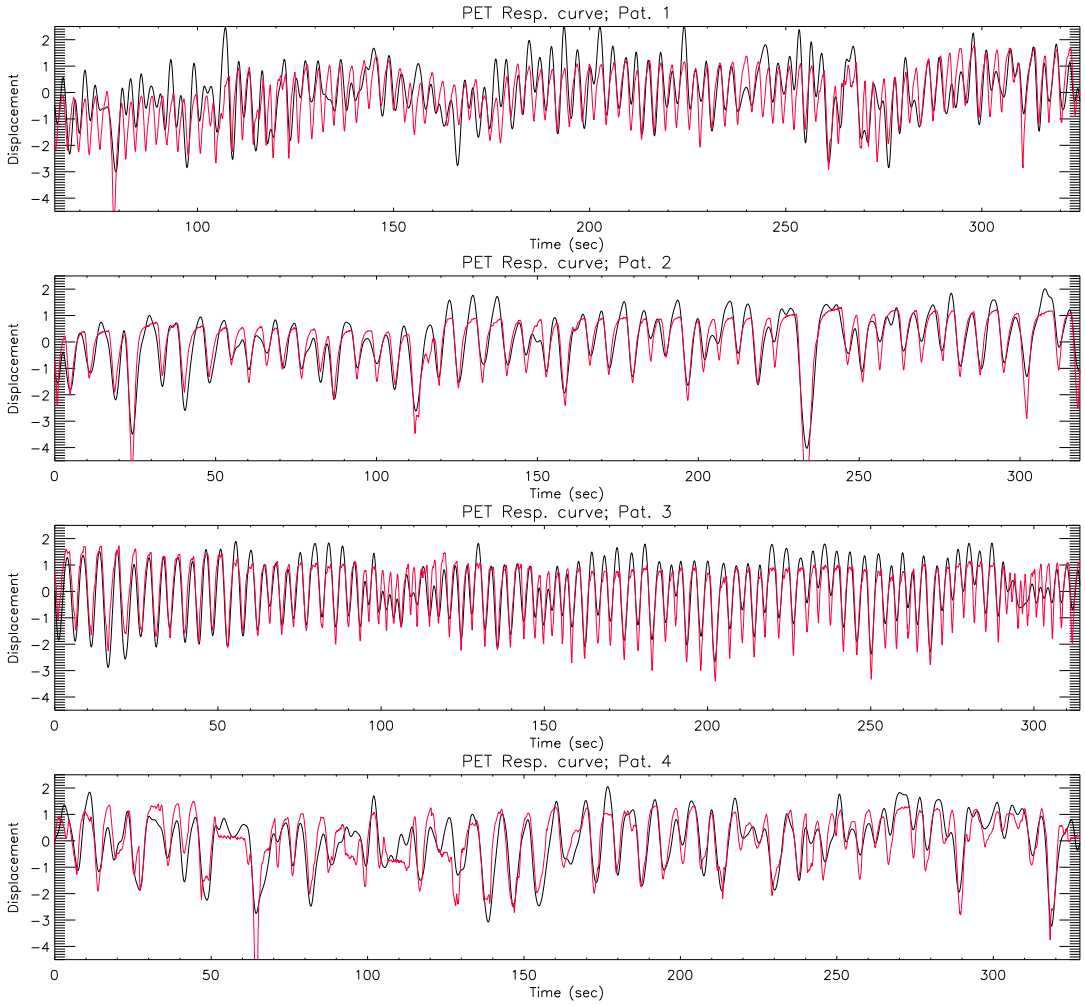

Figure 2.10: PET normalised RPM curve (red) overlaid with normalised data-driven curve (black).

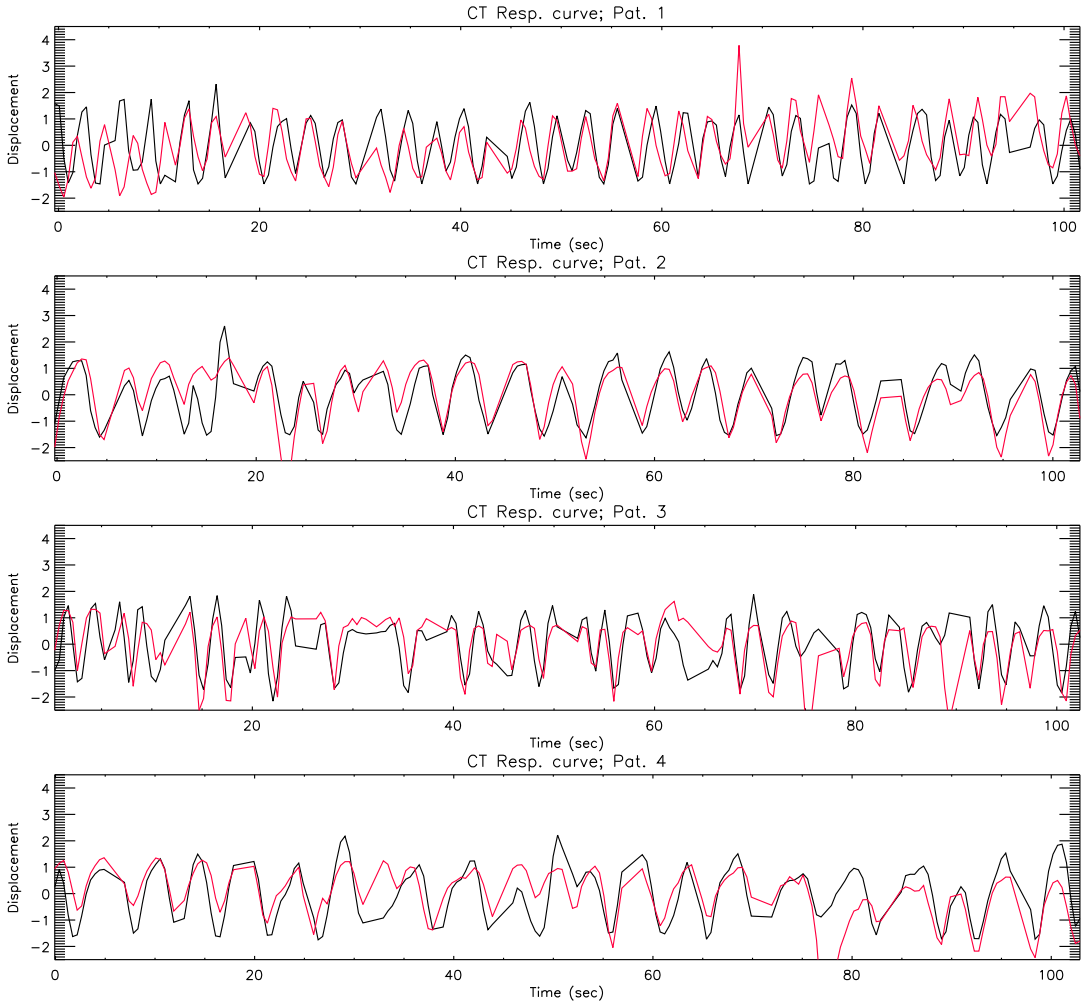

Figure 2.11: CT normalised RPM curve (red) overlaid with normalised data-driven curve (black).

were used to avoid influence of the CT binning process. The zCOM measurements calculated from PET images are shown in figure 2.12 for both data-driven gated images and RPM gated images. Bins containing less than 1% of the counts in the bin with the greatest counts were excluded. Accordingly the range of motion measured on the data-driven images was 3.1, 8.3, 5.0 and 6.5 mm, and on the RPM gated images 4.2, 7.7, 4.4 and 5.1 mm for patients 1, 2, 3 and 4 respectively.

Figure 2.13 shows the zCOM measurements calculated from the RPM gated and data-driven gated CT images. The measured range of motion on the data-driven gated images was 5.1, 5.8, 2.6 and 6.3 mm, and on the RPM gated images 4.4, 5.3, 2.2 and 5.8 mm for patients 1, 2, 3 and 4 respectively.

ZCOM range and nRMSE values for PET and CT created with the different parameter sets are shown in figures 2.14 and 2.15 respectively. For patient 1, parameter set C resulted in a 56.7% drop in the PET zCOM range when compared with the mean range for all parameter sets for patient 1. All other patients were less than 12.5% below the mean PET zCOM range for each patient. CT zCOM values were within 9% of the mean CT zCOM value for each patient. Comparison of the RPM curves with the data-driven curves revealed similar results. Patient 1, C demonstrated a nRMSE of 16.6%, 4.9% greater than the mean value of 11.7% for patient 1. All other values were within 1% of the mean nRMSE value for PET. All nRMSE values were within 4% when comparing the two curves for the CT data.

Figure 2.16 shows the RPM gated and data-driven gated CT images for bin 5 of patient 1, and bin 6 of patient 3. RPM gated CT images for these patients demonstrated a high level of motion artefact which was not evident in the data-driven gated CT images. Data-driven gated CT images and RPM gated CT images for patients 2 and 4 both contained comparably low levels of motion artefact.

2.4 Discussion

The respiratory frequency calculated from the CT data was consistently higher than the frequency calculated from the PET data, however, the largest difference between the CT and PET values was 0.13 Hz. This is less than the frequency

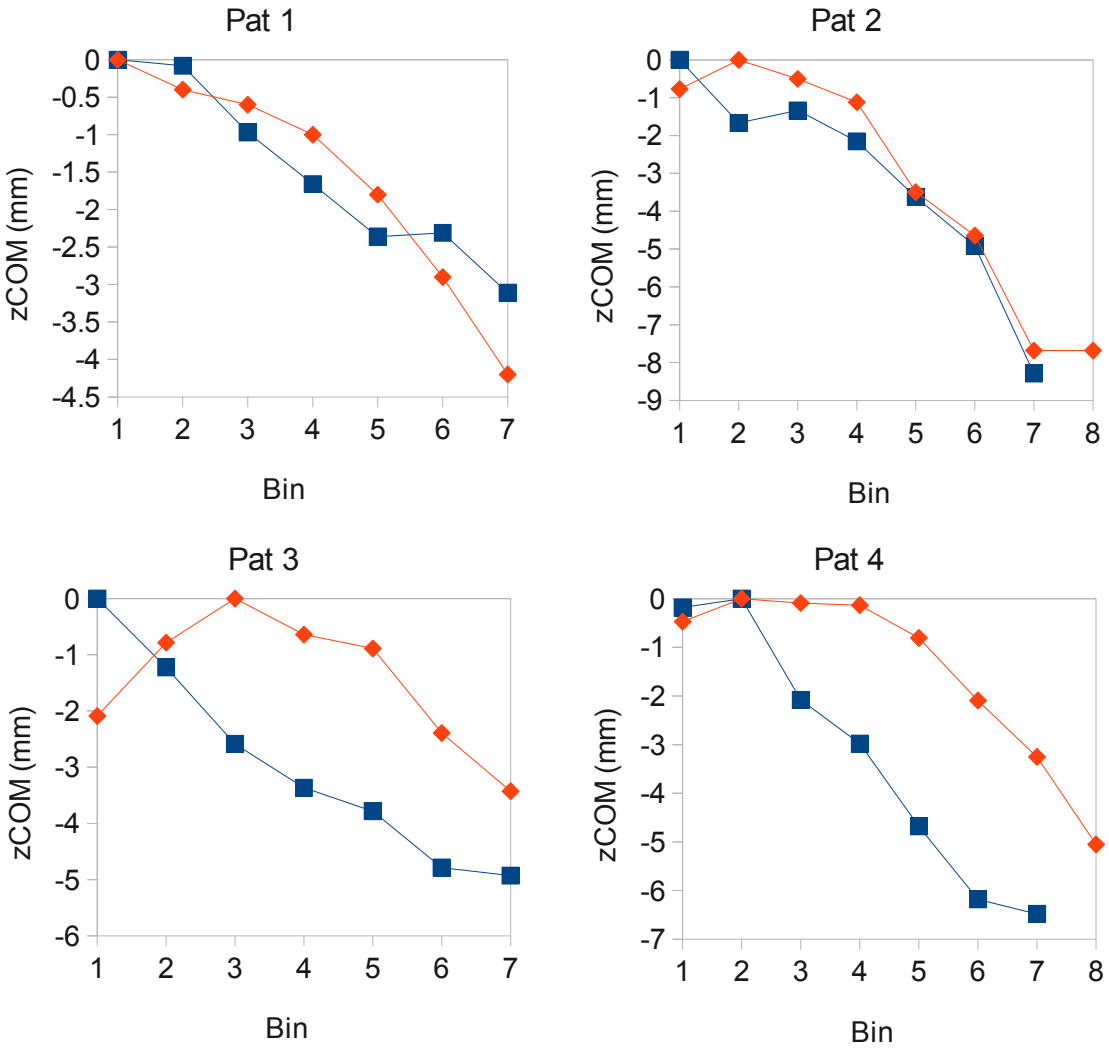

Figure 2.12: Centre of mass of the counts within a volume of interest defined over the tumour on non-attenuation corrected PET images. The COM along the z axis is shown, for images gated with the RPM signal (diamond) and the data-driven signal (square).

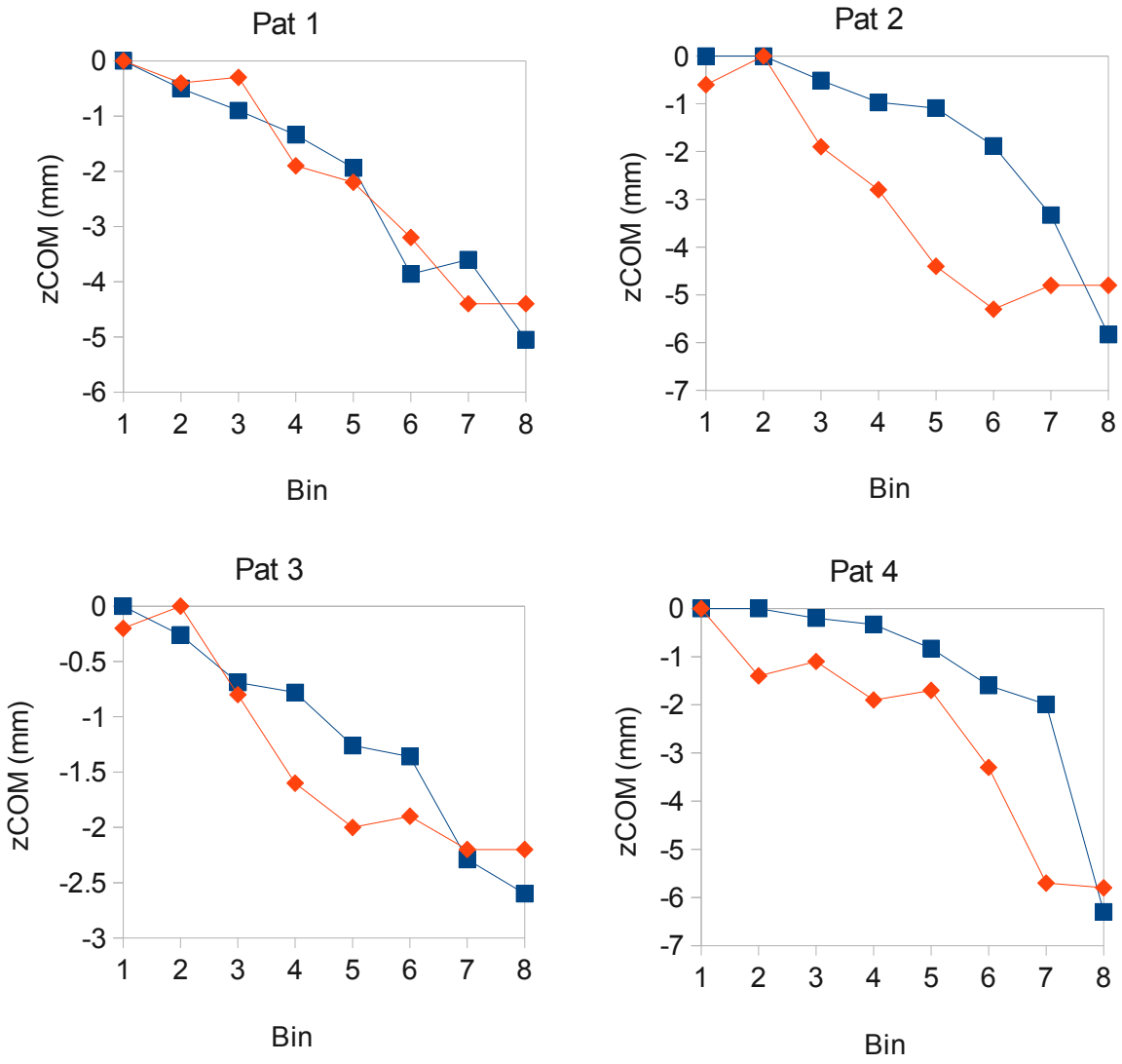

Figure 2.13: Centre of mass of a volume of interest defined over the tumour CT images gated with the RPM trace (diamond) and the data-driven signal (square). The COM along the z axis is shown.

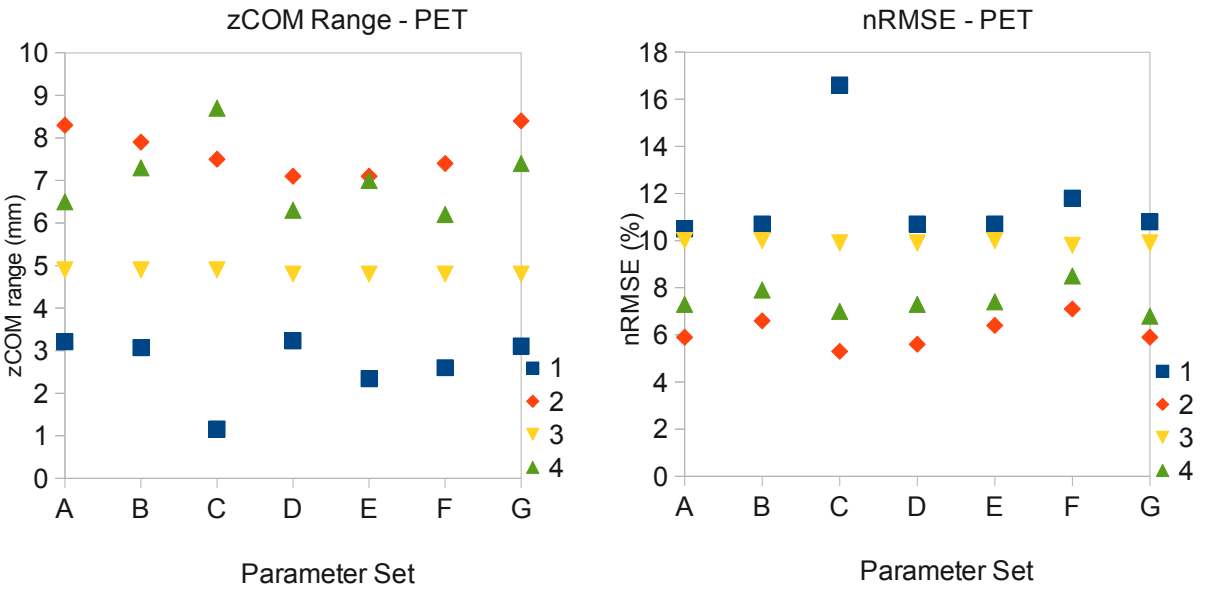

Figure 2.14: PET zCOM range (left) and nRMSE values (right) calculated from images created with parameter variations

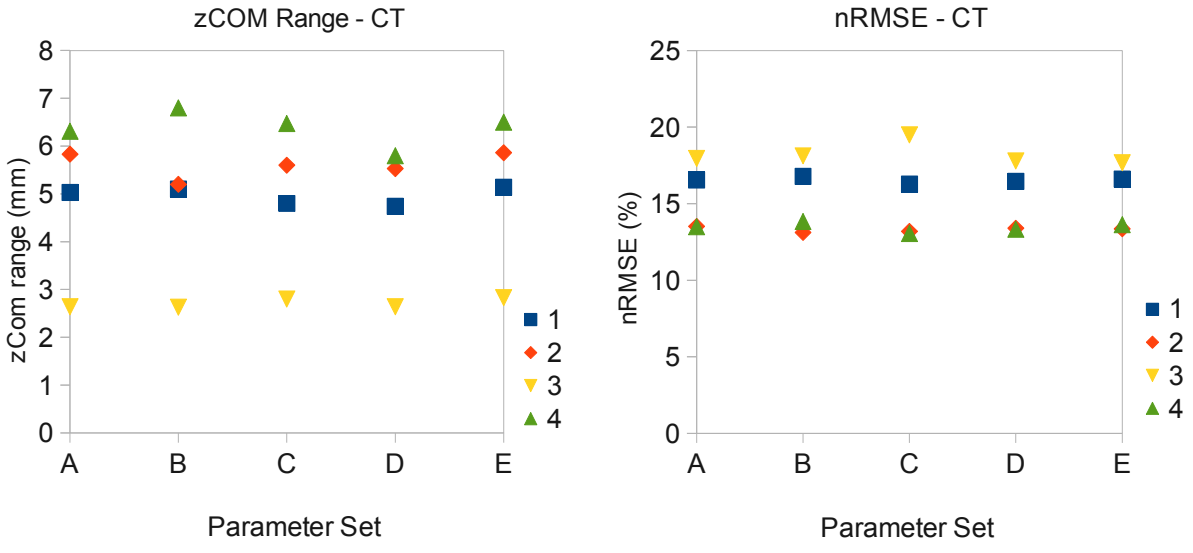

Figure 2.15: CT zCOM range (left) and nRMSE values (right) calculated from images created with parameter variations

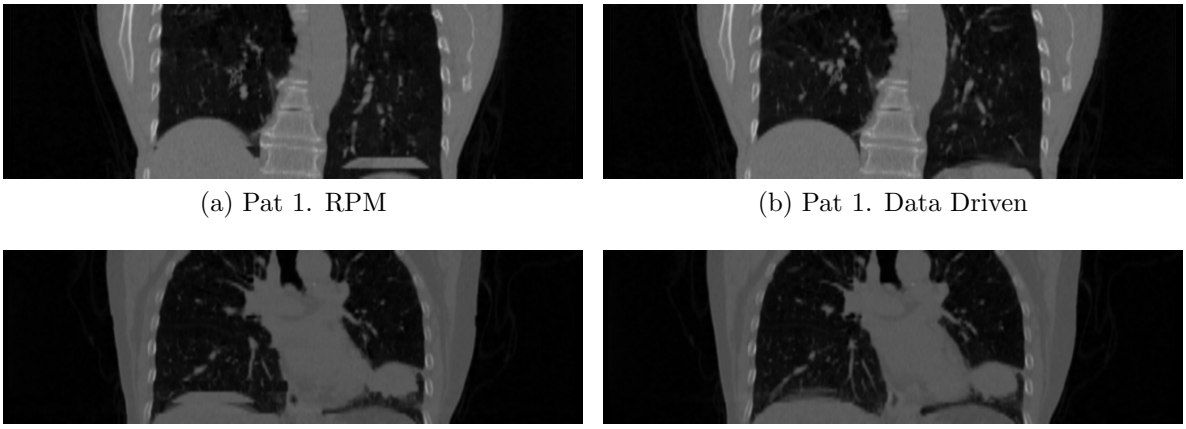

(a) Pat 1. RPM (b) Pat 1. Data Driven

(c) Pat 3. RPM (d) Pat 3. Data Driven

Figure 2.16: Coronal CT images for patients 1 bin 5 and patient 3 bin 6, RPM derived image demonstrating respiratory motion artefact, particularly at the diaphragm; data-driven image demonstrates reduced artefact.

resolution of the CT data following FFT, 0.18 Hz, indicating that similar f_{resp} values are obtained for the two modalities.

Visual assessment of the overlaid normalised traces demonstrate a generally accurate recovery of the RPM trace. Unusually high peaks in the CT curve appear not to be reproduced by the RPM system, however as the outliers are removed from the sequence prior to binning, these points do not affect the images.

Comparing the measured nRMSE of the two curves for all patients demonstrates a considerably higher difference for the CT component of the study. A likely explanation for this is the difference in sampling period for the two imaging components. A sample interval of 100 msec was used for the PET data, however images were reconstructed to 450 msec sample interval for the CT component.

Given that the RPM and data-driven signals are derived from measurements of different patient parameters, a certain amount of discrepancy is expected when the two signals are directly compared. An exact replication of the RPM signal would not be expected, nor would it necessarily indicate an ideal system. The measured difference between the two signals can only be referred to as an indication of the successful functioning of the data-driven system. This is supported by the images for patient 1 which recorded PET and CT nRMSE of 10.5 % and

16.6 % respectively, and patient 3 which recorded a PET and CT nRMSE of 10.0 % and 18.0 % respectively. Visual inspection of PET and CT gated images, and assessment of the zCOM measurements for these patients both indicate accurate binning.

Furthermore, when the RPM system is used to gate an acquisition of a lung tumour, the position of the abdominal or chest wall is being used as in index of the complex 3 dimensional position of the lung tumour. This is not necessarily an accurate assumption. Two of the four CT data sets actually demonstrated reduced respiratory artefact in the data-driven gated images, suggesting that in some cases the data derived signal is the more accurate, as also suggested by Zeng et al [150].

The centre of mass measurements indicate that both gating methods recovered a similar amount of tumour excursion for both PET and CT when using parameter set *A*. The range of the zCOM measurements was within 0.7 mm when comparing the CT images gated with the two methods, with the data-driven method consistently producing a marginally higher range. The data-driven gated PET images only produced a smaller range than the RPM gated images in patient 1 and recovered a higher range in all other patients, with patient 4 demonstrating an increase of 1.4 mm.

Increasing the spatial filter size (parameter set *C*) for patient 1 decreased the zCOM range by 56.7% and increased the nRMSE by 4.9% when compared with the mean values for patient 1. For all other patients and parameter variations accurate results were demonstrated. This suggests that, apart from very heavy spatial filters, the gating system is insensitive to large variations in the spatial filter, spectral window, and mask characteristics, and that the values used in this work are likely to be applicable to other datasets.

It is possible however, that the parameters used for these 4 patients may not be optimal for all patient datasets or PET/CT systems. Furthermore, some patients may exhibit respiratory characteristics which might lead the system to fail entirely, for example if the respiratory frequency varied considerably throughout the study. A further study with a larger number of patients will be required to clarify these outstanding issues.

A distinct advantage to performing respiratory gated studies using data-driven

methods over hardware based methods is the removal of the required hardware which requires time for imaging staff to configure for each patient. The methods proposed in this chapter describe a system which requires no user interaction prior to imaging; a clinical cine CT and listmode PET acquisition is acquired.

Several previously described PET data-driven methods require PET data to be reconstructed to short time frames prior to gating, requiring a considerable number of PET frames to be reconstructed. For example a 5 minute acquisition sampled at $100msec$ would require 3000 reconstructed volumes, or on a 47 slice PET camera, 141×10^3 reconstructed images. The method described in this work derives the respiratory signal from the aquired data in sinogram space, completely removing this overhead. Furthermore because listmode data consists of a record of sequential individual lines of response, this method can directly sample the listmode file to create temporary projection sequences in memory. In the absence of the ability to acquire listmode PET data, a dynamic series of sinograms would suffice provided short enough time frames were permissible.

While application of the PET gating system requires no alteration to the standard clinical imaging protocol, the CT gating system requires a cine CT acquisition over the region which is to be gated. Using the parameters described, and scanning over one PET bed position, the approximate effective dose for the cine CT component of this study is 5 mSv. The typical PET/CT protocol implemented for oncology patients at this centre results in a total patient dose of approximately 19 mSv. Performing the additional cine CT required for this gated study increases the total effective dose to approximately 24 mSv. Altering the parameters used to acquire the cine CT by decreasing the tube current and voltage and increasing the rotation speed provides the potential to reduce this dose, warranting further investigation.

Amplitude binning was used in this work, where each of the bins were of equal amplitude size. This typically results in a non-uniform distribution of counts across the bins and as such some gates were excluded. Using amplitude bins of variable size could overcome this issue, and may provide improved results [34].

The method was demonstrated with PET data acquired in 2D mode, and CT images acquired on a 4-slice system. All PET/CT systems currently in production are only capable of 3D mode, and also, are often capable of acquiring at least

64 CT slices simultaneously. Furthermore, clinical FDG images are typically acquired as multiple bed positions. Extending and validating the gating method to 3D, multi-bed position PET acquisitions is an important step in producing a gating method which is applicable in the clinical environment, and this forms the subject of chapter 3.

2.5 Conclusion

While hardware based respiratory gating techniques remain a widely accepted means of acquiring respiratory gated PET and CT data, data-driven techniques offer several advantages. In this chapter, an automated, retrospective, data-driven gating method for both PET and CT was developed. The method uses spectral analysis to find regions within PET sinograms and CT images which are subject to respiratory motion. To demonstrate the technique, gating was performed on listmode 2D PET and cine CT data acquired from four patients with lung tumours on a GE Discovery ST 4 slice PET/CT system. Based on quantitative and visual assessment of the gated images and direct comparison of the data-driven acquired respiratory curve with a hardware acquired respiratory curve, the system was found to perform accurately for all four patients.

Chapter 3

Respiratory gating clinical 3D whole body PET images.

3.1 Introduction

In the previous chapter, a data-driven respiratory gating method was described and demonstrated with 2D, single bed position PET and CT lung images of lung cancer patients. The technique uses a spectral analysis approach to form a mask that identifies pixels which are subject to respiratory motion. In PET, the mask is applied to a dynamic sinogram which is created from the listmode file. A counts vs. time curve is then produced by summing the pixel values in the masked region of the dynamic sinogram at every time point. As the mask includes pixels which lie at the edges of moving areas of activity, the total counts in the mask will vary with respiratory motion. Assuming the change in counts within the mask is proportional to the amplitude of displacement, the counts vs. time series provides an estimate the respiratory signal.

Given that typical PET imaging protocols involve acquiring multiple bed-positions and respiratory motion is known to affect organs other than the lungs [61], including the prostate [86], it is desirable to produce a respiratory gating method that is applicable to multiple bed positions covering all parts of the body that are subject to motion. Additionally, gating all acquired bed positions removes user interaction required to select and gate individual bed positions.

Also, at this time all commercially available PET scanners are not capable of imaging in 2D mode, therefore this system should be capable of gating 3D PET data.

No system currently exists which can perform data-driven respiratory gating on 3D, multi bed-position PET images. In the previous chapter the gating method was only applied to single bed position, 2D PET images of the lung. In this chapter, the data-driven gating method is modified to enable gating of 3D data, data acquired from the lung bed position is used to guide the gating procedure for the remaining bed positions, and a method based on registration is developed to align the direction of motion between bed positions. These developments were essential to enable 3D whole body data-driven gating by this technique.

The modified gating method was evaluated with clinical patient data. For comparison, the RPM hardware based respiratory monitoring system was used to acquire the respiratory signal of the patients during the acquisitions. Raw PET data was then retrospectively gated using both the data-driven method and the optical signal. Non-attenuation corrected (NAC) gated images were quantitatively assessed to separate the effect of using a single, helical CT to attenuation correct a gated PET series. This allowed evaluation of the gating alone. Attenuation corrected (AC) images were also reconstructed to demonstrate the feasibility of producing gated, AC images for clinical use. All processing related to the gating was performed off-line, however for the assessment all gated data were restored to the PET-CT scanner console for reconstruction.

3.2 Methods

All images were acquired on a GE Discovery VCT (General Electric Medical Systems, Waukesha, WI) PET/CT system. Helical CT images were acquired at 140 kVp, 64 mAs, 0.4 second rotation speed, pitch 1.375, 16×2.5 mm collimation, and reconstructed to 3.75 mm thickness with a spacing of 3.27 mm. No breathing instructions were given, and no contrast agents were used. Following the CT, a half-body 3D PET was acquired from inferior to superior. Images were acquired using the standard clinical protocol used by the department, for 4 minutes per bed position, and with a bed overlap of 11 slices. The axial field of view (FOV) of the

Discovery VCT is 150.4 cm and the 3D sinogram dimensions are $329 \times 553 \times 280$ in the r, ϕ and θ dimensions respectively. All PET data were acquired in listmode.

Eleven lung or oesophageal cancer patients were injected with approximately 350 MBq of FDG, approximately 90 minutes before scanning commenced. Institutional permission was granted to perform this research study, and informed consent was obtained from all patients taking part. A Varian RPM system was used to acquire a hardware based respiratory signal on all patients. The imaging technologist placed the reflective marker for the RPM system where respiratory motion was observed to be greatest. The box was placed on the abdomen (between vertebrae L1 and L3) for 9 patients, and on the xiphoid process (between vertebrae T9 and T10) for 2 patients.

The data-driven gating method, described in chapter 2 is a two stage process. Firstly, a dynamic sinogram series of 100 msec frames is created from listmode PET data, and is spatially filtered. Using a spectral analysis, a mask is then created which identifies regions in projection space that are subject to motion. Secondly, a counts vs. time series is produced by summing the pixel values in the masked dynamic sinogram. This counts vs. time series is used to estimate the respiratory signal.

3.2.1 3D PET

To apply the gating method to 3D PET, only listmode events which crossed 5 crystal ring pairs (see section 1.1.2.3) or less were accepted, and single slice rebinning (SSRB) was used to create 2D data from indirect planes. This was done to reduced the lines of response to the same acceptance range used by the VCT in 2D mode, conditions under which the method had been previously evaluated. The reduced set of listmode events was only used to produce the respiratory signal estimate. Once this had been obtained, the entire listmode dataset was binned into the 3D sinogram gates for reconstruction.

3.2.2 Multi-bed PET

The gating method estimates the dominant frequency component of respiration in the lung position, f_{resp} (derived from equation 2.15), and uses this to restrict

the range of frequencies over which to evaluate each sinogram location in the raw data. In the previous chapter only PET images of lung tumours were used. It was expected that in multi-bed PET imaging, low amplitude of motion in some bed positions could reduce the sensitivity of the gating system. To overcome this, only one value of f_{resp}, calculated from the lung position, was used to centre the frequency window that is used to define the mask, for all bed positions.

For the lung position, a full analysis was performed in order to calculate f_{resp} (the frequency window was defined by $f_1 = 0.1Hz$ and $f_2 = 0.35Hz$, and the restrictive window set to $\delta = 0.1Hz$). As calculating f_{resp} for the remaining positions was not necessary, a narrow frequency window was used, centred on the lung f_{resp} value (the frequency window was defined by $f_1 = f_{resp} - 0.02Hz$, and $f_2 = f_{resp} + 0.02Hz$).

To automatically determine which PET bed position was of the chest, the corresponding helical CT data was used. CT data was thresholded to create an approximate mask representing the lungs; pixels between -400 Hounsfield Units (HU) and -900 HU were set to 1, and all others to 0. The mask volume was divided into sections which corresponded to the PET bed positions, and the section with the highest number of non-zero pixels was used as the chest bed position. If the two highest positions contained less than 20 % of the total non-zero pixels, then the most inferior position was selected as we expect the base of the lung to contain greater motion than the upper lung.

Following extraction of the respiratory signal estimate, in some cases, using f_{resp} as the cutoff to filter the signal produced an overly smoothed respiratory curve such that some peaks in the respiratory signal appeared to be eliminated or reduced in amplitude when compared with the hardware based signal. So in this section an arbitrarily cutoff of $2 \times f_{resp}$ was used to filter the signal prior to amplitude binning the listmode data. Reducing the attenuation of the respiratory signal between f_{resp} and $2 \times f_{resp}$ appeared to prevent the loss or amplitude reduction of respiratory peaks.

3.2.3 Combining PET bed positions

The gradient of the respiratory signal produced by the data-driven method is arbitrarily related to the direction of motion; it is not known if an increase in signal amplitude resulted from movement in the positive or negative direction. A simple, 1 dimensional registration between gates was used to determine the direction of inferior-superior motion from the first to last gate. This procedure consisted of a series of steps, which are summarised in figure 3.1. At each bed position, a series of 3D sinograms were produced by the gating method, which were then normalised for PMT gain differences and geometric sensitivity using the 3D normalisation method for the VCT scanner. Normalised sinograms were then single-slice-rebinned (SSRB), creating a series of 2D sinograms. These were corrected for cross-plane sensitivity, and reconstructed using filtered back projection (FBP).

From this gated, non attenuation corrected image series, a coronal maximum intensity projection (MIP) image was calculated for each gate. MIP images were used for registration rather than coronal slices to reduce noise. The gate which contained the longest acquisition time was used as the reference MIP image, m_{ref}. Each of the remaining MIP images, m_g, where g corresponds to the gate number, were approximately registered to m_{ref} in the z-direction only. A rigid body, 1-dimensional registration was used.

The registration between the MIP images was performed by defining centrally placed selection windows, m'_{ref} and m'_g over the reference and gate MIPs respectively, and moving m'_g over a range of z-locations across the gated image. The range used was -5 to +5 pixels (-16.4 mm to +16.4 mm), and the size of the selection windows was the full 128 pixels (600 mm) in the x direction, and 37 pixels (121 mm) in the z direction. The window over the reference image remained centrally placed, and static.

At each z-location, a difference image was calculated by subtracting the contents of the reference window and the gate window. Each difference image was filtered with a 3×3 pixel Gaussian filter with a 55 mm full width half maximum. The standard deviation of the smoothed difference image was then used to quantify the amount of mis-registration between the reference window m'_{ref}, and the

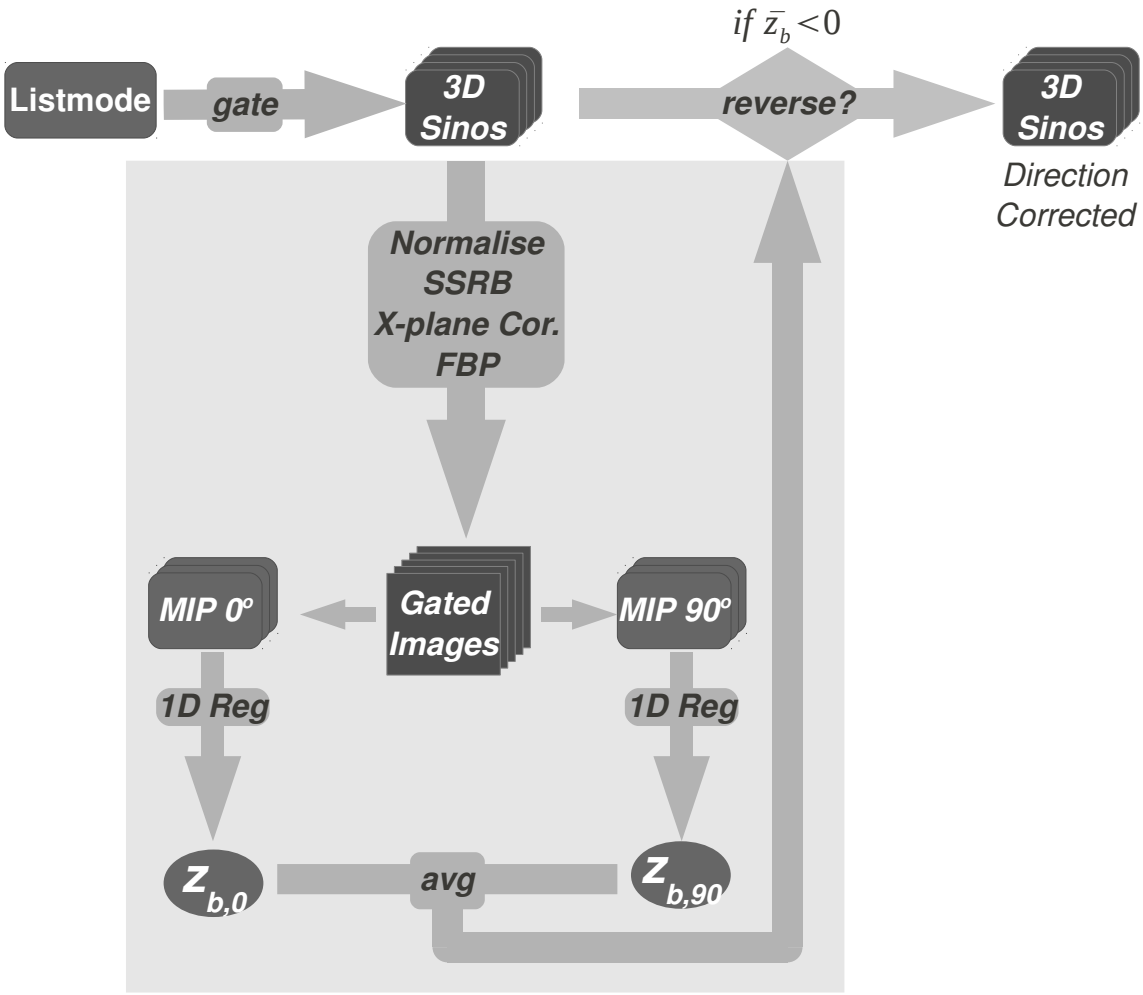

Figure 3.1: Flow chart describing the method to correct the direction of the gates in a given bed position. A simple, 1D registration is used to determine the z-direction of movement in the MIP images, which are produced from 2D (SSRB), normalised reconstructed images. If the direction is determined as negative, the gated series are reversed.

gate window $m'_{g,\Delta}$ shifted by Δ pixels in the z-direction.

The z-step that provided the minimum difference, z_{min} was selected as the point of registration, such that

$$z_{min,g} = argmin(sd\{(m'_{ref} - m'_{g,\Delta}) \star H\}) \qquad \Delta\epsilon[-5,5] \qquad (3.1)$$

where H defines the 2D Gaussian smoothing kernel, and sd defines the standard deviation operator.

If $z_{min} = 0$, i.e. no displacement, then z_{min} was set to the z-step that produced the second lowest difference.

The registration resulted in a point of registration, $z_{min,g}$, along the z-axis between the reference MIP and the MIP for gate g. This process was repeated for all gates, producing a $z_{min,g}$ for each gate, g. An acquisition-time weighted average of $z_{min,g}$ was then calculated,

$$z_b = \frac{\Sigma_{g=0}^{ngates} t_g z_{min,g}}{\Sigma t_g} \qquad (3.2)$$

where z_b is the weighted average of the displacement for bed position b, and t_g is the acquisition time of gate g.

The above method was then repeated with a sagital MIP, resulting in a second z_b measurement for each bed position. The direction of motion for bed b was then determined as

$$dir_b = sgn\{\frac{z_{b,coronal} + z_{b,sagital}}{2}\} \qquad (3.3)$$

If dir_b was found to be negative, then the gates for bed b were reversed.

Prior to registration, all MIP images were normalised to the maximum value, and values below 5% of the maximum were set to 0.

3.2.4 Reconstruction and Evaluation

Respiratory curves derived from the data-driven and RPM methods were compared by z-score normalising the curves according to equation 2.22. The normalised root mean squared (NRMS) error between the datasets was then calculated. This was performed for all bed positions, for all patients.

All gated 3D sinograms were restored to the VCT camera for reconstruction. The VUEpoint iterative reconstruction method was used, with 2 iterations and 20 subsets, and images were reconstructed to a 128×128 matrix over a 60 cm transaxial field of view. Non-attenuation corrected and attenuation corrected images were reconstructed, with the standard, non-gated helical CT used to attenuation correct all gates. Both RPM gated and data-driven gated data sets were reconstructed.

Volumes of interest (VOI) were manually defined on regions of focal tracer uptake which exhibited motion on the gated NAC dataset. The size and placement of these regions varied between patients because of different activity distributions. For each patient, 4 VOIs were defined and applied to all gates in both NAC gated datasets.

The 3 dimensional centre of mass was calculated in each VOI, for all datasets as

$$COM(g) = \sqrt{COM_x(g)^2 + COM_y(g)^2 + COM_z(g)^2} \tag{3.4}$$

where COM_X, COM_y and COM_z refer to the VOI centre of mass measurement for each gate g, in the x, y and z direction respectively. The overall displacement was defined as the change in COM between the first and last gates, i.e. $COM(8) - COM(1)$, indicating the amount of motion determined by respiratory gating using each of the respiratory signals. Overall displacement values were calculated for all VOIs and all patients on images created with the RPM and data-driven gated methods. A paired t-test was used to test the null hypothesis that the mean difference between the two groups of displacement measurements is 0. Rejection of the null hypothesis (at $p < 0.05$) would indicate that the displacement measured by the two methods differs significantly.

3.3 Results

A total of 75 bed positions were acquired, with a mean of 6.8 PET bed positions per patient (range 6 to 8), equating to a mean scan length of 839 mm (range 742 mm to 978 mm). The mean lungs bed position, identified from the helical CT, was 3.9 (range 3 to 5). Data-driven respiratory signals were obtained for all

bed positions, for all patients. The RPM system failed or partly failed in 5 bed positions, where the reflective box was obscured from the camera.

3.3.1 RPM comparison

Respiratory signals from the data-driven and RPM methods were compared visually and quantitatively. In the head and pelvis regions the lowest similarity was seen between the two signals, and the highest degree of similarity was seen in the lower lung and abdomen. This is exemplified in figure 3.2, which shows the amplitude normalised respiratory signal for all 6 bed positions for patient 11.

Bed positions 3, 4 and 5 produced an average NRMS error of under 23%. The error increased in the remainder of the bed positions, in accordance with visual comparison. Mean NRMS error values for all bed positions which contain full RPM data are shown in figure 3.3.

3.3.2 Combining bed positions

Of the 75 bed positions acquired, a negative z_b was calculated for 33 bed positions, and the gates for these positions were reversed. Reconstructed whole body gate sequences were assessed visually, and in all cases except 1, the correct bed positions appeared to have been reversed. For bed position 5 (upper lungs) of patient 11, the lung tumour appeared to move in the opposite direction to the liver. However, the visible level of motion in the tumour was barely detectable, and the overall COM displacement of the tumour was measured as 2.4 mm in the RPM gated series, and 1.1 mm in the data-driven gated series.

In 19 other cases, the NRMS error between the RPM and data-driven signals contradicted the reverse calculations, i.e. the NRMS error was lower when the data-driven signal was inverted if z_b was positive, or not inverted if z_b was negative. All of these positions except 1 were of the legs, pelvis, upper chest or head-neck regions, and in all of these cases no motion was visible in either the RPM or data-driven gated image datasets. In the exception case, the image was of the kidneys, and visual assessment of the gated images determined the registration method was correct. In this case, less than 1mm of overall kidney COM motion was measured in either dataset.

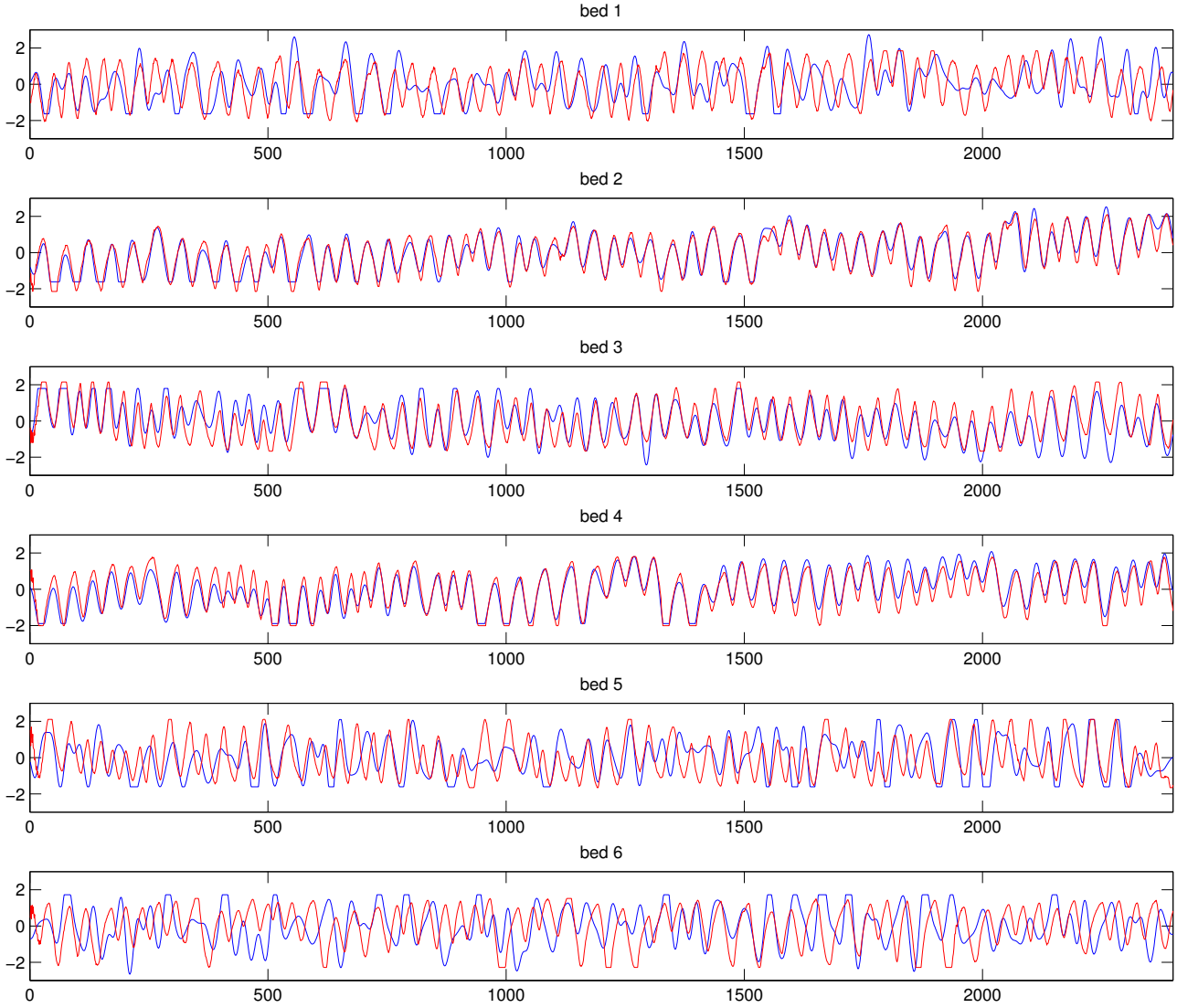

Figure 3.2: Amplitude normalised RPM (red) and data-driven (blue) respiratory curves for 6 bed positions, patient 11. Positions 1 and 6, acquired over the pelvis and head respectively. Clipped peaks exist where the amplitude exceeds the 95% outlier limit. RPM and DDG signals for bed positions 2, 3 and 4 appear to match closely, and bed positions 1 and 6 - where no motion was visible in either NAC image dataset, matched poorly. NRMS error values were calculated as 1: 27%, 2: 7%, 3: 17%, 4: 11%, 5: 29%, 6: 34%.

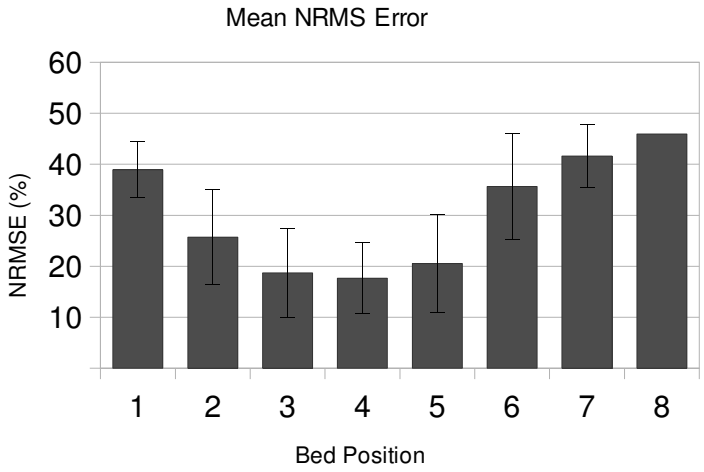

Figure 3.3: Mean NRMS error between data-driven and RPM curves for each bed position. The error bars indicate 1 standard deviation. Five bed positions which contained failed RPM data were removed. Less error is seen for central bed positions. All patients scanned from feet to head.

3.3.3 Image evaluation

In all cases, the non attenuation corrected and attenuation corrected gated images were successfully reconstructed on the VCT. Visually, the motion throughout the NAC and AC gated image series of the body appeared similar for both gating methods, for all patients. Figure 3.4 shows the non-gated and gates 1, 4 and 8 of the data-driven gated and RPM gated MIP AC images for patient 1. Motion is visible from the bowel to the mediastinum, and no motion is visible in the upper lung.

Volumes of interest were defined on all patients, and the relative change in COM calculated for both RPM gated and data-driven gated non-attenuation corrected image sets. The mean overall COM change (gate 1 to gate 8) for the data-driven gated images was 10.3 mm ($\pm 12.9mm$), and 9.1 mm ($\pm 11.4mm$) for the RPM gated images. Figure 3.5 shows a Bland-Altman plot comparing RPM and DDG derived measures of the overall COM change. A larger COM change was recorded in the RPM gated images in 17 measurements, and the data-driven gating images produced larger measurements in the remaining 27 cases. The mean overall displacement in all VOIs was 1.2 mm greater for the data-driven

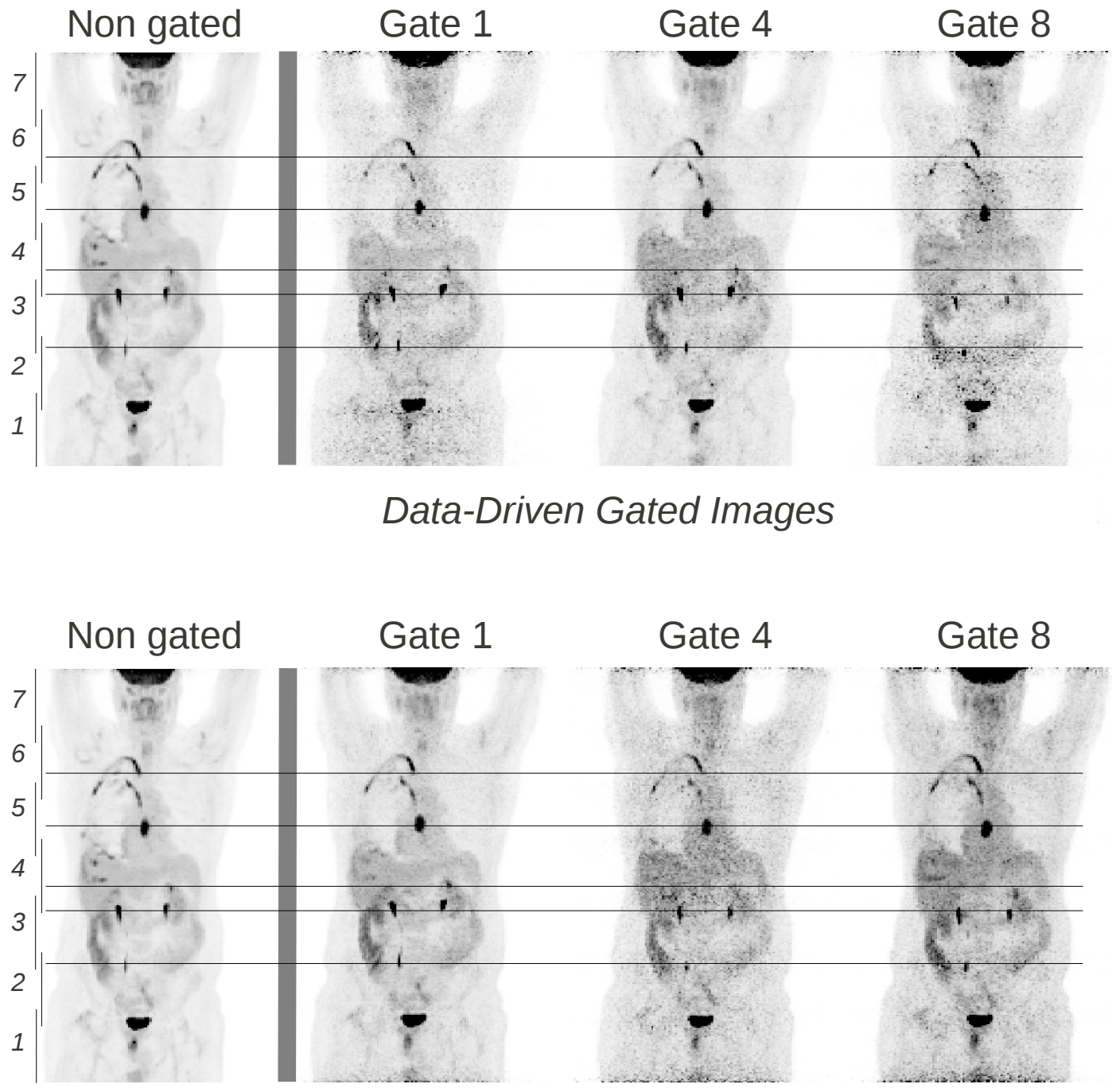

Figure 3.4: Data-driven gated (top row) and RPM gated (bottom row) attenuation corrected MIP images for patient 1. The non-gated image is shown on the far left, followed by gates 1, 4 and 8 from left to right. Horizontal lines which cross displaced structures are shown for reference. Bed positions are indicated by numbers on the left.

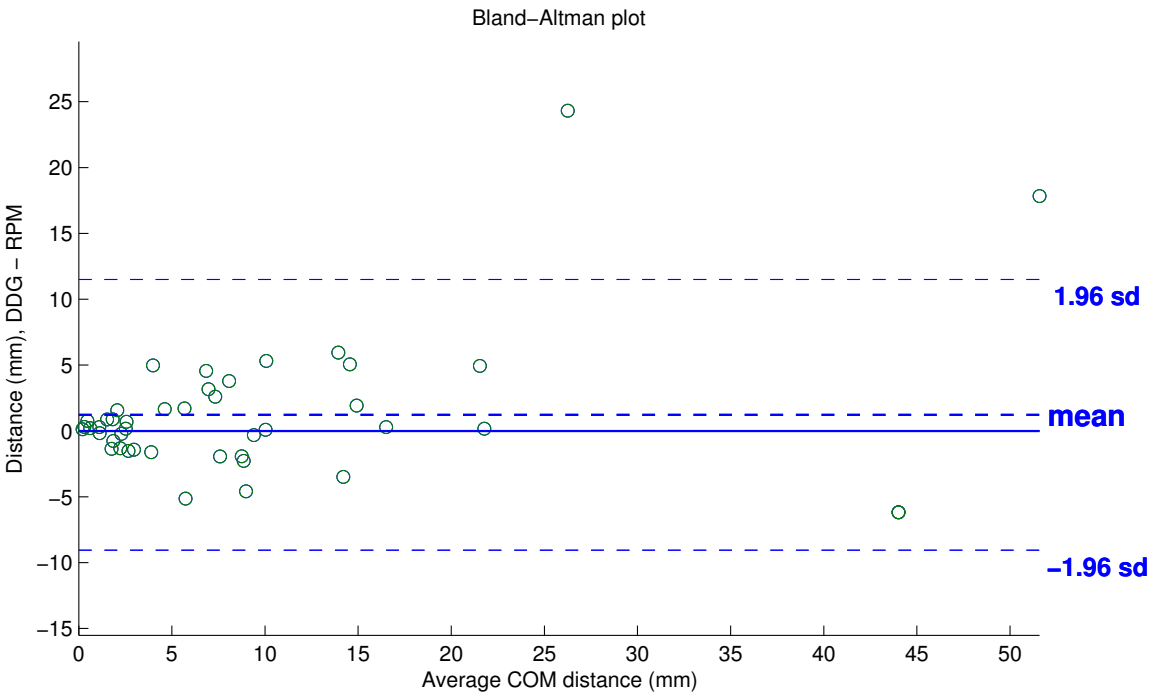

Figure 3.5: Bland-Altman plot comparing the total COM displacement in VOIs defined on the data-driven and RPM gated datasets. On average, the data-driven gated images produced greater COM displacement, however no significant difference was found between the two methods ($p = 0.13$).

gating method, however a paired t-test showed no significant difference was found between the two data sets ($p = 0.13$).

When the differences in overall COM change were grouped into local anatomical regions (bowel, abdominal wall, kidney, liver/stomach, lung), shown in table 3.1, no significant difference was found in any of the regions.

3.4 Discussion

In comparison to 3D, the contribution of scatter and randoms to the count rate is less in 2D, however overall sensitivity is higher in 3D. The gating method was shown to work effectively on 3D list mode events spanning 5 or less crystals.

In this work, a true gold standard for the respiratory signal is not known.

Region	COM (mm)	p-value	n
Abd. Wall	0.8	(0.30)	10
Lung	-0.9	(0.30)	12
Stomach	-0.9	(0.35)	6
Kidney	-3.3	(0.20)	13
Bowel	-0.9	(0.72)	3

Table 3.1: Difference in overall COM measured in anatomically grouped VOIS, showing p-value and the number of VOIs in each group. Positive difference infers greater distance measured on RPM dataset. No significant difference was found in any of the regions.

Validation of the gating method against known motion would require a dynamic physical phantom or simulation with a dynamic digital phantom, however these methods do not easily represent the variations in activity distribution and respiratory motion of clinical patient data. The RPM system is a commercially available means of acquiring respiratory data, and while the accuracy of this system in multi-bed PET imaging is not known, it remains the manufacturer facilitated method of acquiring respiratory gated PET data on the GE VCT, and is widely used [103]. To evaluate the data-driven method with clinical data, data-driven gated results were therefore compared with the RPM gated results which represent the standard gating method.

The data-driven gating method was shown to produce respiratory signals that were comparable to those produced with the RPM method. The respiratory signal from the data-driven method is closest to the RPM signal for bed positions over the abdomen and chest, and the difference between the two signals increased in other positions. Examining the images visually, the results from both gating methods appeared similar, and no significant difference was found between displacement values measured on images gated using the two methods.

All bed positions were gated, including the head and the pelvis. This automatically provides respiratory motion information for the entire body, the extent of which is otherwise unknown, and with no additional overheads other than processing time. However, the gating method relies on there being detectable motion within each bed position in order to derive a respiratory signal. If no

or little moving activity is present in a given field of view, then the mask may incorrectly include pixels which are not subject to respiratory motion, resulting in a signal that is not related to respiration. The unpredictable assignment of listmode counts to sinogram gates could produce a noise mismatch with gates from other bed positions. While such a case was not found, it remains a caveat when applying the data-driven gating method to whole body PET imaging. A potential solution to this is to adjust the size of each amplitude gate during the binning process in order to maintain a constant imaging noise in all gates [34].

Calculating the direction of motion in each bed position also relies on moving regions of activity to perform a 1D registration. This failed in regions with minimal or no motion, and in most cases this had no visible effect on the images. In one case out of 75 the direction was not calculated correctly and the result was visible, although difficult to detect.

The dominant frequency component of respiration, f_{resp}, calculated from the lung position, was used in the remaining bed positions to restrict the frequencies analysed when determining which pixels are subject to respiratory motion (forming the mask). As the respiratory signal is generated by summing the values within the mask, using the lung derived f_{resp} in the remaining positions alters the placement of the mask, it does not form the respiratory signal itself. However, this relies on the assumption that the patient does not alter the respiratory frequency during the PET acquisition. A variation in frequency could result in incorrect pixels being classified with respiratory motion involvement, which could adversely affect the respiratory signal.

A limitation of this method is the use of a single, helical CT scan to attenuation correct all gated PET data. The CT is performed with the patient free-breathing, and at a speed of 137.5 mm per second, effectively acquiring locally static images with respect to the breathing cycle. Assuming ideal respiratory gating, the CT would approximately match the gated PET series in only one, or lie in between 2, of the gated images. The remaining PET gates would have different degrees of mismatch between the CT and PET. The importance of the effect of this mismatch on attenuation correction in whole body imaging outside the lung is not well understood. Attenuation correcting the PET data with a gated cine-CT has been shown to produce improved results in the thorax [99]. In

sub-diaphragmatic regions however, no moving air-tissue boundaries exist with the exception of air within the bowel and the abdominal wall. Using a cine CT in this region might not provide sufficient improvement in attenuation correction to justify the additional radiation dose, and a single, helical CT scan may provide adequate attenuation correction for the gated PET images. This requires further investigation.

The data-driven gating method was demonstrated to be suitable for implementation in whole body 3D PET imaging in the clinical setting. No modifications to the standard acquisition protocol are required; listmode data can be recorded in any PET acquisition on the Discovery VCT. In most cases, the method was shown to perform at least as well as the hardware based RPM method. While the method did not produce superior results to the RPM method in all cases, it presents an easy alternative to using a hardware based device which can also be prone to error and failure. In this study, the RPM signal was degraded in 5 cases due to obstruction of the reflective block. In studies by Liu et al [80] and Wells et al [147], a considerable number of RPM signals were un-usable due to incomplete or erroneous RPM data. A data-driven approach may provide a more robust alternative.

3.5 Conclusion

The data-driven gating system previously described in chapter 2 was adapted to use the respiratory frequency estimate from gating the bed position containing the lungs (identified from CT) for all bed positions, and to only accept list mode events which spanned 5 or less crystals axially. A method was successfully developed to identify the direction of motion in each bed position, and reverse the gates where necessary in order to gate 3D whole body PET acquisitions.

The data-driven gating method was shown to perform at least as well as RPM based gating in whole body, 3D PET imaging. Specific cases were found in which the RPM gating method recovered more motion than the data-driven method, however cases were also found in which the data-driven method recovered more motion. In all but one case, the direction of the gated bed positions was correctly identified. No significant difference was found between the data-driven gating

method and the RPM gating method when comparing the measured displacement in gated images, at all evaluated locations in the body.

This method provides an alternative to respiratory gating clinical 3D, whole body PET patient acquisitions without additional gating hardware. No modification to the departmental clinical PET/CT acquisition protocol was required to retrospectively produce the gated PET images.

Chapter 4

Comparing approaches to respiratory motion correction in NH_3 PET perfusion imaging

4.1 Introduction

Respiratory motion can cause both blurring in PET, and produce a spatial misalignment between PET and CT which results in attenuation correction errors. In cardiac PET/CT imaging, these attenuation correction errors have been identified as a source of artefacts which can resemble false defects [48, 88].

Several approaches to reducing the effect of respiratory motion in PET/CT imaging exist. These are of varying degrees of complexity, as detailed in chapter 1 where they are generalised into three categories, as summarised in figure 1.24. The first category, involves producing an attenuation correction map which more closely matches the *average* respiratory point represented in the static PET data. In the second approach, the PET acquisition is respiratory gated and a series attenuation correction images are produced that corresponds to the respiratory point in each PET gate. By adding the attenuation corrected PET images, the attenuation correction errors can reduce, however motion induced blurring remains. While each attenuation corrected PET gate presents an image approximately free of motion blur, an increase in noise results from reduced imaging statistics. To

overcome this, the attenuation corrected, gated PET image series can be registered and re-combined. This creates a single, motion free image of similar imaging statistics to the non-corrected and non-gated image.

Currently, a comparison between these approaches has not been presented in the literature. In this chapter, Ammonia (NH_3) cardiac perfusion PET/CT scans were used to compare 3 approaches to reduce attenuation correction artefacts with the standard method of attenuation correction that uses a helical CT. Following this, the effect of reducing motion blur is evaluated by implementing a motion correction approach.

Initially, the approach of using an averaged cine CT for attenuation correction was implemented. In this, a cine CT is acquired over one or more respiratory cycles, and the images at each position are averaged [2, 29, 110].

The second approach included respiratory gating both PET and CT data and performing matched attenuation correction. Gating separates PET and CT acquisitions into series of near motion free frames, that in sequence, represent one respiratory cycle. By gating both PET and CT acquisitions, each PET gate can be attenuation corrected with the CT gate from the corresponding section of the respiratory cycle [97, 99, 114].

A limitation to this approach is the considerable additional dose required to include a cine CT into the routine imaging protocol, and for this reason, a second matched attenuation correction approach was implemented. To avoid the requirement of a cine CT, a *pseudo* cine CT dataset can be produced from a standard, 3D, non-dynamically acquired helical CT. One method of obtaining this series of CT images which match the respiratory position of the gated PET images is by applying PET derived respiratory motion fields to the helical CT [32]. This formed the second matched attenuation correction approach used in this chapter.

Finally, non-rigid registration was used to motion correct and sum the attenuation corrected and reconstructed PET images from both matched attenuation correction methods.

PET and cine CT images were gated using the data-driven gating method described in chapters 2 and 3, which required adapting to function with the NH_3 cardiac PET data. To evaluate the effect of each method on attenuation

correction, PET-CT alignment and cardiac wall intensity were measured. Cardiac wall assessment was also used to determine the effect of motion correction.

4.2 Methods

Rest and stress scans from 37 patients were considered in this study, and images were acquired on a GE Discovery VCT PET/CT scanner (General Electric Medical Systems, Waukesha, WI). All patients received a rest and stress NH_3 PET scan, and each scan included a helical CT prior to the PET acquisition, and cine CT following the PET. The helical CT was acquired over 150.4 mm with 140 kVp, 20 mA, 0.4 sec/rotation, a pitch of 1.375:1, and reconstructed to 47 512×512 2.5 mm thick slices separated by 3.27 mm. Following the Helical CT, patients were injected with approximately 550 MBq of $^{13}NH_3$ and a 2D PET image was acquired for 26 minutes in listmode. For relative assessment of myocardial perfusion the initial rapidly changing portion of the scan is discarded [85], and in this work the 20 min of PET data 6 min post injection was used. The cine CT was then acquired at 140 kVp, 10 mA, 0.4 sec/rotation, 5.5 sec cine duration, 40 mm collimation, and reconstructed to 2.5 mm contiguous slices.

A Varian (Varian Medical Systems, Palo Alto, CA) real-time position management (RPM) hardware respiratory monitoring system was fitted to the patient to obtain a second respiratory signal for comparison with the respiratory signal derived from the data-driven method. ECG gating was not performed.

Voluntary patient movement was determined by measuring the displacement of the spine between the helical scan and the cine CT scan, which were on average 30 ($\pm$4) min apart. In 14 cases, movement greater than 5 mm was measured, and these datasets were excluded from this study. The remaining 60 individual rest or stress image datasets, were analysed further.

All patients consented to take part in the study which was approved by a national ethics committee.

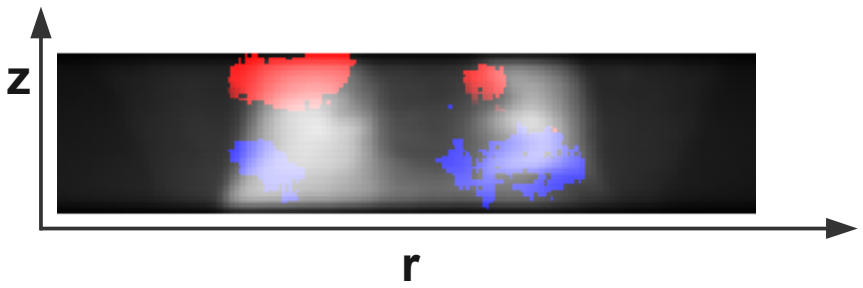

Figure 4.1: An example of a phase weighted mask overlaid on a projection image for an NH_3 cardiac PET image acquired from 6 to 26 min post injection. Uptake in the liver and myocardium both contribute to the respiratory signal.

4.2.1 Data-driven gating of NH_3 PET

The PET and CT data-driven gating method used in this work is fully described in chapter 2, and was shown to produce results comparable with hardware based devices in clinical, whole body FDG 3D PET imaging in chapter 3. Additional considerations were required to gate the NH_3 PET data.

The identification of pixels which are subject to respiratory motion is an unsupervised process, and for the NH_3 PET data, pixels in the liver and myocardium typically contributed to the respiratory signal. This is shown in an example phase weighted mask from a NH_3 cardiac PET scan in figure 4.1.

The respiratory signal is obtained by summing the counts in the dynamic PET series after applying the mask, so the 10 minute half life of ^{13}N must be corrected. Further to this, the combined uptake in the liver and myocardium regions throughout the 20 minute acquisition is difficult to predict, and tracer kinetics are likely result in change in the baseline of the respiratory signal.

After decay correcting for the 10 min half-life of ^{13}N, the respiratory curves

obtained from the data-driven gating method still demonstrated a gradual change in the baseline position in most cases (figure 4.2). This was assumed to result from tracer kinetics in the liver and myocardium. To correct for this variation, the respiratory curve was normalised to a 4th order polynomial function fitted to the respiratory curve, also demonstrated in figure 4.2.

Listmode data were gated into 8 bins. Amplitude gating was used, however the size (amplitude range) of each bin was adjusted such that an equal amount of acquisition time was assigned to each bin. This ensured similar noise statistics in each sinogram bin. Sinograms were corrected for geometric distortion prior to attenuation correction and reconstruction with filtered back projection (FBP).

4.2.2 Attenuation Correction Methods

Four approaches to attenuation correction were assessed. These included a helical CT, an averaged cine CT, a data-driven gated cine CT and a *pseudo* cine CT which was generated by applying motion fields derived from the NAC PET images to the helical CT. An attenuation correction map was created from each CT scan by applying a 10 mm FWHM spatial Gaussian filter, and CT Hounsfield units were converted to 511-kev μ values by applying the multi-linear transform used on the GE VCT. CT attenuation correction (CTAC) sinograms were formed by forward projecting the μ volumes and interpolating to the spatial coordinates of the PET sinogram.

Table 4.1 summarises the four approaches of attenuation correction, and the additional two methods which utilised motion correction.

1. **Helical CTAC (HCT).** The helical CT was was interpolated in the axial direction to match the positions of the PET slices prior to converting to CTAC. Gated PET sinograms were summed, attenuation corrected and filter back-projected to create the helical attenuation corrected PET volume, AC_{HCT}.

2. **Average cine CTAC (ACT).** All CT slices at each slice location of the 4D cine CT were averaged to create a single CT volume, which was interpolated in the axial dimension to match the PET position. Gated PET sinogram

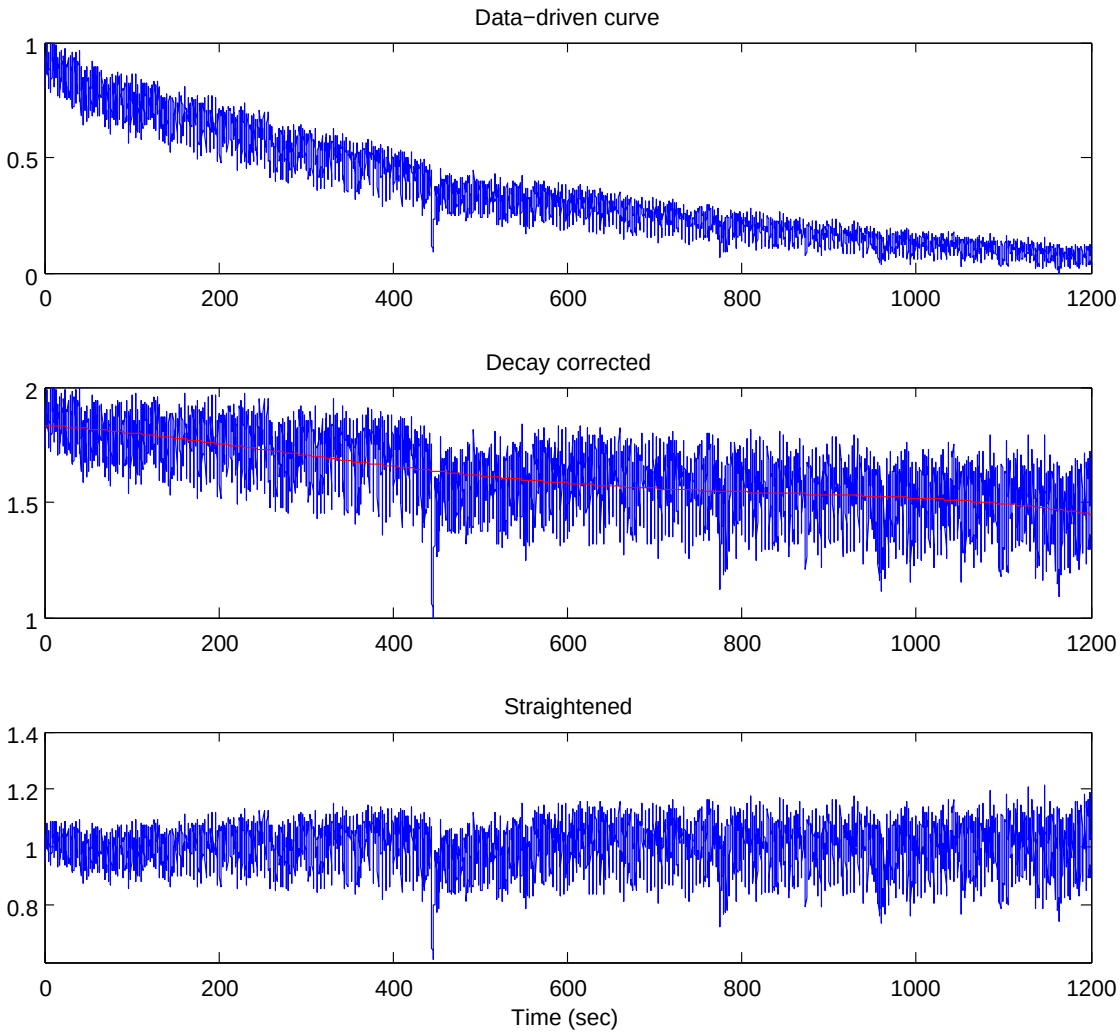

Figure 4.2: Data-driven curve for patient 1 (top). Decay corrected curve (middle) contains gradual decrease in baseline. A 4th order polynomial fitted to the decay corrected curve (shown in red). The decay corrected curve was *straightened* by normalising to the polynomial (bottom).

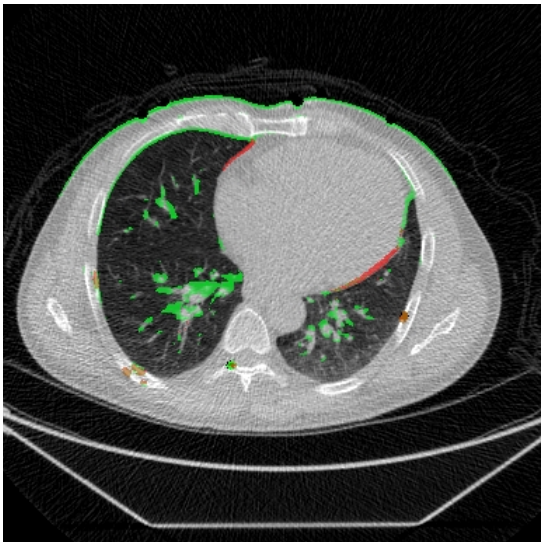

Figure 4.3: An example of a cine CT slice overlaid with the mask that identifies respiratory motion (green) and cardiac motion (red).

gates were summed, attenuation corrected with the CTAC, and filter back-projected to create the attenuation corrected PET volume, AC_{ACT}.

3. **Gated cine CTAC (GCT)** Two modifications to the CT data-driven gating method described in chapter 2 were implemented to reduce the contribution of cardiac contractile motion to the respiratory signal and to improve the continuity of the myocardium in the gated sequence. Firstly, pixels subject to cardiac motion were removed from the mask that identifies respiratory motion. Mask pixels with a frequency spectrum that exceeded a constant magnitude threshold of 1000 in the window of 0.71 Hz and 0.89 Hz were identified as regions of cardiac motion, and pixels in the frequency window of 0.18 Hz to 0.36 Hz were identified as regions of respiratory motion. Figure 4.3 shows an example of a CT slice overlaid with the binary mask which identifies cardiac contractile motion and respiratory motion.

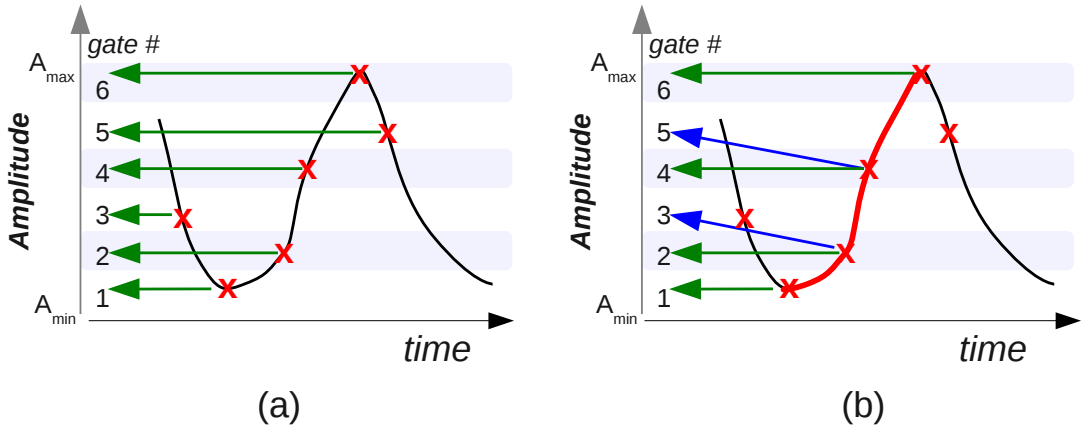

Figure 4.4: (a) The CT gating method used in chapter 2, gates are populated with images acquired when the signal matches the amplitude range for each gate. (b) The method used in this chapter, the longest continuous and monotonic section of the respiratory cycle is used to populate the gates. Missing data is filled with the nearest neighbour.

Secondly, in chapter 2 the CT gates were populated with the cine CT images acquired at time points where the respiratory signal matched the amplitude range of the gates. While this approach appeared adequate for lung tumour imaging, spatial discontinuities were noted along the myocardium with images acquired in this chapter. To reduce this effect, in this chapter, the longest continuous monotonic section of the respiratory cycle was found, and only images from that section were placed in the gates. Where no CT image was available for the amplitude range of a given gate, the slice from the closest point on the monotonic section of the respiratory signal was duplicated. A comparison between the two approaches is illustrated in figure 4.4.

A rigid body, 1 dimensional registration of PET maximum intensity projections and CTAC projections, as described in section 3.2.3 was used to identify the inferior-superior direction of motion from first to last gate in the gated PET and CTAC series. If necessary, the gated CTAC sinogram series was reversed to match the direction of motion in the gated PET se-

ries. Each PET sinogram gate was attenuation corrected with the matching CTAC gate, and reconstructed with FBP. Gated images were a) summed to create a single PET volume (AC_{GCT}), and b) motion corrected as described in section 4.2.3 to create $ACReg_{GCT}$.

4. **Pseudo cine CTAC.** A *pseudo* cine CTAC was created by applying the motion fields derived from the NAC PET images to the helical CTAC image. Figure 4.5 illustrates the process that was used, in which, firstly, the NAC PET gate that spatially matched the helical CTAC was identified (gate 7 in the diagram). This was done by approximating the superior edge of the liver in both the NAC PET and the helical CTAC as described in section 4.2.5, and the PET gate with the closest liver position to the helical CTAC was defined as the reference gate. This reference NAC PET gate was registered to each remaining NAC PET gate, creating 7 transformations which were then applied to the helical CTAC. This produced a CTAC for each respiratory position represented by the gated PET series, effecting an approximated gated cine CTAC sequence. Registrations were non-rigid, and performed with Niftyreg (version 1.3) [96]. This implements the B-spline based free-form deformation method developed by Rueckert et al [118] which uses normalised mutual information [28, 139] to determine image similarity at the voxel level. A $10mm^3$ final grid, 10 mm source and target filter, and a bending energy weight of 0.05 was used. Each PET sinogram gate was attenuation corrected with the corresponding pseudo gated CTAC gate and reconstructed with FBP.

   Attenuation corrected PET images were a) summed to create a single PET volume (AC_{pseudo}), and b) registered and summed to create a motion corrected volume as described in section 4.2.3 to create $ACReg_{pseudo}$.

4.2.3 Motion correction

Motion corrected images were created from the PET images that were attenuation corrected with the gated (AC_{GCT}) and pseudo (AC_{pseudo}) cine CTACs. To avoid compounding the effects of any remaining spatial misalignment between

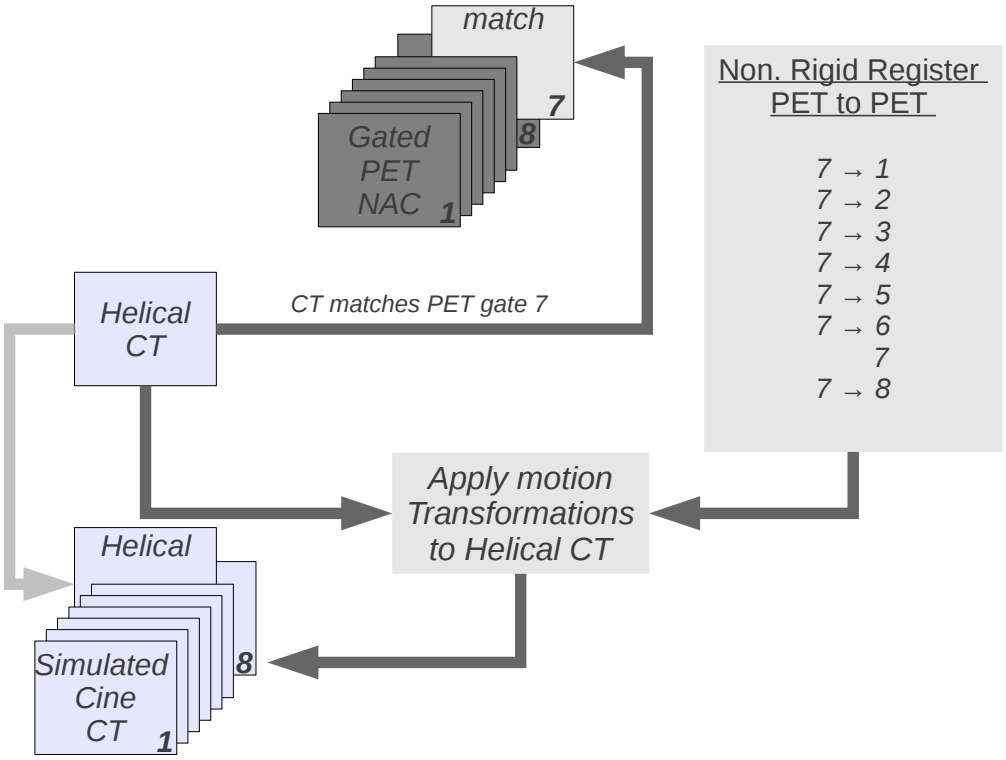

Figure 4.5: Flowchart describing the simulation of a cine CT by registering the PET gate which matches the helical CTAC to all remaining PET gates. The resulting transformation vectors are then applied to the helical CTAC.

Method	CTAC	PET	Atten. Cor.	Single resulting image
1. AC_{HCT}	helical	non-gated	non-matched	summed
2. AC_{ACT}	avg cine	non-gated	non-matched	summed
3. AC_{GCT}	gated cine	gated	matched	summed
4. AC_{pseudo}	pseudo gated	gated	matched	summed
5. $ACReg_{GCT}$	gated gated	gated	matched	registered & summed
6. $ACReg_{pseudo}$	pseudo gated	gated	matched	registered & summed

Table 4.1: Summary of the six attenuation corrected PET images created for each study. Motion correction was performed on gated and pseudo gated CT corrected PET images.

PET and attenuation correction maps, motion correction transformations were derived from gated, non-attenuation corrected PET images, and the transformations applied to the attenuation corrected images.

All NAC PET gates were registered to the maximum expiration gate which was assumed to be the gate with most superior centre of mass. Once the transformations were applied to the AC_{GCT} and AC_{pseudo} PET images, a single motion corrected image was obtained by summing the registered images to produce $ACReg_{GCT}$ and $ACReg_{pseudo}$. Niftyreg (version 1.3) [96] was used for all registrations, which were non-rigid, and performed with a $10mm^3$ final grid, a 10 mm source and target filter, and a bending energy penalty weight of 0.05.

4.2.4 Evaluation

The data-driven gating method was compared with the RPM based method to evaluate data-driven gating for NH3 cardiac imaging.

Methods 1-6 were then evaluated in 2 separate stages. Firstly, the different attenuation correction methods without motion correction (methods 1-4) were compared, and in the second stage the effects of implementing motion correction (methods 5 & 6) were evaluated.

Two metrics were used to evaluate the images. 1- PET-CT alignment; 2- relative change in myocardial wall intensities in attenuation corrected PET images.

i - Data-driven gating

To evaluate the data-driven gating method with NH_3 cardiac PET imaging, RPM and data-driven derived respiratory curves were compared. Additionally, non-attenuation corrected images were reconstructed from RPM gated and data-driven gated PET sinograms, and the range of liver and cardiac motion in each series compared. Motion range was defined as the difference between the organ position in the first and last gate, and the position was determined from profiles defined over the liver and myocardium on coronal images (see section 4.2.5).

ii - Attenuation correction

Alignment between the NAC PET images and each CTAC was first assessed to compare the four approaches of attenuation correction (methods 1 - 4). Liver and myocardium positions in each NAC PET and CTAC gate were determined from profiles over each organ as described in section 4.2.5. Alignment was defined as the absolute difference between NAC PET and CTAC positions averaged over all gates. For the gated and pseudo gated CTs, each NAC PET gate was compared with the matching CTAC gate, and for the averaged cine and helical CT each NAC PET gate was compared with the single static CTAC.

The four attenuation correction methods were also compared by measuring the myocardium intensity in the attenuation corrected images AC_{HCT}, AC_{ACT}, AC_{GCT} and AC_{pseudo}. The 3D AC PET images were rotated to create short axis slices, which were smoothed with a 3D Gaussian, 4.8 mm FWHM to reduce image noise. Two profiles, one towards the base and one towards the apex, were manually defined on each of the anterior, inferior, lateral and septal walls of the short axis slices. For each acquisition, one set of profiles were defined and copied onto all AC image datasets. The peak of each profile, as illustrated in figure 4.6, was used to indicate cardiac wall intensity.

As the true myocardial activity is unknown, relative change in myocardial intensity was used to evaluate attenuation correction methods 2-4, with the helical CT (method 1) as the baseline for comparison. When poor PET-CT alignment exists, the anterior wall of the myocardium in PET can correspond to lung in the CT, and this can result in under-attenuation correction and reduced activity

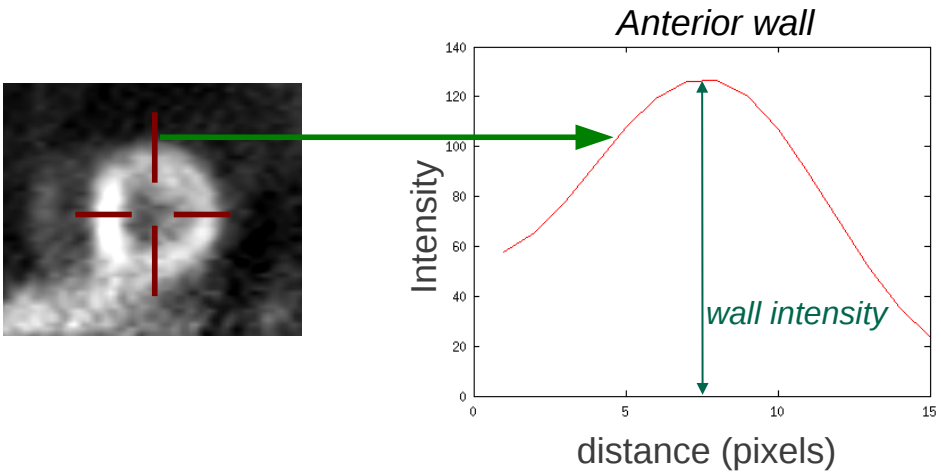

Figure 4.6: Cardiac wall intensity was determined as the height of profiles defined on short axis images.

in the attenuation corrected PET image. Replacing this CT with a CT that improves alignment is therefore expected to increase anterior wall intensity in the AC PET images, as illustrated in figure 4.7 (a). Conversely, a decrease in anterior wall intensity in AC PET would result if the replacement CT worsens PET-CT alignment (figure 4.7 (b)). A positive correlation between the change in PET-CT alignment and change in anterior wall activity is therefore expected, as illustrated in figure 4.7 (c).

iii - Motion Correction

The range of liver and cardiac motion was defined as the change in position from the first to last gate. This was determined on the non-attenuation corrected gated PET image series for both the motion corrected and non-motion corrected images. The accuracy of the motion correction was indicated by the decrease in motion range resulting from the application of correction.

Short axis profiles were also used to evaluate motion corrected images. Myocardial profiles on $ACReg_{GCT}$ and $ACReg_{pseudo}$ were compared with the non-

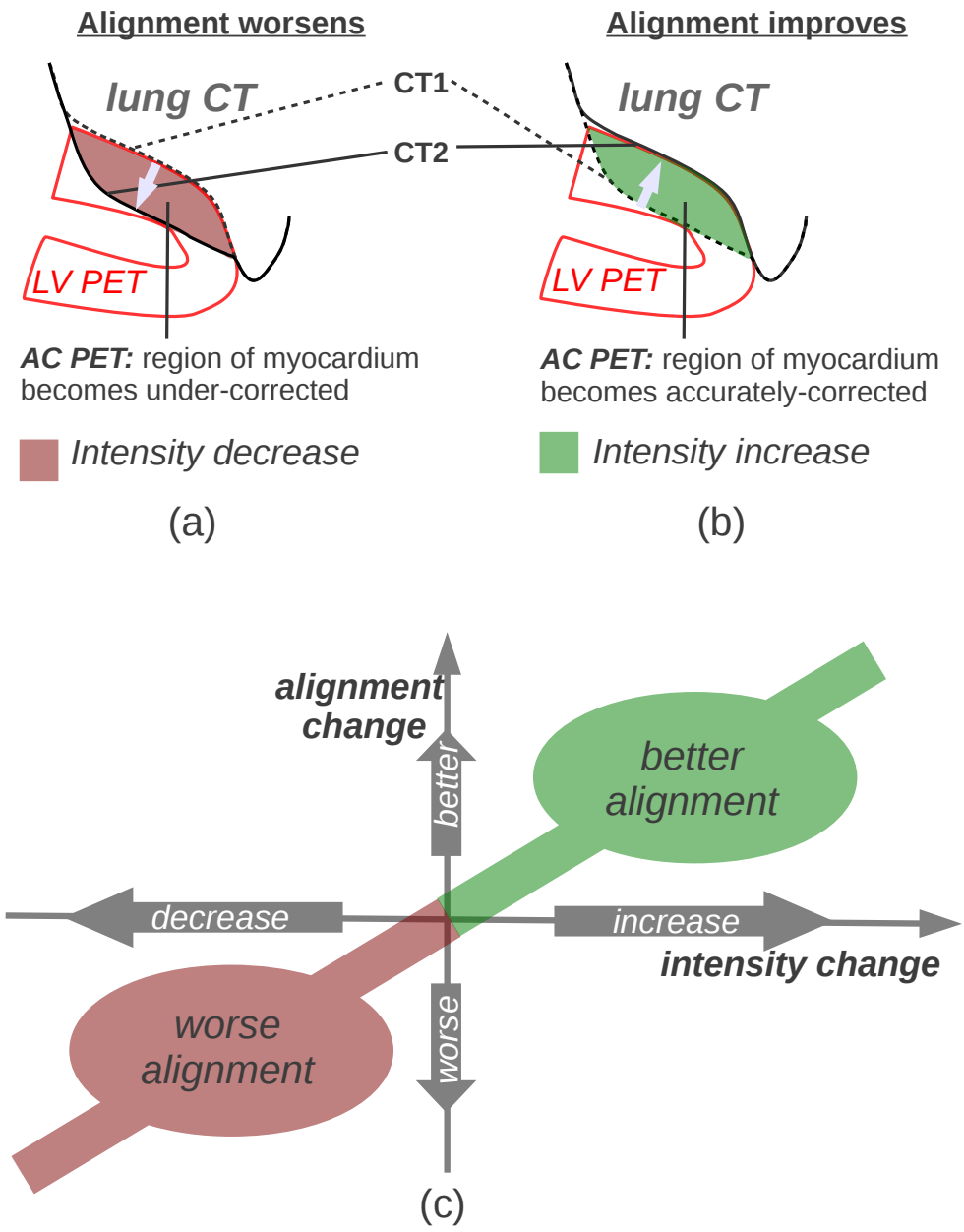

Figure 4.7: (a) Replacing CT1, which aligns correctly with the PET image, with CT2, which aligns poorly with the PET image, results in worse PET-CT alignment. Incorrectly using lung attenuation correction values for a region of the myocardium in PET (labeled *LV PET*) reduces the anterior wall activity in PET images. (b) Improved PET-CT alignment results when CT1 is replaced with CT2, resulting in an increase in anterior wall activity in attenuation corrected PET. (c) A positive correlation between the change in alignment and the change in anterior wall intensity is expected.

registered images AC_{GCT} and AC_{pseudo} respectively, and the change in cardiac wall intensity described the effect of applying motion correction. Application of the non-rigid transformations introduces a translation, invalidating direct comparison of the motion corrected and non-motion corrected images. So, for each scan, the motion corrected volumes were translated in 3 dimensions to match the position of the myocardium in the non-motion corrected volumes. This was done by iteratively translating the motion corrected NAC PET series such that the position of 9 profile peaks, 2 on each cardiac wall and 1 additional apical profile, matched the non-corrected NAC PET volume. The resulting translations were then applied to the motion corrected AC PET images.

4.2.5 Liver and myocardial edge

The location of the liver and myocardium along the z axis was necessary to match the helical CT scan with the gated PET (to produce the pseudo gated CT), and to evaluate the reconstructed PET images. To determine the position of these organs, profiles of the superior edges of the liver and myocardium were obtained from a coronal image. The coronal image was manually selected, and averaged with 5 anterior and 5 posterior adjacent slices. For PET images, a further 4 mm Gaussian filter was applied to this averaged, coronal slice.

An ROI was manually defined on the coronal slice and projected onto the z-axis, creating the profile. A straight line was fitted to the central segment of the profile which spanned 20% to 80% of the profile range. The point where where the fitted line intercepted 50% of the profile range defined the approximate location of the organ edge along the z axis. Figure 4.8 illustrates the liver edge definition for coronal PET and CTAC slices from the same patient. The displacement between the liver position in PET and CTAC is highlighted.

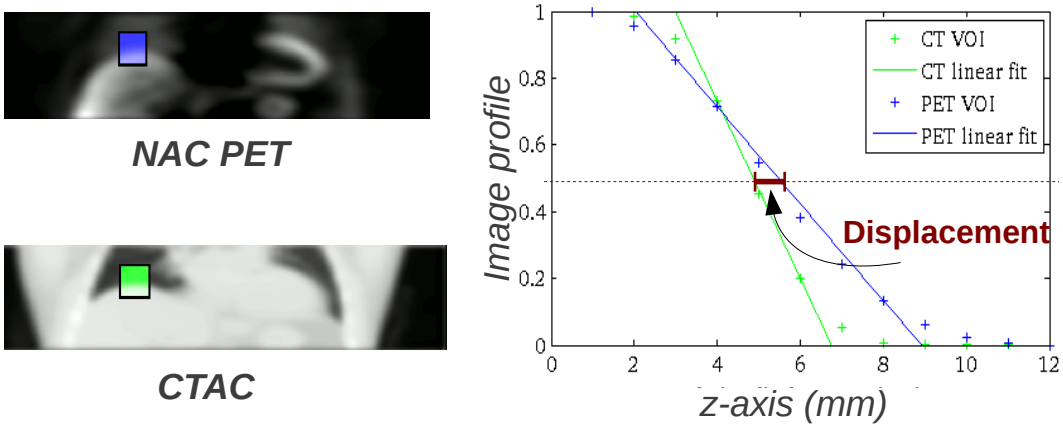

Figure 4.8: PET-CT alignment of the liver. A profile was defined along the z-axis over the liver edge in both datasets, and a straight line was fit to the section ranging from 0.8 to 0.2 of the intensity normalised profile. Alignment was defined as the z-axis separation between the two straight lines at y = 0.5.

4.3 Results

4.3.1 Data-driven gated PET

Considering all scans, NAC images gated with the data-driven gating method demonstrated an average of 11.8 mm motion, compared with 10.8 mm for RPM gated NAC images. No significant difference was found between the displacement ranges ($p = 0.052$). Figure 4.9 contains a Bland Altman plot of the range of cardiac motion calculated using both methods.

Eleven of the RPM curves were partially corrupt, where the reflective box was obscured from the optical camera. The remaining respiratory curves obtained from the two methods generally appeared visually similar, and the mean normalised RMS error between the two methods was 21%. In 6 of the 49 complete RPM curves acquired, the RPM data appeared to contain considerable baseline offset changes during the study, the data-driven curve did not contain this offset. In all of these 6 cases, the displacement range across the gates was larger for the

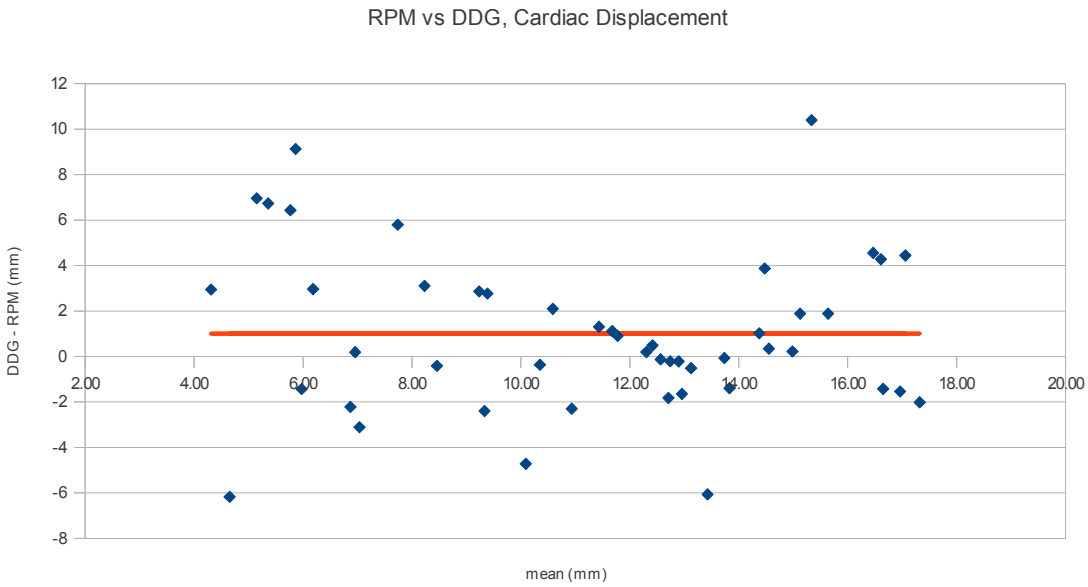

Figure 4.9: Bland Altman plot of the range of myocardial wall motion (first to last gate) of NAC PET images gated with the data-driven gating method, and the RPM gating method. No significant difference was found between the two methods when comparing the motion range ($p = 0.052$).

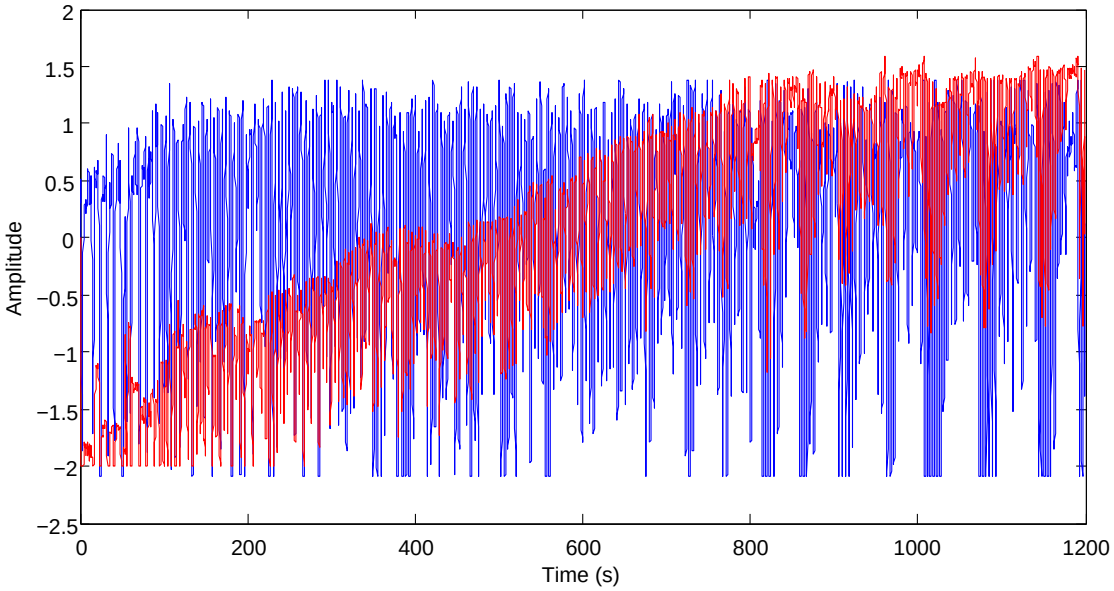

Figure 4.10: Patient 38, rest scan. RPM (red) overlaid with the data-driven curve (blue). The RPM curve demonstrates a gradual baseline increase throughout the duration of the scan. Larger displacement across the gates was measured on the data-driven gated images (9.8 mm) than the RPM gated method (6.7 mm).

data-driven method than for the RPM method. Figure 4.10 shows an example of this, where 9.8 mm of motion was measured on the data-driven gated images, and 6.7 mm was measured on the RPM gated images.

4.3.2 Gated and pseudo CT images

On average, the range of liver and cardiac motion measured in the pseudo gated CT was 13.1 mm and 6.9 mm respectively, significantly greater than the average motion measured on the gated cine, which was 7.6 mm and 4.9 mm. In 45 of the 60 scans, the pseudo gated CT produced a larger range of cardiac motion than the gated cine.

In 56 of the 60 gated cine CT images, cardiac contractile motion was observed along the anterior wall when visually assessing the gated cine CT sequence. The cardiac contractile motion was also seen as undulations in the myocardial position in 36 cases for the gated cine images. An approximate of the myocardial wall dis-

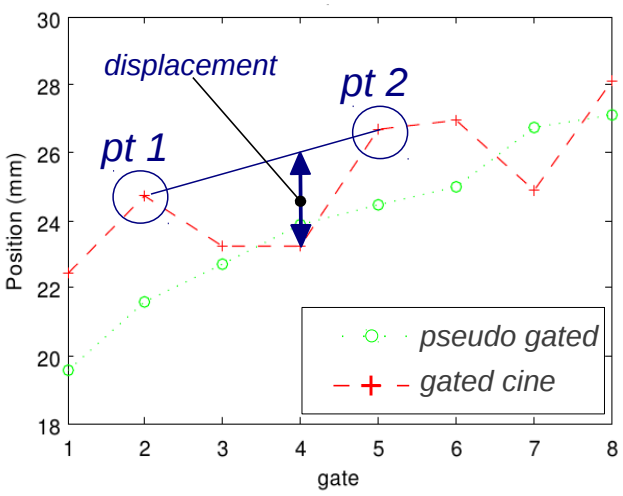

Figure 4.11: Cardiac wall position for gated cine CT (red dashed) and pseudo gated CT (green dotted) for an example scan with approximately 2.8 mm of cardiac contractile motion in the gated cine sequence. Displacement from contractile motion was estimated by fitting a straight line (shown in blue) between points either side of the undulation, and finding the maximum offset to the image derived displacement curve.

placement caused by contractile motion was determined by fitting a straight line between the two points either side of an undulation, and the displacement defined as the maximum offset between the wall position measurement and the straight line. This is illustrated in figure 4.11 where approximately 2.8 mm of cardiac contractile motion was measured in the gated cine CT image sequence. No cardiac contractile motion was noted on the pseudo gated CT sequences. For the 36 cases where cardiac contractile motion was observed in the cardiac displacement position of the gated cine CT images, on average, 3.9 mm of displacement was found (range 0.9 mm to 8.8 mm).

4.3.3 PET - CT alignment

Observing the overall PET-CT alignment for all scans, shown in figure 4.12, the pseudo gated CT produced the best liver and cardiac alignment, where the mean

alignment was 1.9 mm and 5.4 mm respectively. The helical CT produced the worst liver and cardiac alignment, with 5.2 mm and 6.5 mm respectively.

Compared with the helical CT, the averaged, gated and pseudo gated CTs all demonstrated improved average PET-CT alignment at the liver. The pseudo gated CT produced the best result, with an average of 3.3 mm improvement, and the averaged and gated cine CTs improved the alignment by 1.3 mm and 0.9 mm respectively. However, all three cine CTs demonstrated worse PET-CT alignment in some cases, by up to 11.5 mm for average cine, 13.1 mm for gated cine, but only up to 1.6 mm for the pseudo gated CT.

Over the superior wall of the myocardium, all cine CTs improved PET-CT alignment compared with the helical CT, but only the pseudo gated CT produced a significant improvement. All three cine CTs also produced cases where cardiac wall alignment was worse when compared with the helical CT. The pseudo gated CT produced the smallest degrading effect, up to 3.2 mm, where as the alignment worsened by up to 9.6 mm and 11.2 mm for the average and gated cine CTs respectively.

Compared with the average cine CT, the pseudo gated CTs improved average liver and cardiac alignment by, on average, 1.9 mm ($p < 0.05$) and 0.2 mm (not significant) respectively. Surprisingly, compared with the average cine, the gated cine produced slightly worse liver and cardiac alignment by, on average, 0.4 mm (not significant) and 0.6 mm ($p < 0.05$) respectively.

The pseudo gated CT significantly improved liver alignment by 2.3 mm when compared with the gated cine, and improved cardiac alignment by 0.8 mm.

Table 4.2 summarises the change in PET-CT alignment, comparing all combinations of CTs.

4.3.4 Cardiac wall profile analysis (non-motion corrected)

Cardiac wall profiles were defined on the short-axis attenuation corrected PET images AC_{HCT}, AC_{ACT}, AC_{GCT} and AC_{pseudo}. This section considers only non-motion corrected images, so the changes in AC PET images which result from using different CTs are attributed to attenuation correction and not blurring.

Initially, AC_{ACT}, AC_{GCT} and AC_{pseudo} were compared with AC_{HCT} to observe

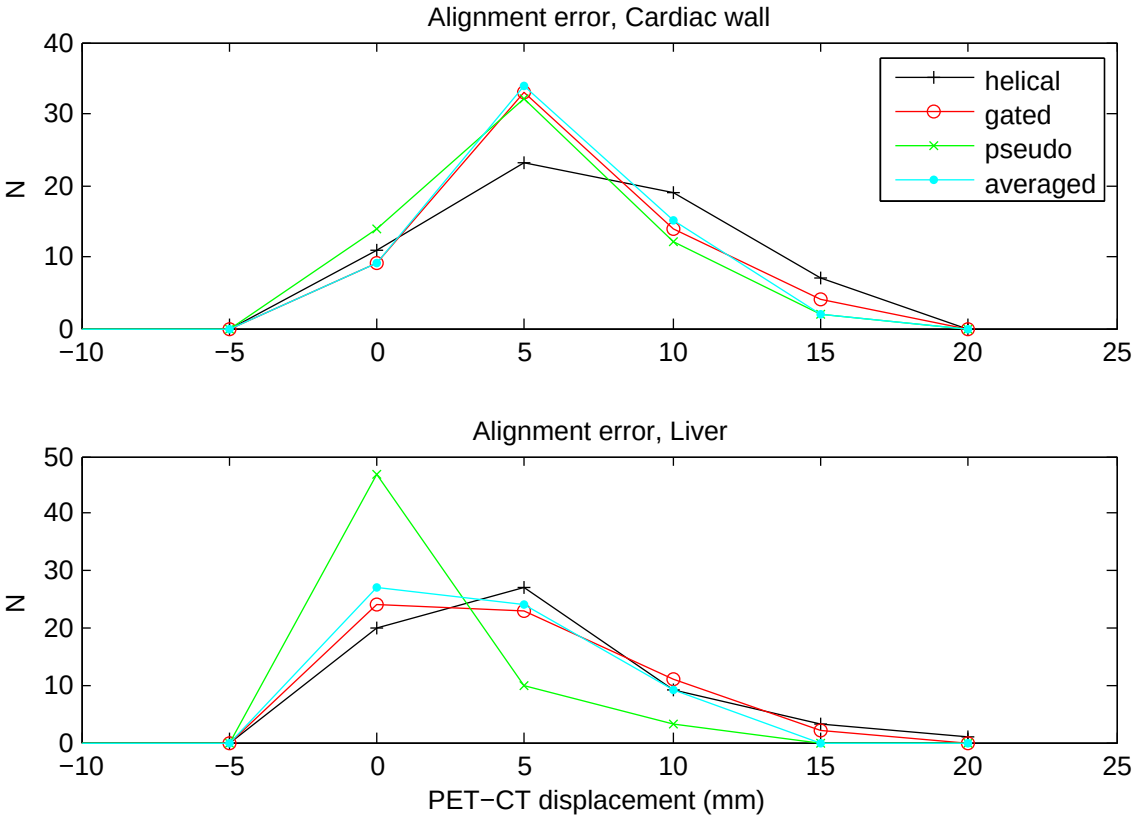

Figure 4.12: PET-CT alignment error averaged over all scans and all gates, at the anterior wall of the myocardium (top) and liver (bottom) for the helical CT, gated, average and pseudo gated CT CTs displayed as histograms. The helical CT produces the most errors, and the pseudo gated CT produces the least.

Baseline		Liver			Myocardium		
		ACT	pseudo	GCT	ACT	pseudo	GCT
HCT	mean	1.3*	3.3*	0.9	0.9	1.1*	0.3
	max	14.3	8.4	15.1	10.6	7.7	11.9
	min	-11.5	-1.6	-13.1	-9.6	-3.2	-11.2
ACT	mean		1.9*	-0.4		0.2	-0.6
	max		9.9	4.4		8.3	1.2
	min		-7.3	-6.8		-7.4	-4.0
Pseudo	mean			-2.3*			-0.8
	max			8.1			7.6
	min			-11.7			-10.7

Table 4.2: Mean, minimum, and maximum change in PET-CT alignment when each CT is compared with a baseline CT: i.e. $Alignment_{baseline} - Alignment_{new}$. A positive alignment change indicates an improvement, and negative indicates worse alignment. All values in mm. Asterisk (*) indicates significant difference ($p < 0.05$).

the relative change to the myocardium in PET when the typically used helical CTAC is replaced with the alternative methods.

Anterior wall profile changes were well correlated with the change in mean absolute PET-CT cardiac alignment ($\rho = 0.72, p < 0.05$), and in general the anterior wall intensity increased where alignment improved, and decreased where the alignment was worse. Figure 4.13 shows the percentage change in wall intensity and the change in alignment for each anterior wall short-axis measurement.

Exception cases were noted on the gated and averaged cine datasets where an increase in anterior wall intensity of more than 10% resulted from a worse PET-CT alignment. In these cases, motion artefact in the gated and average cine CTs produced a spatial discontinuity along the anterior wall, and the alignment measurement, recorded on coronal images, did not accurately represent the PET-CT displacement at the apical section of the anterior wall. In one case, an improvement in PET-CT alignment resulted in a decrease in anterior wall intensity of approximately 20%. In this case, the myocardium position in the helical CT was superior to the position in PET. While the absolute PET-CT alignment improved when the ACT and GCT were used, the myocardium position in these

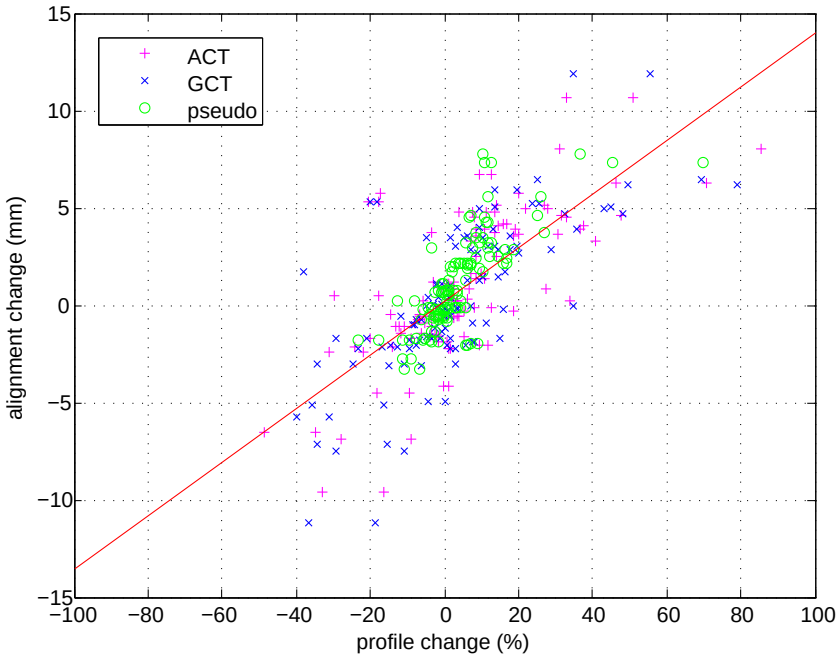

Figure 4.13: When the helical CT is replaced with the ACT, GCT or pseudo gated CT, the resulting change in PET-CT alignment of the myocardial wall correlates well with the resulting change in anterior wall intensity measured on the attenuation corrected PET. Generally, an improvement in alignment (a positive change) creates an increase in anterior wall intensity, and a worse alignment (a negative change) produces a decrease in anterior wall intensity.

CTs was up to 10mm inferior to the PET position in some gates, resulting in an under-correction of the anterior wall.

Figure 4.14 shows the change in the anterior and lateral cardiac wall intensities when the helical CT was replaced with the averaged, gated and pseudo gated CTs. More of a positive bias can be seen for the AC_{pseudo} PET images for both walls. The AC_{ACT} and AC_{GCT} PET images showed more cases of a large decrease in intensity. A decrease in anterior wall intensity of more than 10% was seen in 21 and 24 cases in the AC_{ACT} and AC_{GCT} PET images respectively, compared with only 6 cases in the AC_{pseudo} images. However, slightly fewer cases were found where the anterior wall increased by more than 10% in the AC_{pseudo} images, 25 cases, compared with 36 and 33 cases in the AC_{ACT} and AC_{GCT} images respectively.

Profiles over the septal and inferior walls were less affected by replacing the helical CT, however an increase of up to 22% and a decrease of up to 39% was found with the AC_{ACT} and AC_{GCT} PET images. No correlation was found between the change in inferior wall intensity and the change in cardiac wall alignment, however a correlation was found with liver alignment ($p < 0.05$). Similarly for the septal wall, a higher correlation with wall intensity change was found with liver alignment than with cardiac alignment. When the pseudo gated CT improved alignment by reducing a superior displacement of the liver, the inferior and septal wall intensity decreased by more than 10% in 13 cases, indicating attenuation overcorrection of the septal and inferior walls by superior displacement of the liver in the helical CTs.

Figure 4.15 contains bullseye plots and a horizontal long axis slice for an example patient scan where the gated, pseudo and averaged (not shown) cine CT's improve the alignment when compared with the helical CT. An anterior apical wall defect apparent in the AC_{HCT} PET image is not present in the AC_{ACT}, AC_{GCT} and AC_{pseudo} PET images. For this case, the mean liver and cardiac wall PET-CT misalignment was reduced from 10.6 mm and 7.9 mm respectively when the helical CT was used, to 2.7 mm and 3.0 mm for the gated cine CT, and 4.7 mm and 0.6 mm for the pseudo gated CT.

Figure 4.16 shows the horizontal long axis and bullseye plots for an example where the gated cine CT produced worse cardiac PET-CT alignment (11.5 mm)

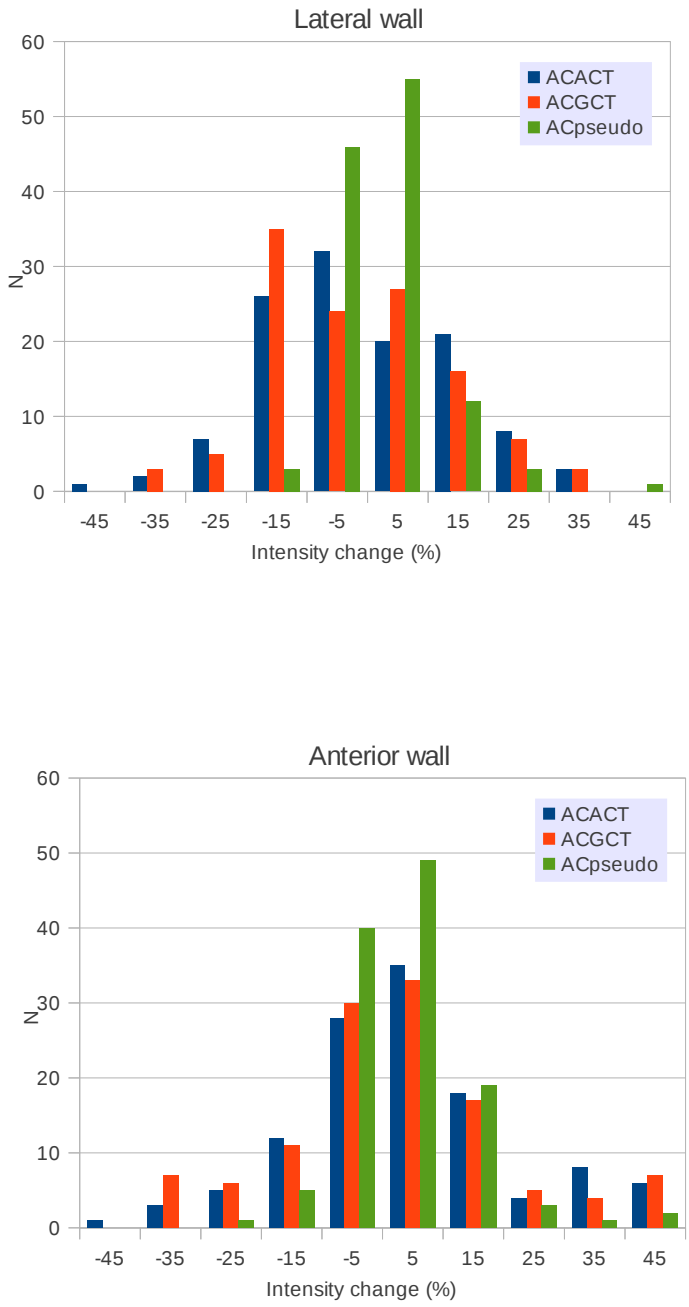

Figure 4.14: The percentage change in cardiac anterior and lateral wall intensities in PET images when the helical CTAC was replaced with the average, gated and pseudo gated CTACs. More of a positive bias is seen with the AC_{pseudo} images.

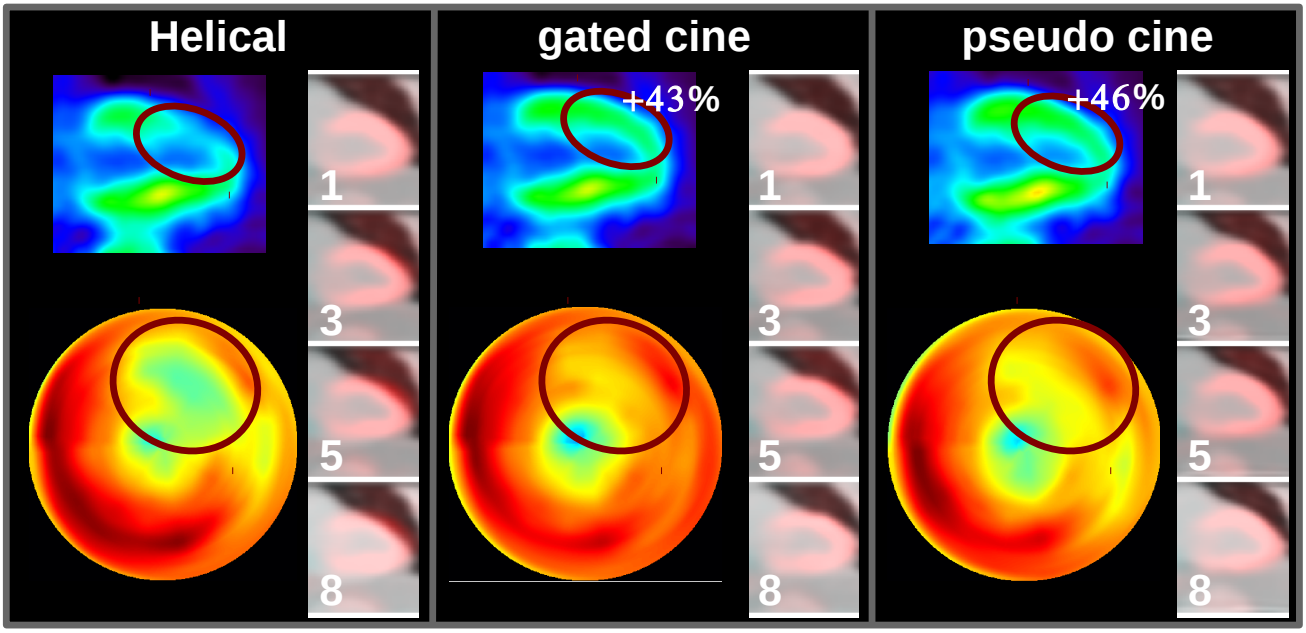

Figure 4.15: An example where PET-CT alignment improved from 7.9 mm with the helical CT to 3.0 mm and 0.6 mm for the gated and pseudo gated CTs respectively. Anterior apical defect on the AC_{HCT} PET images is not present in AC_{GCT} and AC_{pseudo}, and the anterior wall increased by 43% and 46% respectively.

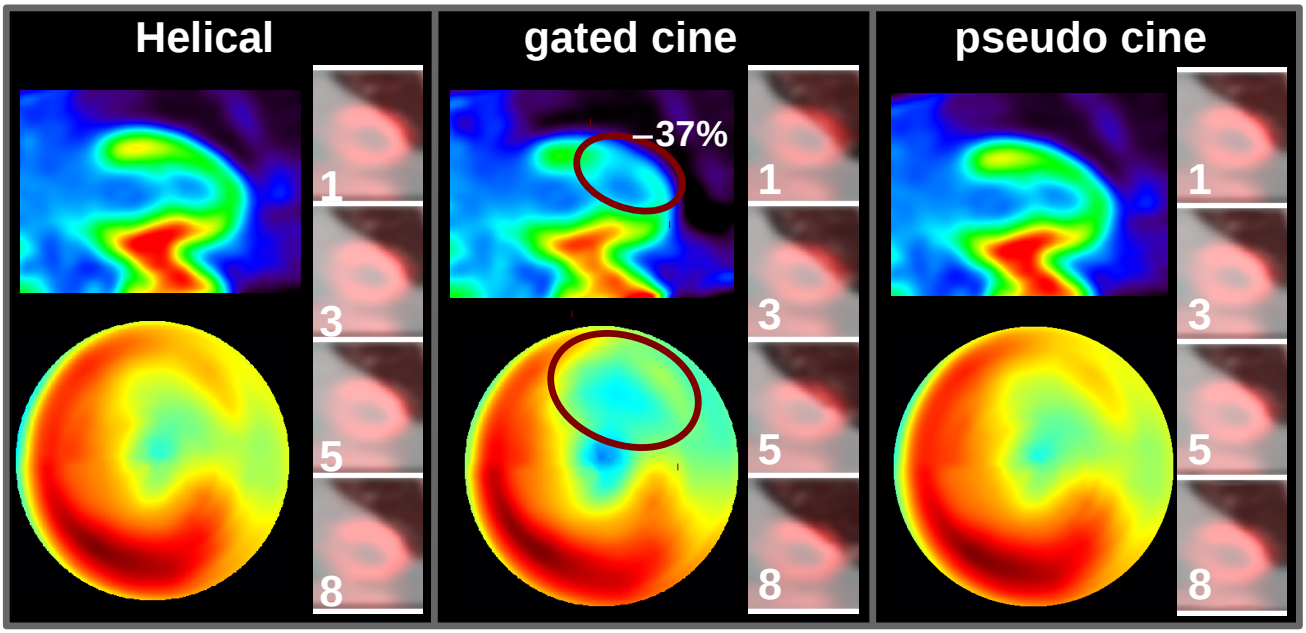

Figure 4.16: Cardiac PET-CT alignment is decreased from 0.3 mm with the helical CT to 11.5 mm with the gated cine CT. A 37% decrease in the anterior wall of the AC_{gated} AC PET images appears as a defect. Cardiac PET-CT alignment for the pseudo gated is 1.6 mm, and no anterior wall defect is seen.

than the helical CT (0.3 mm) and pseudo gated CT (1.6 mm). A spatial PET-CT misalignment with the gated cine CT results in an artefact which appears as an anterior wall defect and is seen in the AC_{GCT} PET image but not in the AC_{HCT} PET image. A 37% decrease in anterior wall intensity was found with the AC_{GCT} PET data. The AC_{pseudo} PET images were not visually different to the AC_{HCT} images.

When the averaged cine CT was considered as the standard CTAC for comparison, replacing this with the gated cine CT increased the anterior wall intensity by more than 10% in 2 cases, and decreased the anterior wall intensity by more than 10% in 6 cases (mean 20%). Replacing the averaged cine with the pseudo

SA Wall	$PET_{GCT}reg$	$PET_{pseudo}reg$
Anterior	4.0	4.4
Inferior	4.6	4.7
Septal	1.3	1.3
Lateral	-0.4	0.7

Table 4.3: Average change in short axis wall intensities resulting from motion correction. All values expressed as a percentage.

gated increased the anterior wall by more than 10% in 23 cases (mean 29%), and decreased by more than 10% in 21 cases (mean -20%).

4.3.5 Motion correction

This section considers the effect of motion correction only, and the changes to AC_{GCT} and AC_{pseudo} which resulted from applying motion correction demonstrate a change in motion induced blurring, and not attenuation correction.

The range of motion was measured on the NAC PET images before and after motion correction. On average, the range of liver motion reduced from 12.2 mm to 1.0 mm, and the cardiac wall respiratory motion range reduced from 8.3 mm to 0.8 mm.

Applying motion correction significantly increased the average intensity of the anterior and inferior walls. Table 4.3 shows the average change in all short axis wall intensities when motion correction was applied. The change in wall intensity was significantly correlated with total respiratory motion range for the anterior and inferior walls, however, no correlation was found for the septal and lateral walls. These effects are demonstrated in figure 4.17, which shows the change in cardiac wall intensity for all walls with respect to the total respiratory induced displacement range.

In 13% of cases, the non-rigid correction increased the anterior wall intensity by 10% or greater. Figure 4.18 shows representative short axis slices for a case where motion correction increased the anterior wall intensity by 26% for the AC_{GCT} images, and 28% for the AC_{pseudo} images.

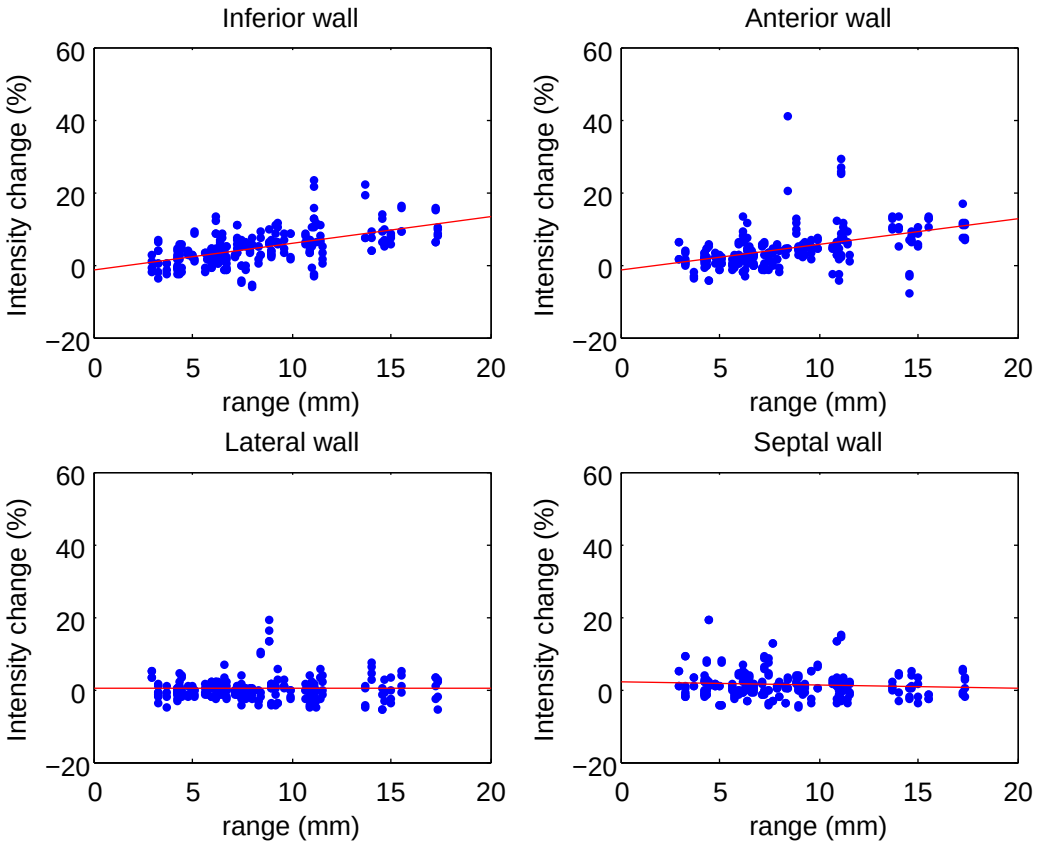

Figure 4.17: For the anterior and inferior walls, a significant ($p < 0.05$) correlation was found between the effect of motion correction (the change in profile maximum measured on $ACReg_{GCT}$ and $ACReg_{pseudo}$) and the range of respiratory induced motion measured on NAC gated PET images. No correlation was found for the septal and lateral walls.

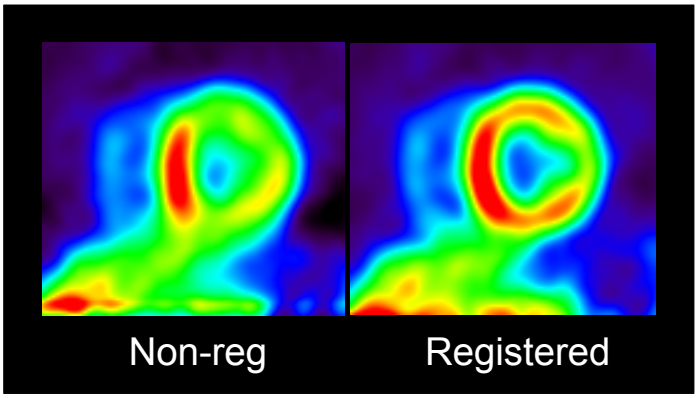

Figure 4.18: Short axis slices for the non-registered AC_{GCT} (left) and registered $ACReg_{GCT}$ (right) PET images. Registration increased the anterior and inferior wall maximum by 26% and 19% respectively.

4.4 Discussion

Cardiac perfusion NH_3 PET imaging appears well suited to data-driven gating, and the gating method used in this work produced similar results to the RPM hardware based method. This was expected, as compared with the lungs, uptake in liver and myocardium is typically high in NH_3 perfusion images, providing high contrast edges which move with respiration. Although no significant difference was found between the data-driven and hardware based gating methods, on average, more motion was measured on the data-driven PET images than on the RPM gated images. Considering that 11 of the 60 RPM acquisitions failed, the data-driven method may provide a more robust approach to obtaining gated PET for NH_3 cardiac perfusion imaging.

Given the tracer dynamics during the 20 min acquisition, low frequency changes in baseline position of the respiratory curve were removed from the signal prior to gating. Six cases of baseline changes in the RPM signal were found, and it is not clear if it is correct to remove this component of the respiratory signal. Dawood et al [34] respiratory gated seven FDG PET patients and found that removing baseline drift made no difference to the results. However, for the 6 cases found with baseline drift in this work, significantly more motion was mea-

sured, 4.3 mm on average, in the data-driven gated PET images with baseline component removed, compared to the RPM gated PET images with the baseline change remaining.

PET-CT misalignment can lead to attenuation correction errors, which in cardiac imaging, can present as false defects. Compared with the helical CT, the averaged, gated and pseudo gated CTs, on average, improved the liver and cardiac PET-CT alignment. Importantly however, all methods were also shown to worsen the alignment in some cases. As a consequence of worse alignment, the averaged cine CT decreased the anterior wall intensity in AC PET images by more than 10% in 21 out of 60 cases, which is comparable to findings from other groups; Alessio et al found that in 23% cases the averaged cine produced unacceptable PET-CT alignment [2], and Gould et al found artefactual defects in both helical and averaged cine datasets in 19% of cases [48].

A high correlation between the change in cardiac PET-CT alignment and the change in wall intensity was found for the anterior and lateral walls. PET-CT misalignment of these walls is expected to reduce all intensity in AC PET images, as attenuation under-correction results from replacing myocardium μ values with smaller lung μ values. No cases were found that suggested attenuation overcorrection of the lateral and anterior walls, in which a superior displacement of the myocardium would increase anterior or lateral wall intensity. We therefore assume that an increase in the intensity of the lateral and anterior walls reflects an improvement on accuracy, and a decrease indicates a loss of accuracy.

While the inferior wall is also prone to under-correction from inferior displacement of the liver in the CT [93], over-correction of the septal wall can also occur when the liver position in the CT is above the position in the PET [48]. Cases of under correction and overcorrection for the septal and inferior walls were found, and it therefore follows that an increase in septal or inferior wall intensity does not necessarily indicate improved accuracy, nor does a decrease necessarily indicate loss of accuracy. Given that true uptake in the myocardium is not known, liver PET-CT alignment provides the best indication of accurate inferior and septal wall attenuation correction. As such, the averaged, gated and pseudo gated CTs all improved liver alignment, but the pseudo gated performed the best. All three cine CTs demonstrated cases where liver alignment worsened. Alignment was up

to 13.1 mm worse for the averaged and gated cine CTs, however for the pseudo gated CT the largest degradation of alignment was only 1.6 mm.

A degradation of alignment and resulting decrease in anterior wall intensity occurred in more cases and to a greater extent when the helical CT was replaced with the averaged and gated cine CTs, compared with the pseudo gated CT which produced fewer and less severe cases. Conversely, however, when the alignment improved and the intensity of the anterior wall increased as a result, the averaged and gated cine CTACs had a greater effect than the pseudo gated CTAC. This is reflected in the 21 cases where the AC_{ACT} PET images produced more than 10% increase in anterior wall intensity when compared with AC_{pseudo}.

In general, the gated cine CT data did not appear to improve PET-CT alignment when compared with the averaged cine, and cardiac contractile motion may have contributed to this. Observing clinical data, Pan et al found that cardiac contractile motion was not sufficient to cause attenuation correction errors, although further investigation was suggested [109]. However, cardiac contractile motion was visually apparent in the majority of gated cine CT images acquired in this study, and in half of the cardiac wall displacement trajectories. This appeared to create spatial discontinuity between bed steps in the gated sequence, and degrade the PET-CT alignment in some frames. Using ECG triggering to acquire the cine CT during end-diastole state may provide a means of reducing or eliminating this effect, and consequently improve PET-CT alignment of respiratory gated studies. It seems possible that cardiac motion may also affect the fast rotation helical CT acquisition and consequently degrade the helical and pseudo gated CT PET-CT alignment. Koepfli et al, however, found ECG gating was not necessary for helical CT scans used to attenuation correct myocardial perfusion PET studies [68], although respiratory gating was not used during the PET acquisition.

Despite the significant correlation between the effect of motion correction and the range of respiratory induced displacement, the cases where motion correction produced the largest change in inferior and anterior wall intensity were not necessarily the cases with the largest motion range. A likely explanation for this is the variation in respiratory characteristics between patients, both the amplitude of motion and the amount of acquisition time spent at maximum displacement will

determine the effect of motion in the PET image. Liu et al [80] created histograms of relative respiratory displacement based on respiratory traces, and classified the histograms into three categories. Histograms demonstrating a higher peak, i.e. the patient spent lest time at maximum displacement were defined as *type 1* ; histograms demonstrating a broader peak were defined as *type 2*; histograms with flatter distribution, i.e. similar time was spent at each displacement, were defined as *type 3* . They found that *type 1* curves resulted in images that were less prone to motion effects.

When the histograms of patients in this study with more than 8 mm of motion were examined, patients with a *type 1* histogram (higher peak) had a smaller effect from motion correction, 4.8% on average, than patients with a flatter *type 2* histogram which produced an average effect of 7.7%. This difference was not significant ($p = 0.2$), however the average range of motion was 12 mm for the *type 1* group, larger than the *type 2* group which was 9 mm. Cases where the histogram type could explain the difference in registration effect were found, however exceptions to this were also found as exemplified in figure 4.19 which shows three histograms from 3 respiratory traces. Additional factors may explain these exception cases, including thickness of the cardiac wall and the amount of blur remaining in the gated PET data. Moreover, a variable amplitude gating method was used which produces gates of equal noise, and a potential consequence of this is increased residual motion in some gates.

The findings of this study are limited to the specific methods of reducing respiratory motion which were used. Simple approaches to each concept were implemented, and improvements to each of the methods may alter the results. Average cine CT was chosen as this is the method currently available on the scanner used in this work, however a maximum intensity projection cine CT has been shown to produce superior results [2]. All cine CT images were gated with the data-driven gating method, and cases where this method performed poorly were found. An improvement to the gating could reduce the occurrences of degraded PET-CT misalignment, and other data-driven CT gating methods may produce superior results [18, 76, 134, 148, 150]. While the data-driven method used in this work performed well with the PET data, other PET specific methods should also be considered for potentially improving the gated PET data [15, 17,

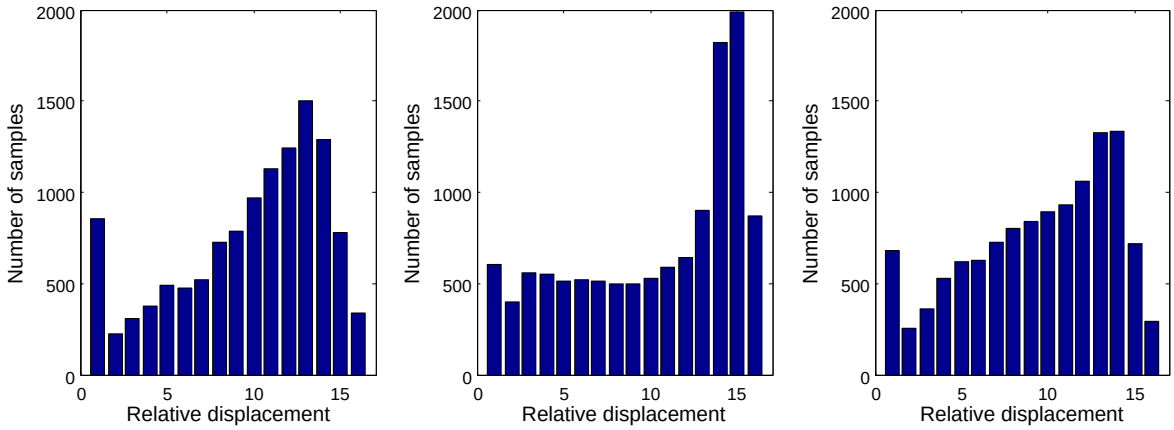

Figure 4.19: Histograms of relative displacement based on respiratory curves from 3 example patients, all with a cardiac respiratory displacement range of 11 mm (determined on NAC PET images). Type 2 curve on the left demonstrated 27% improvement from motion correction, and the type 1 curve in the centre demonstrated a 3% improvement. On the right however, another type 2 curve produced only 5% improvement.

63, 134, 141]. Finally, the pseudo gated CT was derived in a simple fashion by applying PET derived motion fields to the helical CT. McQuaid et al have produced a detailed method of generating cine CTs from static CT images [92], and Alessio et al has shown that consistency criteria can also be used to reduce respiratory motion artefact in cardiac PET imaging [1]. These approaches may improve the results for the pseudo gated CT approach.

Motion correction appeared robust as it did not appear to create cases of a large decrease in anterior or inferior wall intensities. Only 13% of anterior wall profiles improved by 10% or more when motion corrected. This appears low, however these results represent correction for motion only, as the attenuation correction maps had already been corrected for spatial PET-CT mismatch. Furthermore, this implementation of motion correction could potentially improve, gated and reconstructed images were individually registered to the expiration gate and summed to create the motion corrected image. Other registration methods such as optical flow [35], combining the registration within iterative reconstruc-

tion [71, 77, 87, 113, 115], and combining the generation of a pseudo gated CT with registration and reconstruction [6] could all potentially improved the results.

Limitations of the methods used for measuring the PET-CT misalignment and measuring cardiac wall profiles must also be considered. Measuring the edge of an object in a PET image is not well defined because of resolution effects, and in this work the edge was approximated as the mid-point between the local minimum and maximum either side of the edge. This could be a source of error in the PET-CT misalignment values, however the results demonstrate that generally, the relative change in cardiac wall measurement approached zero as the PET-CT misalignment approached zero, supporting the accuracy of the approximation. Alignment values were, however, only calculated at one position on the myocardial wall and liver on the coronal images, which may not truly represent the misalignment throughout the entire area of interest, and cases were found where the mismatch at the basal region did not represent mismatch at the apical region. Similarly, only 8 cardiac wall profiles were measured, and some changes in the myocardium may have been undetected.

4.5 Conclusion

In general, improving cardiac PET-CT alignment increased the anterior and lateral cardiac wall intensity measured on AC PET, and degrading the alignment decreased the intensity of these walls. The inferior and septal walls were prone to both over attenuation correction and under attenuation correction from incorrect alignment of the liver. Compared with using helical CT as an attenuation correction map, the averaged, gated and pseudo gated CTs all improved the average liver and cardiac PET-CT alignment, however all three methods also produced cases where alignment was degraded and lateral and anterior wall intensity decreased. This occurred in more cases and to a greater extent for the averaged and cine CTs, and cases were found where artefacts appearing as defects were introduced. Conversely however, when successful in improving alignment, the averaged and gated cine CTs had a greater effect than the pseudo gated, and in some cases the averaged and gated cine CTs resolved artefacts which were unchanged by the pseudo gated. Careful assessment of spatial alignment is required

regardless of the attenuation correction method used.

NH_3 PET images are well suited to data-driven gating, and the method used improved (although not statistically significant) the average range of motion measured in gated PET images when compared with a hardware based method. However, the data-driven gated cine CT images were prone to artefacts, and this may have resulted from cardiac contractile motion.

Motion correction generally increased the inferior and anterior wall intensity, and the amount of change was correlated with the range of respiratory motion. While motion correction only produced a large effect in a small number of cases, up to 41% change in anterior wall intensity was demonstrated.

Chapter 5

Conclusions

Two primary effects result from respiratory motion during PET/CT imaging. Relative to the respiratory cycle, the long duration of PET acquisitions results in an averaging effect of respiratory motion over several respiratory cycles. This manifests as blurring, and consequently reduces the resolution, introduces spatial distortion, and degrades the quantitative accuracy of PET. Secondly, respiratory motion can produce a spatial mismatch between a helical CT scan, which represents a snap-shot of the respiratory cycle, and a slowly acquired PET. This can result in incorrect attenuation correction which can reduce the quantitative and qualitative accuracy of PET, and produce false-positive defects in the case of cardiac imaging.

Several approaches to reduce these effects have been suggested and these can be categorised into three approaches:

1. Production of a CT which more closely represents the average respiratory position in the PET image. This improves the attenuation correction errors resulting from respiration, but not the effect of blurring in the PET image.

2. Acquiring the PET and CT such that each represent matching positions of the respiratory cycle. This improves the attenuation correction errors which result from respiration. Gated attenuation corrected images contain reduced motion, however noise is increased. Gated attenuation corrected images can be summed to recover imaging statistics, however blurring is then re-introduced.

3. Using non-rigid motion correction to recombine all acquired PET data, producing a single motion-free image with equal statistics to the non corrected image. Both the attenuation correction errors and blurring are improved.

The first approach can be implemented by using breath hold techniques during the CT acquisition, but these are prone to error. An alternative is to acquire a 4D cine CT over at least one respiratory cycle, and average all acquired slices at each position. The resulting 3D image approximates the average respiratory position represented in the PET data.

To facilitate the second and third approaches, respiratory gating can be used to separate PET and CT acquisitions into near motion-free frames. By attenuation correcting each PET gate with the CT gate from the corresponding section of the respiratory cycle, the second approach introduces another solution to blurring and misalignment. However, gated PET data contains a fraction of the total acquired PET counts, resulting in increased noise if the standard total acquisition time is maintained. By motion correcting each PET gate to a common position and adding the data, the third approach produces a single motion-free image.

While hardware based gating is available on commercial PET/CT scanners, it requires configuration prior to imaging and can be prone to failure. Data-driven gating presents an alternative, which is capable of retrospective gating with no modification to PET imaging protocols.

In this work, a data-driven respiratory gating method for both PET and CT was successfully developed. The gating technique uses a spectral analysis to determine regions within PET sinograms, or 4D cine CT images, that are subject to respiratory motion. By observing the intensity change of these pixels over time, an estimate of the respiratory signal is derived. Original listmode PET and cine CT images are then retrospectively gated using this signal.

The gating technique was demonstrated with PET and CT data from 4 patients with confirmed lung carcinoma. Single bed position 2D PET images were acquired over the lung bases to include the diaphragm and FDG avid lung tumour, and a 16 cm cine CT was acquired. When compared with the hardware based method, the data-driven approach produced similar respiratory signals, with on average, 15.4 % and 8.4 % difference between the methods for CT and PET respectively. A similar range of tumour motion was also measured on PET and

CT images gated with both techniques. Finally, the data-driven gating method was shown to be robust, and apart from including a heavy spatial filter, a large variation in parameters did not greatly affect the gated images.

Extending the gating method to routine clinical whole body PET imaging formed the second aim of this work. This was successfully achieved by developing an additional method to join separate PET bed positions, and altering the procedure to exploit the assumption that the greatest respiratory motion is likely to exist at the lung bases. Gating of PET data was performed on 11 routine clinical FDG whole body patients, imaged in 3D, and using the reconstruction utilities on the PET/CT scanner.

The data-driven gating method performed well with PET data, and on average, recovered a slightly higher range of respiratory motion than the hardware-based method, suggesting the hardware obtained surrogate signal may not be as accurate. PET images of lung tumours and myocardium both provide a high contrast area of interest, and if this is subject to respiratory motion, a strong signal is expected. Indeed the data-driven method produced very similar results to the hardware based method for most lung cancer and cardiac studies. In the whole body studies however, an area of high contrast was not necessarily present in all PET bed positions. Regardless, a good correlation was found with the hardware based method in the lower lung and abdominal bed positions. This is encouraging; the gating method does not rely on a moving region of high contrast to detect a respiratory signal. A poor respiratory signal was obtained for other bed positions, particularly over the shoulders and pelvis. However this appeared to be of no measurable consequence, as no motion was detected in these regions in the hardware-gated images.

The final objective of this work was to compare and evaluate various approaches to reducing respiratory motion artefacts in the heart. Three approaches of reducing the PET-CT mismatch caused by respiratory motion were investigated: averaged cine CT, gated cine CT, and a pseudo gated CT. PET images attenuation corrected with the gated and pseudo gated CTs were then motion corrected using non-rigid registration, and summed.

All attenuation correction methods, on average, improved the PET-CT alignment in the myocardium and liver and increased anterior wall intensity of atten-

uation corrected PET images. However, all of these techniques also produced cases where the alignment worsened, and in some cases a false positive defect in the corresponding AC PET image resulted. This occurred in more cases, and to a greater extent, when the averaged and gated cine CTs were used compared with the pseudo gated CT. In contrast, for the cases where PET-CT alignment improved, the averaged and gated cine CTs produced a greater effect than the pseudo CT gated. When the motion corrected images were evaluated, on average, a small increase in anterior and inferior myocardial wall intensity was found, with a large increase seen only in a small number of cases. Motion correction appeared to have no detrimental effects however.

Cine CT data gated well when the lung cancer patients were considered, and in some cases the data-driven method produced gated CT images with less artefact than images gated using the hardware method. This was not the case for all cardiac patients however, and the results indicated that cardiac contractile motion could interfere with the respiratory signal. Cardiac contractile motion was apparent in the majority of gated cine CT image sets, and this is a possible explanation for the poor performance when using these images for PET attenuation correction. The pseudo cine CT, whilst more difficult to implement, was shown to provide a more robust alternative. Additionally, the pseudo cine can be generated from a standard helical CT, rather than requiring a high dose cine CT acquisition. Combined with data-driven gating method, this provides a mechanism for retrospectively performing respiratory motion correction on any clinical cardiac PET/CT scan with no modification to the acquisition parameters.

5.0.1 Data-driven gating parameter selection

Several parameters must be set prior to running the data-driven gating method, and these parameters mostly control the spatial filter, frequency window, mask size, and the post-filter applied to the respiratory curve. Values for these parameters were initially chosen experimentally such that accurate results were produced for all four patient datasets acquired in chapter 2. Parameters that describe the spatial filter, frequency window, and mask size were then varied over a wide range, and apart from a heavy spatial filter, no large effects were found.

This suggested an insensitivity to these parameters, so for PET imaging, the initial set parameters defined in chapter 2 which describe the spatial filter, the restrictive frequency window size (δ) and the mask size were retained for the 11 whole body and 60 cardiac scans in chapters 3 and 4 (allowing for the different crystal configuration in the newer PET/CT scanner used). Successful data-driven gating of these additional scans provided further evidence of a method which is in-sensitive to parameter selection.

The initial value for the post-filter applied to the respiratory curve was, however, doubled in chapter 3. This prevented over-smoothing of the curves which was otherwise noted when the initial value was used. A limited range of patient data was used in the first study (when the initial post-filter was defined), and it is likely that the wider range of respiratory characteristics introduced in chapter 3 resulted in some cases of over-smoothing. The new post-filter was retained for the cardiac data in chapter 4

Data driven cine CT gating was used in chapter 2 with lung tumour imaging data, and in chapter 4 with cardiac imaging data. In chapter 4, two modifications to the initial gating method were described, including modifying the binning process to include only a temporally contiguous section of cine data at each position, and modifying the frequency windows to subtract pixels subject to cardiac contractile motion from the mask. These changes were necessary as spatial discontinuities were noted along the myocardial wall, which was also the region where the reduction of respiratory motion artefacts were being investigated. Myocardial wall discontinuities were not noted in the lung cancer gated CT images, however this included only 4 patients and it is possible that the initial gating method would also produced artefacts with a larger number of patients. Further to this, the initial datasets were acquired on a 4 slice scanner, which limited each CT bed position to 10 mm. The 60 cardiac cine CTs were acquired on a newer 64 slice scanner, with 40 mm CT bed positions. The larger cine CT bed positions could also contribute to the presence of artifacts.

While final the parameters used in chapter 4 do vary from the initial values used when the method was first developed in chapter 2, these modifications were required as more data was introduced. Generally, the gating method appears robust and insensitive the majority of parameters, however it is possible that when

the method is applied to more datasets, further modifications may be required.

5.1 Future work

Currently, using a 4D gated CT to attenuation correct matching gated PET data presents an immediate solution to the attenuation correction errors introduced by respiratory motion. However, using a gated cine CT to facilitate this increases the overall radiation dose to the patient considerably, and justification is required to include a cine CT in all PET/CT examinations, assuming the cine CT acquisition parameters used in this work. If the additional radiation dose could be reduced or eliminated, then the gating methods presented in this work provide a mechanism to routinely respiratory gate all clinical PET/CT acquisitions.

5.1.1 Dose reduction

Three main approaches to reducing the additional radiation dose required to obtain respiratory gated PET/CT acquisitions are suggested.

5.1.1.1 Parameter optimisation

A reduction in CT dose is possible by adjusting the acquisition parameters. In chapter 2, a tube current of 20 mA was used, and this was halved to 10 mA in chapter 3. This halved the dose, however 3 mSv still results from a 16 cm scan with 5.5 s cine duration and a tube voltage of 140 kVp. Further dose reduction is necessary for routine implementation, and technical limitations to modern CT scanners prevent reducing the tube current below 10 mA on most CT scanners (some modern PET/CT scanners are only capable of a minimum tube current of 20 mA).

Where further reduction in tube current is not possible, another approach to reducing CT dose is to lower the tube voltage. This has the combined effect of reducing both photon flux and photon energy. While photon flux is linearly proportional to patient dose, the effect of reducing photon energy on effective dose and image noise depends largely on patient size [125, 138], and the effect on PET attenuation correction is difficult to predict. Low dose helical CT images using 5

mA.s and 140 kVp have been shown to produce suitable attenuation correction for clinical whole body PET [59], however in the context of cardiac PET/CT imaging, Souvatzoglou et al found that CT images acquired at 80 kVp and 13 mA provided accurate attenuation correction [128]. Fahey et al suggested that dose settings as low as 80 kVp and 5 mA.s can be used for paediatric PET/CT imaging, but using these settings for adult acquisitions produced artefacts in attenuation corrected PET images and a minimum of 120 kVp was suggested for larger adults [40].

By reducing the tube voltage and current, a considerable reduction in dose can clearly be achieved. Investigation is required to establish how much the tube current and voltage can be lowered whilst retaining the ability to gate cine CT acquisitions and accurately attenuation correct the PET data. Recently Xia et al used simulations to assess various approaches to optimise CT acquisition parameters used when generating CT-based PET attenuation correction data, and included filtering techniques that exploit the reduced resolution required to attenuation correction PET [149]. Including variations in patient size would form an important extension to this work.

Recently, iterative CT reconstruction tools have been introduced to commercial PET/CT systems [36]. With this, CT dose can be reduced by 32-65% whilst retaining image quality [51]. Considerable dose reductions are therefore likely with 4D CT, and it is important to evaluate this new technology in the context of respiratory motion correction in PET/CT imaging.

5.1.1.2 Restrict additional cine CT

In chapter 3, respiratory motion was found from the upper chest to the lower abdomen. Retrospective gating of whole body clinical FDG PET acquisition was demonstrated to be feasible, however attenuation correction was performed with helical, non-dynamic CT. Extending a cine CT to cover 5 PET bed positions, approximately 61 cm spanning from the top of the lungs to the pelvis, results in a dose of approximately 8.4 mSv. To justify such a dose would require considerable additional diagnostic information to be gained by the cine CT scan, and evidence of this, other than in the thorax, does not exist.

It is possible that no significant benefit is provided by using matched attenuation correction in the abdomen. Apart from the abdominal wall and gas within the bowel, no air-tissue boundaries exist which are more likely to be affected by respiratory motion. By demonstrating that gated cine CT only significantly improves attenuation correction over the lungs and diaphragm of gated PET data, a simple means of eliminating a large portion of additional dose for respiratory gated PET/CT imaging would be presented by restricting the extent of the cine CT.

Combined with reducing the tube voltage and using noise reduction techniques described above (section 5.1.1.1) to produce low dose 4D gated CT in the lungs only, by demonstrating that non-dynamic CT is sufficient to attenuation correct gated PET data outside the lungs the effective dose could be reduced enough to permit routine application.

5.1.1.3 Eliminate additional CT

An alternative approach to reducing the dose associated with 4D CT is to artificially generate 4D CT data from a static CT using motion fields derived from PET. This was demonstrated in chapter 4 where pseudo cine CTs were generated from a helical CT scan using respiratory motion fields derived from data-driven non-attenuation corrected gated PET images. In the context of cardiac perfusion PET imaging, this method, although implemented in a simple manner, appeared to be more robust than using gated cine and averaged cine for attenuation correction. In the context of lung imaging however, it is not clear if the motion fields derived from NAC PET, particularly in the absence of a highly active tumour, will contain adequate detail to construct accurate 4D CT data throughout the lung.

Potentially, pseudo gated CTs could completely eliminate the requirement for 4D CTs, thereby maintaining the same effective dose as the non-gated PET/CT acquisition. It also presents an alternative to the restricted approach described above (section 5.1.1.2); if a helical CT does not accurately attenuation correct the gated abdominal PET, then a pseudo cine CT of this region could suffice. This approach does, however, rely on the assumption that the respiratory position in

the helical CT matches the respiratory position in one of the PET gates.

5.2 Dual gating

In chapter 4, three approaches to reducing respiratory motion induced attenuation correction artefacts were evaluated for cardiac imaging. All demonstrated cases of worse PET-CT alignment when compared with the helical CT. The gated cine CT performed surprisingly poorly, and cardiac contractile motion was identified as a possible cause of this. Eliminating cardiac contractile motion could improve the results, and this requires further investigation.

Dual respiratory and cardiac gating has been suggested as necessary to acquire reliable cardiac PET data [81, 132], and dual gating of PET has been demonstrated [67, 69, 72, 131]. However, an evaluation of using cardiac gated or dual gated CT for attenuation correction has not been performed.

Extending the data-driven gating method to recover cardiac contractile motion seems appealing, and the feasibility of extracting cardiac information from PET data has already been demonstrated [17]. Extracting this signal from a cine CT sequence, however, is not obviously possible. Consideration should be given to the averaging effect over the duration of each CT slice acquisition, and to the slow sample rate. On the GE Discovery VCT, a rotation speed of 0.4 s is possible, equating to a sampling frequency of 2.5 Hz, and a Nyquist frequency of 1.25 Hz. This is only fast enough to capture a periodic cardiac signal of up to 75 bpm. However, only a small portion of the cardiac cycle is spent in systole, so it is likely that a higher sampling frequency is necessary to extract the true non-sinusoidal signal. Increasing the rotation speed, or reconstructing slices from half rotations will increase the sampling frequency, however not all CT systems are capable of this. Hardware based ECG triggers may be required.

An alternative to obtaining cardiac gated PET and CT data over the full cardiac cycle is to retain only the diastolic section of the images. By prospectively gating the cine CT acquisition with an ECG signal, the x-ray tube can be switched off during the systolic state. This will remove most of the cardiac contractile motion from the cine series, however a temporally discontinuous sequence will be produced which may affect the data-driven respiratory gating method. In

PET, either only the diastolic component of the acquisition can be retained, or all cardiac gates can be elastically registered to the diastolic state [72].

In addition to the effect of contractile motion on myocardial imaging, cardiac contractile motion also contributes up to 16 mm of motion in lung tumours situated close to the heart [38, 117]. Dual gating seems likely to offer a means of further improving PET/CT FDG acquisitions of lung tumours, and this has not been explored.

5.3 PET/MR

Combined PET/MR scanners are now commercially available as either sequential or simultaneous dual modality systems. Sequential systems acquire images in series, in a similar manner to PET/CT scanners, and for the purposes of respiratory motion correction the only obvious advantage over PET/CT is the elimination of ionising radiation dose from the CT component. This introduces the possibility to obtain 4D MR data on all patients. However, one limitation of respiratory gating in PET/CT is the inability to manage different breathing characteristics during CT compared with the PET, and on a sequential PET/MR system, this problem remains.

Simultaneously acquired PET and MR, however, is not subject to this restriction, and motion fields extracted from the MR could be used directly to correct the PET images [26, 135]. Standard MR sequences do not produce a signal in lung and bone, and this can present an issues when using MR images to attenuation correct PET data and when deriving motion fields from the lung to motion correct PET images. Solutions to MR based PET attenuation correction have been suggested, however an evaluation of using lung motion fields derived from MRI to accurately motion correct lung tumours in PET has not been performed with clinical PET data.

5.4 Clinical significance and application

In this work, the clinical significance of applying gating and motion correction has not been considered. In oncological indications, the diagnostic reporting of

PET/CT images is frequently used to identify otherwise undiagnosed metastatic lesions. Motion correction has the potential to improve a PET image so that a more accurate visual representation and quantification of a motion affected tumour could result in a true positive rather than a false negative. A large scale study is required to determine if routine PET/CT studies should be respiratory motion corrected. Similarly in cardiac imaging, the clinical significance of motion correction is not yet well characterised. This work has shown the potential for motion correction to create, rather than resolve artefacts, and it is not clear whether the risks of implementing these motion correction methods are outweighed by the benefits.

An important limitation is the potential inadequacy of PET to provide accurate motion fields. We should consider the case where a lesion is not visible in the non-gated PET because of motion blur, and not visible in the gated PET sequence because of high image noise. Ideally, motion correction would accurately combine the gated sequence to reduce the image noise and remove motion blur, producing an image of high SNR such that the tumour becomes detectable. However, the poor SNR of the gated sequence may result in the tumour itself not contributing to the motion field. Inaccurate motion correction of the tumour could result in a tumour which is still non-detectable in the final image, and a false negative would remain. It may be that gated cine CT images, which contain fine detail of lung structure throughout the lung, could provide a more accurate motion field that in this case may result in a true positive.

Finally, as PET is beginning to be used in radiotherapy treatment planning, respiratory gated PET/CT images offer additional and potentially very useful information. Planning typically includes margins that surround tumours to account for possible respiratory motion, which consequently includes healthy tissue if over-estimated or omits tumour tissue if under-estimated. Using the motion trajectory obtained from respiratory gated PET/CT, this margin can be defined more accurately [9]. A caveat to this is the case where the gating system fails to accurately recover the motion trajectory, resulting in the incorrect reduction of the treatment margin. Secondly, inter-fraction and intra-fraction respiratory motion characteristics can vary considerably [89], introducing additional risk with implementing this approach. These points require careful evaluation before rou-

tine application of respiratory gating.

Bibliography

[1] Adam M. Alessio, Paul E. Kinahan, Kyle M. Champley, and James H. Caldwell. Attenuation-emission alignment in cardiac PET/CT based on consistency conditions. *Medical Physics*, **37**[3]:1191, 2010.

[2] Adam M Alessio, Steve Kohlmyer, Kelley Branch, Grace Chen, James Caldwell, and Paul Kinahan. Cine CT for attenuation correction in cardiac PET/CT. *Journal of nuclear medicine*, **48**[5]:794–801, May 2007.

[3] G Antoch, L S Freudenberg, T Beyer, A Bockisch, and J F Debatin. To enhance or not to enhance? F-18-FDG and CT contrast agents in dual-modality F-18-FDG PET/CT. *Journal of nuclear medicine*, **45**[1]:56S–65S, January 2004.

[4] G Antoch, L S Freudenberg, T Egelhof, J Stattaus, W Jentzen, J F Debatin, and A Bockisch. Focal tracer uptake: A potential artifact in contrast-enhanced dual-modality PET/CT scans. *Journal of nuclear medicine*, **43**[10]:1339–1342, October 2002.

[5] R D Badawi, P K Marsden, B F Cronin, J L Sutcliffe, and M N Maisey. Optimization of noise-equivalent count rates in 3D PET. *Physics in medicine and biology*, **41**[9]:1755–1776, September 1996.

[6] Wenjia Bai and Michael Brady. Motion correction and attenuation correction for respiratory gated PET images. *IEEE transactions on medical imaging*, **30**[2]:351–65, February 2011.

[7] R Bar-Shalom, N Yefremov, L Guralnik, D Gaitini, A Frenkel, A Kuten, H Altman, Z Keidar, and O Israel. Clinical performance of PET/CT in evaluation of cancer: Additional value for diagnostic Imaging and patient management. *Journal of Nuclear Medicine*, **44**[8]:1200–1209, August 2003.

[8] S F Barrington, J E Mackewn, P Schleyer, P K Marsden, N G Mikhaeel, W Qian, P Mouncey, P Patrick, B Popova, P Johnson, J Radford, and M J O'Doherty. Establishment of a UK-wide network to facilitate the acquisition of quality assured FDG-PET data for clinical trials in lymphoma. *Annals of oncology*, **22**[3]:739–45, March 2011.

[9] Valentino Bettinardi, Maria Picchio, Nadia Di Muzio, Luigi Gianolli, Maria Carla Gilardi, and Cristina Messa. Detection and compensation of organ/lesion motion using 4D-PET/CT respiratory gated acquisition techniques. *Radiotherapy and oncology*, **96**[3, SI]:311–316, September 2010.

[10] T Beyer, D W Townsend, T Brun, P E Kinahan, M Charron, R Roddy, J Jerin, J Young, L Byars, and R Nutt. A combined PET/CT scanner for clinical oncology. *Journal of nuclear medicine*, **41**[8]:1369–79, August 2000.

[11] Thomas Beyer, Gerald Antoch, Todd Blodgett, Lutz F Freudenberg, Tim Akhurst, and Stephan Mueller. Dual-modality PET/CT imaging: the effect of respiratory motion on combined image quality in clinical oncology. *European journal of nuclear medicine and molecular imaging*, **30**[4]:588–96, April 2003.

[12] Ronald Boellaard, Wim J G Oyen, Corneline J Hoekstra, Otto S Hoekstra, Eric P Visser, Antoon T Willemsen, Bertjan Arends, Fred J Verzijlbergen, Josee Zijlstra, Anne M Paans, Emile F I Comans, and Jan Pruim. The Netherlands protocol for standardisation and quantification of FDG whole body PET studies in multi-centre trials. *European Journal of Nuclear Medicine and Molecular Imaging*, **35**[12]:2320–2333, December 2008.

[13] Luc Boucher, Serge Rodrigue, Roger Lecomte, and François Bénard. Respiratory gating for 3-dimensional PET of the thorax: feasibility and initial results. *Journal of nuclear medicine*, **45**[2]:214–9, February 2004.

[14] Florian Buether, Iris Ernst, Mohammad Dawood, Peter Kraxner, Michael Schaefers, Otmar Schober, and Klaus P Schaefers. Detection of respiratory tumour motion using intrinsic list mode-driven gating in positron emission tomography. *European Journal of Nuclear Medicine and Molecular Imaging*, **37**[12]:2315–2327, December 2010.

[15] Ralph A Bundschuh, Axel Martínez-Moeller, Markus Essler, María-José Martínez, Stephan G Nekolla, Sibylle I Ziegler, and Markus Schwaiger. Postacquisition detection of tumor motion in the lung and upper abdomen using list-mode PET data: a feasibility study. *Journal of nuclear medicine*, **48**[5]:758–63, May 2007.

[16] C Burger, G Goerres, S Schoenes, A Buck, A H R Lonn, and G K von Schulthess. PET attenuation coefficients from CT images: experimental evaluation of the transformation of CT into PET 511-keV attenuation coefficients. *European Journal of Nuclear Medicine and Molecular Imaging*, **29**[7]:922–927, July 2002.

[17] Florian Büther, Mohammad Dawood, Lars Stegger, Frank Wübbeling, Michael Schäfers, Otmar Schober, and Klaus P Schäfers. List mode-driven cardiac and respiratory gating in PET. *Journal of nuclear medicine*, **50**[5]:674–81, May 2009.

[18] Greg Carnes, Stewart Gaede, Edward Yu, Jake Van Dyk, Jerry Battista, and Ting-Yim Lee. A fully automated non-external marker 4D-CT sorting algorithm using a serial cine scanning protocol. *Physics in Medicine and Biology*, **54**[7]:2049, 2009.

[19] M Charron, T Beyer, N N Bohnen, P E Kinahan, M Dachille, J Jerin, R Nutt, C C Meltzer, V Villemagne, and D W

Townsend. Image analysis in patients with cancer studied with a combined PET and CT scanner. *Clinical nuclear medicine*, **25**[11]:905–910, November 2000.

[20] S R Cherry, M Dahlbom, and E J Hoffman. 3D PET using a conventional multislice tomograph without septa. *Journal of Computer Assisted Tomography*, **15**[4]:655–668, 1991.

[21] S R Cherry, R P Woods, E J Hoffman, and J C Mazziotta. Improved detection of focal cerebral blood-flow changes using 3-dimensional positron emission tomography. *Journal of cerebral blood flow and metabolism*, **13**[4]:630–638, July 1993.

[22] Simon Cherry, Michael Phelps, and James Sorenson. *Physics in Nuclear Medicine*. Saunders, 3 edition, 2008.

[23] Pai-Chun Melinda Chi, Osama Mawlawi, Sadek A Nehmeh, Yusuf E Erdi, Peter A Balter, Dershan Luo, Radhe Mohan, and Tinsu Pan. Design of respiration averaged CT for attenuation correction of the PET data from PET/CT. *Medical Physics*, **34**[6]:2039–2047, June 2007.

[24] B.B. Chin, Y. Nakamoto, D.L. Kraitchman, L. Marshall, and R. Wahl. PET-CT evaluation of 2-deoxy-2-[18F] fluoro-D-glucose myocardial uptake: effect of respiratory motion. *Molecular Imaging & Biology*, **5**[2]:57–64, April 2003.

[25] Z H Cho, J K Chan, L Ericksson, M Singh, S Graham, N S Macdonald, and Y Yano. Positron ranges obtained from biomedically important positron-emitting radionuclides. *Journal of nuclear medicine*, **16**[12]:1174–1176, 1975.

[26] Se Young Chun, Timothy G Reese, Jinsong Ouyang, Bastien Guerin, Ciprian Catana, Xuping Zhu, Nathaniel M Alpert, and Georges El Fakhri. MRI-Based Nonrigid Motion Correction in Simultaneous PET/MRI. *Journal of Nuclear Medicine*, 2012.

[27] Christian Cohade, Medhat Osman, Laura N T Marshall, and Richard N T L Wahl. PET-CT: accuracy of PET and CT spatial registration of lung lesions. *European journal of nuclear medicine and molecular imaging*, **30**[5]:721–6, May 2003.

[28] A Collignon, F Maes, D Delaere, D Vandermeulen, P Suetens, and G Marchal. Automated multi-modality image registration based on information theory. *Information Processing in Medical Imaging*, pages 263–274, 1995.

[29] Russell Cook, Greg Carnes, T.-Y. Lee, and R.G. Wells. 4D CT for Respiratory Gated Attenuation Corrections in Canine Cardiac PET Imaging. In *IEEE Nuclear Science Symposium Conference Record, 2005*, **4**, pages 2408–2412, 2005.

[30] James W Cooley and John W Tukey. An algorithm for the machine calculation of complex Fourier series. *Math. Comp.*, **19**:297–301, 1965.

[31] Doumit Daou. Respiratory motion handling is mandatory to accomplish the high-resolution PET destiny. *European Journal of Nuclear Medicine and Molecular Imaging*, **35**[11]:1961–1970, 2008.

[32] M Dawood, F Buether, N Lang, X Jiang, and K P Schaefers. Transforming static CT in gated PET/CT studies to multiple respiratory phases. In H Tang, YY and Wang, SP and Lorette, G and Yeung, DS and Yan, editor, *18th International Conference on Pattern Recognition, Vol 1, Proceedings*, INTERNATIONAL CONFERENCE ON PATTERN RECOGNITION, pages 1026–1029, 2006.

[33] Mohammad Dawood, Florian Buther, Xiaoyi Jiang, and Klaus P Schafers. Respiratory motion correction in 3-D PET data with advanced optical flow algorithms. *IEEE transactions on medical imaging*, **27**[8]:1164–75, August 2008.

[34] Mohammad Dawood, Florian Buther, Norbert Lang, Otmar Schober, and Klaus P Schafers. Respiratory gating in positron emis-

sion tomography: A quantitative comparison of different gating schemes. *Medical Physics*, **34**[7]:3067, 2007.

[35] Mohammad Dawood, Norbert Lang, Xiaoyi Jiang, and Klaus P Schäfers. Lung motion correction on respiratory gated 3-D PET/CT images. *IEEE transactions on medical imaging*, **25**[4]:476–85, April 2006.

[36] B De Man, J Nuyts, P Dupont, G Marchal, and P Suetens. An iterative maximum-likelihood polychromatic algorithm for CT. *IEEE Transactions on medical imaging*, **20**[10]:999–1008, October 2001.

[37] Stephen E Derenzo. Mathematical Removal of Positron Range Blurring in High Resolution Tomography. *Nuclear Science, IEEE Transactions on*, **33**[1]:565–569, 1986.

[38] L Ekberg, O Holmberg, L Wittgren, G Bjelkengren, and T Landberg. What margins should be added to the clinical target volume in radiotherapy treatment planning for lung cancer? *Radiotherapy and oncology*, **48**[1]:71–7, July 1998.

[39] Yusuf E Erdi, Sadek a Nehmeh, Tinsu Pan, Alexander Pevsner, Kenneth E Rosenzweig, Gikas Mageras, Ellen D Yorke, Heiko Schoder, Wendy Hsiao, Olivia D Squire, Phil Vernon, Jonathan B Ashman, Hassan Mostafavi, Steven M Larson, and John L Humm. The CT motion quantitation of lung lesions and its impact on PET-measured SUVs. *Journal of nuclear medicine*, **45**[8]:1287–92, August 2004.

[40] Frederic H Fahey, Matthew R Palmer, Keith J Strauss, Robert E Zimmerman, Ramsey D Badawi, and S Ted Treves. Dosimetry and adequacy of CT-based attenuation correction for pediatric PET: Phantom study. *Radiology*, **243**[1]:96–104, April 2007.

[41] H Fayad, F Lamare, V Bettinardi, C Roux, and D Visvikis. Respiratory synchronized CT image generation from 40 PET acquisitions. In *IEEE Nuclear Science Symposium Conference Record*, pages 5488–5492, 2008.

[42] Hadi Fayad, Tinsu Pan, Jean Francois Clement, and Dimitris Visvikis. Technical Note: Correlation of respiratory motion between external patient surface and internal anatomical landmarks. *Medical Physics*, **38**[6]:3157, 2011.

[43] J A Fessler. ASPIRE 3.0 User's guide: A Sparse Iterative Reconstruction Library, Technical Report No. 293. Technical report, Communications & Signal Processing Laboratory, University of Michigan, 2006.

[44] A Gallamini, L Rigacci, F Merli, L Nassi, A Bosi, I Capodanno, S Luminari, U Vitolo, R Sancetta, E Iannitto, L Trentin, C Stelitano, S Tavera, A Biggi, A Castagnoli, A Versari, M Gregianin, E Pelosi, P Torchio, and A Levis. The predictive value of positron emission tomography scanning performed after two courses of standard therapy on treatment outcome in advanced stage Hodgkin's disease. *Haematologica-the hematology journal*, **91**[4]:475–481, April 2006.

[45] Andrea Gallamini, Martin Hutchings, Luigi Rigacci, Lena Specht, Francesco Merli, Mads Hansen, Caterina Patti, Annika Loft, Francesco Di Raimondo, Francesco D'Amore, Alberto Biggi, Umberto Vitolo, Caterina Stelitano, Rosario Sancetta, Livio Trentin, Stefano Luminari, Emilio Iannitto, Simonetta Viviani, Ivana Pierri, and Alessandro Levis. Early interim 2-{[}F-18]Fluoro-2-Deoxy-D-Glucose positron emission tomography is prognostically superior to international prognostic score in advanced-stage Hodgkin's lymphoma: A report from a joint Italian-Danish study. *Journal of clinical oncology*, **25**[24]:3746–3752, August 2007.

[46] R George, S S Vedam, T D Chung, V Ramakrishnan, and P J Keall. The application of the sinusoidal model to lung cancer patient respiratory motion. *Medical Physics*, **32**[9]:2850–2861, September 2005.

[47] Gerhard W Goerres, Ehab Kamel, Burkhardt Seifert, Cyrill Burger, Alfred Buck, Thomas F Hany, and Gustav K Von Schulthess. Accuracy of image coregistration of pulmonary lesions in

patients with non-small cell lung cancer using an integrated PET/CT system. *Journal of nuclear medicine*, **43**[11]:1469–75, November 2002.

[48] KL Gould, Tinsu Pan, and Catalin Loghin. diagnostic errors in cardiac PET/CT due to misregistration of CT attenuation and emission PET images: a definitive analysis of causes, consequences, and corrections. *Journal of Nuclear Medicine*, **48**[7]:1112, 2007.

[49] W A Hallett, P K Marsden, B F Cronin, and M J O'Doherty. Effect of corrections for blood glucose and body size on {[}F-18]FDG PET standardised uptake values in lung cancer. *European Journal of Nuclear Medicine*, **28**[7]:919–922, July 2001.

[50] T F Hany, H C Steinert, G W Goerres, A Buck, and G K von Schulthess. PET diagnostic accuracy: Improvement with in-line PET-CT system: Initial results. *Radiology*, **225**[2]:575–581, November 2002.

[51] Amy K Hara, Robert G Paden, Alvin C Silva, Jennifer L Kujak, Holly J Lawder, and William Pavlicek. Iterative Reconstruction Technique for Reducing Body Radiation Dose at CT: Feasibility Study. *American journal of roentgenology*, **193**[3]:764–771, September 2009.

[52] Jianfeng He, G J O'Keefe, G Jones, T Saunder, S J Gong, M Geso, and A M Scott. Evaluation of Geometrical Sensitivity for Respiratory Motion Gating by GATE and NCAT Simulation. In *Engineering in Medicine and Biology Society, 2007. EMBS 2007. 29th Annual International Conference of the IEEE*, pages 4165–4168, 2007.

[53] Jeremy D P Hoisak, Katharina E Sixel, Romeo Tirona, Patrick C F Cheung, and Jean-Philippe Pignol. Correlation of lung tumor motion with external surrogate indicators of respiration. *International Journal of Radiation Oncology*Biology*Physics*, **60**[4]:1298–1306, 2004.

[54] H M Hudson and R S Larkin. Accelerated image reconstruction using ordered subsets of projection data. *Medical Imaging, IEEE Transactions on*, **13**[4]:601–609, December 1994.

[55] M Hutchings, A Loft, M Hansen, L M Pedersen, T Buhl, J Jurlander, S Buus, S Keiding, F D'Amore, A M Boesen, A K Berthelsen, and L Specht. FDG-PET after two cycles of chemotherapy predicts treatment failure and progression-free survival in Hodgkin lymphoma. *Blood*, **107**[1]:52–59, January 2006.

[56] M Iatrou, S G Ross, R M Manjeshwar, and C W Stearns. A fully 3D iterative image reconstruction algorithm incorporatin data corrections. In JA Seibert, editor, *2004 IEEE Nuclear Science Symposium Conference Record, Vols 1-7*, IEEE NUCLEAR SCIENCE SYMPOSIUM - CONFERENCE RECORD, pages 2493–2497, 2004.

[57] Emmanuel Itti, Chieh Lin, Jehan Dupuis, Gaetano Paone, Daniela Capacchione, Alain Rahmouni, Corinne Haioun, and Michel Meignan. Prognostic Value of Interim (18)F-FDG PET in Patients with Diffuse Large B-Cell Lymphoma: SUV-Based Assessment at 4 Cycles of Chemotherapy. *Journal of Nuclear Medicine*, **50**[4]:527–533, April 2009.

[58] Malik E Juweid, Sigrid Stroobants, Otto S Hoekstra, Felix M Mottaghy, Markus Dietlein, Ali Guermazi, Gregory A Wiseman, Lale Kostakoglu, Klemens Scheidhauer, Andreas Buck, Ralph Naumann, Karoline Spaepen, Rodney J Hicks, Wolfgang A Weber, Sven N Reske, Markus Schwaiger, Lawrence H Schwartz, Josee M Zijlstra, Barry A Siegel, and Bruce D Cheson. Use of positron emission tomography for response assessment of lymphoma: Consensus of the Imaging Subcommittee of International Harmonization Project in lymphoma. *Journal of clinical oncology*, **25**[5]:571–578, February 2007.

[59] Ehab Kamel, Thomas F. Hany, Cyrill Burge. CT vs 68 Ge attenuation correction in a combined PET/CT system: evaluation of the effect of lowering the CT tube current. *European Journal of Nuclear Medicine and Molecular Imaging*, **29**[3]:346–350, March 2002.

[60] P J Keall, G Starkschall, H Shukla, K M Forster, V Ortiz, C W Stevens, S S Vedam, R George, T Guerrero, and R Mohan. Acquiring 4D thoracic CT scans using a multislice helical method. *Physics in medicine and biology*, **49**[10]:2053–2067, May 2004.

[61] Paul J. Keall, Gig S. Mageras, James M. Balter, Richard S. Emery, Kenneth M. Forster, Steve B. Jiang, Jeffrey M. Kapatoes, Daniel a. Low, Martin J. Murphy, Brad R. Murray, Chester R. Ramsey, Marcel B. Van Herk, S. Sastry Vedam, John W. Wong, and Ellen Yorke. The management of respiratory motion in radiation oncology report of AAPM Task Group 76. *Medical Physics*, **33**[10]:3874, 2006.

[62] Adam Leon Kesner and Claudia Kuntner. A new fast and fully automated software based algorithm for extracting respiratory signal from raw PET data and its comparison to other methods. *Medical Physics*, **37**[10]:5550–5559, October 2010.

[63] AL Kesner, RA Bundschuh, NC Detorie, M. Dahlbom, J. Czernin, and DHS Silverman. Respiratory gated pet derived from raw pet data. In *EEE Nuclear Science Symposium Conference Record, 2007. NSS'*, **4**, pages 2686–2691, 2007.

[64] Khawar Khurshid, Robert J McGough, and Kevin Berger. Automated cardiac motion compensation in PET/CT for accurate reconstruction of PET myocardial perfusion images. *Physics in medicine and biology*, **53**[20]:5705–18, October 2008.

[65] Paul Kinahan, L. MacDonald, Lydia Ng, Adam Alessio, P. Segars, B. Tsui, and S. Pathak. Compensating for patient respiration in PET/CT imaging with the registered and summed phases (RASP) procedure. In *Biomedical Imaging: Nano to Macro, 2006. 3rd IEEE International Symposium on*, pages 1104–1107, 2006.

[66] Paul E Kinahan, Bruce H Hasegawa, and Thomas Beyer. X-ray-based attenuation correction for positron emission tomography/computed

tomography scanners. *Seminars in nuclear medicine*, **33**[3]:166–79, July 2003.

[67] G J Klein, B W Reutter, M H Ho, J H Reed, and R H Huesman. Real-time system for respiratory-cardiac gating in positron tomography. *Nuclear Science, IEEE Transactions on*, **45**[4]:2139–2143, August 1998.

[68] Pascal Koepfli, T.F. Hany, C.A. Wyss, Mehdi Namdar, Cyrill Burger, A.V. Konstantinidis, Thomas Berthold, G.K. von Schulthess, and P.A. Kaufmann. CT attenuation correction for myocardial perfusion quantification using a PET/CT hybrid scanner. *Journal of Nuclear Medicine*, **45**[4]:537, 2004.

[69] Tommi Kokki, Hannu T Sipilä, Mika Teräs, Tommi Noponen, Nicolas Durand-Schaefer, Riku Klén, and Juhani Knuuti. Dual gated PET/CT imaging of small targets of the heart: method description and testing with a dynamic heart phantom. *Journal of nuclear cardiology*, **17**[1]:71–84, 2009.

[70] Gaber Komar, Mika Teras, Marko Seppanen, Jussi Hirvonen, Tero Vahlberg, Jorgen Bergman, and Heikki Minn. Comparison of 2D and 3D performance for FDG PET with different acquisition times in oncological patients. *Nuclear Medicine Communications*, **30**[1]:16–24, January 2009.

[71] F Lamare, M J Ledesma Carbayo, T Cresson, G Kontaxakis, A Santos, C Cheze Le Rest, A J Reader, and D Visvikis. List-mode-based reconstruction for respiratory motion correction in PET using non-rigid body transformations. *Physics in medicine and biology*, **52**[17]:5187–204, September 2007.

[72] F Lamare, M Teras, T Kokki, H Fayad, O Rimoldi, P G Camici, J Knuuti, and D Visvikis. Correction of Respiratory Motion in Dual Gated Cardiac Imaging in PET/CT. In *2008 IEEE Nuclear Science Symposium and Medical Imaging Conference (2008 NSS/MIC), vols 1-9*, IEEE

NUCLEAR SCIENCE SYMPOSIUM - CONFERENCE RECORD, pages 4530–4535, 2009.

[73] K M Langen and D T Jones. Organ motion and its management. *International journal of radiation oncology, biology, physics*, **50**[1]:265–78, May 2001.

[74] D Lardinois, W Weder, T F Hany, E M Kamel, S Korom, B Seifert, G K von Schulthess, and H C Steinert. Staging of non-small-cell lung cancer with integrated positron-emission tomography and computed tomography. *New England Journal of Medicine*, **348**[25]:2500–2507, June 2003.

[75] C Lartizien, C Comtat, P E Kinahan, N Ferriera, B Bendriem, and R Trebossen. Optimization of injected dose based on noise equivalent count rates for 2-and 3-dimensional whole-body PET. *Journal of Nuclear Medicine*, **43**[9]:1268–1278, September 2002.

[76] Ruijiang Li, John H Lewis, Laura I Cerviño, and Steve B Jiang. 4D CT sorting based on patient internal anatomy. *Physics in Medicine and Biology*, **54**[15]:4821, 2009.

[77] Tianfang Li, Brian Thorndyke, Eduard Schreibmann, Yong Yang, and Lei Xing. Model-based image reconstruction for four-dimensional PET. *Medical Physics*, **33**[5]:1288, 2006.

[78] Chieh Lin, Emmanuel Itti, Corinne Haioun, Yolande Petegnief, Alain Luciani, Jehan Dupuis, Gaetano Paone, Jean-Noel Talbot, Alain Rahmouni, and Michel Meignan. Early F-18-FDG PET for prediction of prognosis in patients with diffuse large B-cell lymphoma: SUV-based assessment versus visual analysis. *Journal of Nuclear Medicine*, **48**[10]:1626–1632, October 2007.

[79] Chi Liu, Adam Alessio, Larry Pierce, Kris Thielemans, Scott Wollenweber, Alexander Ganin, and Paul Kinahan. Quiescent period respiratory gating for PET/CT. *Medical Physics*, **37**[9]:5037, 2010.

[80] Chi Liu, Larry A Pierce, Adam M Alessio, and Paul E Kinahan. The impact of respiratory motion on tumor quantification and delineation in static PET/CT imaging. *Physics in medicine and biology*, **54**[24]:7345–62, December 2009.

[81] L Livieratos, K Rajappan, L Stegger, K Schafers, D L Bailey, and P G Camici. Respiratory gating of cardiac PET data in list-mode acquisition. *European Journal of Nuclear Medicine and Molecular Imaging*, **33**[5]:584–588, May 2006.

[82] M A Lodge, R D Badawi, R Gilbert, P E Dibos, and B R Line. Comparison of 2-dimensional and 3-dimensional acquisition for (18)F-FDG PET oncology studies performed on an LSO-based scanner. *Journal of Nuclear Medicine*, **47**[1]:23–31, January 2006.

[83] M A Lodge, J D Lucas, P K Marsden, B F Cronin, M J O'Doherty, and M A Smith. A PET study of (18)FDG uptake in soft tissue masses. *European Journal of Nuclear Medicine*, **26**[1]:22–30, January 1999.

[84] D A Low, M Nystrom, E Kalinin, P Parikh, J F Dempsey, J D Bradley, S Mutic, S H Wahab, T Islam, G Christensen, D G Politte, and B R Whiting. A method for the reconstruction of four-dimensional synchronized CT scans acquired during free breathing. *Medical Physics*, **30**[6]:1254–1263, June 2003.

[85] Josef Machac, Stephen L Bacharach, Timothy M Bateman, Jeroen J Bax, Robert Beanlands, Frank Bengel, Steven R Bergmann, Richard C Brunken, James Case, Dominique Delbeke, Marcelo F DiCarli, Ernest V Garcia, Richard a Goldstein, Robert J Gropler, Mark Travin, Randolph Patterson, and Heinrich R Schelbert. Positron emission tomography myocardial perfusion and glucose metabolism imaging. *Journal of nuclear cardiology*, **13**[6]:e121–51, November 2006.

[86] S Malone, J M Crook, W S Kendal, and J Szanto. Respiratory-induced prostate motion: quantification and characterization. *International journal of radiation oncology, biology, physics*, **48**[1]:105–9, August 2000.

[87] Ravindra Manjeshwar, Xiaodong Tao, Evren Asma, and Kris Thielemans. Motion compensated image reconstruction of respiratory gated PET/CT. In *Biomedical Imaging: Nano to Macro, 2006. 3rd IEEE International Symposium on*, number 2, pages 674–677, 2006.

[88] A. Martinez-Möller, Michael Souvatzoglou, Nassir Navab, Markus Schwaiger, and S.G. Nekolla. Artifacts from misaligned CT in cardiac perfusion PET/CT studies: frequency, effects, and potential solutions. *Journal of Nuclear Medicine*, **48**[2]:188, 2007.

[89] J R McClelland, S Hughes, M Modat, A Qureshi, S Ahmad, D B Landau, S Ourselin, and D J Hawkes. Inter-fraction variations in respiratory motion models. *Physics in medicine and biology*, **56**[1]:251–272, January 2011.

[90] Jamie R McClelland, Jane M Blackall, Segolene Tarte, Adam C Chandler, Simon Hughes, Shahreen Ahmad, David B Landau, and David J Hawkes. A continuous 4D motion model from multiple respiratory cycles for use in lung radiotherapy. *Medical Physics*, **33**[9]:3348–3358, September 2006.

[91] C K Mckibben and N V Reo. A piezoelectric respiratory monitor for invivo NMR. *Magnetic resonance in medicine*, **27**[2]:338–342, October 1992.

[92] Sarah J McQuaid, Tryphon Lambrou, and Brian F Hutton. A novel method for incorporating respiratory-matched attenuation correction in the motion correction of cardiac PET-CT studies. *Physics in medicine and biology*, **56**[10]:2903–15, May 2011.

[93] SJ McQuaid. Sources of attenuation-correction artefacts in cardiac PET/CT and SPECT/CT. *European journal of nuclear medicine and*, pages 1117–1123, 2008.

[94] L Le Meunier, R Maass-Moreno, and Bacharach Stephen Carrasquillo Jorge, Dieckmann William. PET/CT imaging: effect of respiratory motion on apparent myocardial uptake. *Journal of nuclear cardiology*, **13**[6]:821–830, 2006.

[95] N G Mikhaeel, M Hutchings, P A Fields, M J O'Doherty, and A R Timothy. FDG-PET after two to three cycles of chemotherapy predicts progression-free and overall survival in high-grade non-Hodgkin lymphoma. *Annals of Oncology*, **16**[9]:1514–1523, September 2005.

[96] Marc Modat, Gerard R Ridgway, Zeike A Taylor, Manja Lehmann, Josephine Barnes, David J Hawkes, Nick C Fox, and Sebastien Ourselin. Fast free-form deformation using graphics processing units. *Computer Methods and Programs in Biomedicine*, **98**[3, SI]:278–284, June 2010.

[97] C. C. a. Nagel, G. Bosmans, a. L. a. J. Dekker, M. C. Ollers, D. K. M. De Ruysscher, P. Lambin, a. W. H. Minken, N. Lang, and K. P. Schafers. Phased attenuation correction in respiration correlated computed tomography/positron emitted tomography. *Medical Physics*, **33**[6]:1840, 2006.

[98] S A Nehmeh, Y E Erdi, C C Ling, K E Rosenzweig, O D Squire, L E Braban, E Ford, K Sidhu, G S Mageras, S M Larson, and J L Humm. Effect of respiratory gating on reducing lung motion artifacts in PET imaging of lung cancer. *Medical Physics*, **29**[3]:366–371, March 2002.

[99] S. A. Nehmeh, Y. E. Erdi, T. Pan, A. Pevsner, K. E. Rosenzweig, E. Yorke, G. S. Mageras, H. Schoder, Phil Vernon, O. Squire, H. Mostafavi, S. M. Larson, and J. L. Humm. Four-dimensional (4D) PET/CT imaging of the thorax. *Medical Physics*, **31**[12]:3179, 2004.

[100] S. A. Nehmeh, Y. E. Erdi, T. Pan, E. Yorke, G. S. Mageras, K. E. Rosenzweig, H. Schoder, H. Mostafavi, O. Squire, A. Pevsner,

S. M. Larson, and J. L. Humm. Quantitation of respiratory motion during 4D-PET/CT acquisition. *Medical Physics*, **31**[6]:1333, 2004.

[101] S A Nehmeh, A A Haj-Ali, C Qing, C Stearns, H Kalaigian, S Kohlmyer, H Schoder, A Y Ho, S M Larson, and J L Humm. A novel respiratory tracking system for smart-gated PET acquisition. *Medical Physics*, **38**[1]:531–538, January 2011.

[102] SA Nehmeh, YE Erdi, and GSP Meirelles. Deep-inspiration breath-hold PET/CT of the thorax. *Journal of Nuclear*, **48**[1]:22–26, 2007.

[103] Sadek a Nehmeh and Yusuf E Erdi. Respiratory motion in positron emission tomography/computed tomography: a review. *Seminars in nuclear medicine*, **38**[3]:167–76, May 2008.

[104] Sadek a Nehmeh, Yusuf E Erdi, Clifton C Ling, Kenneth E Rosenzweig, Heiko Schoder, Steve M Larson, Homer a Macapinlac, Olivia D Squire, and John L Humm. Effect of respiratory gating on quantifying PET images of lung cancer. *Journal of nuclear medicine*, **43**[7]:876–81, July 2002.

[105] Jonathon a. Nye, Fabio Esteves, and John R. Votaw. Minimizing artifacts resulting from respiratory and cardiac motion by optimization of the transmission scan in cardiac PET/CT. *Medical Physics*, **34**[6]:1901, 2007.

[106] Medhat M Osman, Christian Cohade, Yuji Nakamoto, and Richard L Wahl. Respiratory motion artifacts on PET emission images obtained using CT attenuation correction on PET-CT. *European journal of nuclear medicine and molecular imaging*, **30**[4]:603–6, April 2003.

[107] Cihat Ozhasoglu and Martin J Murphy. Issues in respiratory motion compensation during external-beam radiotherapy. *International Journal of Radiation Oncology*Biology*Physics*, **52**[5]:1389–1399, 2002.

[108] Tinsu Pan, Ting-Yim Lee, Eike Rietzel, and George T. Y. Chen. 4D-CT imaging of a volume influenced by respiratory motion on multi-slice CT. *Medical Physics*, **31**[2]:333, 2004.

[109] Tinsu Pan, Osama Mawlawi, Dershan Luo, Hui H Liu, Pai-Chun M Chi, Martha V Mar, Gregory Gladish, Mylene Truong, Jeremy Erasmus Jr., Zhongxing Liao, and H A Macapinlac. Attenuation correction of PET cardiac data with low-dose average CT in PET/CT. *Medical Physics*, **33**[10]:3931–3938, October 2006.

[110] Tinsu Pan, Osama Mawlawi, Sadek a Nehmeh, Yusuf E Erdi, Dershan Luo, Hui H Liu, Richard Castillo, Radhe Mohan, Zhongxing Liao, and H a Macapinlac. Attenuation correction of PET images with respiration-averaged CT images in PET/CT. *Journal of nuclear medicine*, **46**[9]:1481–7, September 2005.

[111] A Pevsner, S A Nehmeh, J L Humm, G S Mageras, and Y E Erdi. Effect of motion on tracer activity determination in CT attenuation corrected PET images: A lung phantom study. *Medical Physics*, **32**[7]:2358–2362, July 2005.

[112] Christian Plathow, Sebastian Ley, Christian Fink, Michael Puderbach, Waldemar Hosch, Astrid Schmähl, Jürgen Debus, and Hans-Ulrich Kauczor. Analysis of intrathoracic tumor mobility during whole breathing cycle by dynamic MRI. *International Journal of Radiation Oncology*Biology*Physics*, **59**[4]:952–959, 2004.

[113] Irene Polycarpou, Charalampos Tsoumpas, and Paul K. Marsden. Statistical evaluation of PET motion correction methods using MR derived motion fields. *2011 IEEE Nuclear Science Symposium Conference Record*, [1]:3579–3585, October 2011.

[114] Falk Pönisch, Christian Richter, Uwe Just, and Wolfgang Enghardt. Attenuation correction of four dimensional (4D) PET using phase-correlated 4D-computed tomography. *Physics in medicine and biology*, **53**[13]:N259–68, July 2008.

[115] Feng Qiao, Tinsu Pan, John W Clark, and Osama R Mawlawi. A motion-incorporated reconstruction method for gated PET studies. *Physics in medicine and biology*, **51**[15]:3769–83, August 2006.

[116] Eike Rietzel, Tinsu Pan, and George T. Y. Chen. Four-dimensional computed tomography: Image formation and clinical protocol. *Medical Physics*, **32**[4]:874, 2005.

[117] C S Ross, D H Hussey, E C Pennington, W Stanford, and J F Doornbos. Analysis of movement of intrathoracic neoplasms using ultrafast computerized-tomography. *International Journal of Radiation Oncology*Biology*Physics*, **18**[3]:671–677, March 1990.

[118] D Rueckert, L I Sonoda, C Hayes, D L G Hill, M O Leach, and D J Hawkes. Nonrigid registration using free-form deformations: Application to breast MR images. *IEEE Transactions on medical imaging*, **18**[8]:712–721, August 1999.

[119] Christian Schaller, Jochen Penne, and Joachim Hornegger. Time-of-flight sensor for respiratory motion gating. *Medical Physics*, **35**[7]:3090–3093, 2008.

[120] P Schleyer. *Respiratory motion correction in nuclear medicine imaging.* University of Melbourne, Dept. of Electrical and Electronic Engineering Science, 2003.

[121] H Schoder, Y E Erdi, S M Larson, and H W D Yeung. PET/CT: a new imaging technology in nuclear medicine. *European Journal of Nuclear Medicine and Molecular Imaging*, **30**[10]:1419–1437, October 2003.

[122] W P Segars, B M W Tsui, A J Da Silva, and L Shao. CT-PET image fusion using the 4D NCAT phantom with the purpose of attenuation correction. In S Metzler, editor, *2002 IEEE Nuclear science symposium, conference record, vols 1-3*, IEEE NUCLEAR SCIENCE SYMPOSIUM - CONFERENCE RECORD, pages 1775–1779, 2003.

[123] Yvette Seppenwoolde, Hiroki Shirato, Kei Kitamura, Shinichi Shimizu, Marcel van Herk, Joos V Lebesque, and Kazuo Miyasaka. Precise and real-time measurement of 3D tumor motion in lung due to breathing and heartbeat, measured during radiotherapy. *International journal of radiation oncology, biology, physics*, **53**[4]:822–34, July 2002.

[124] L K Shankar, J M Hoffman, S Bacharach, M M Graham, J Karp, A A Lammertsma, S Larson, D A Mankoff, B A Siegel, A den Abbeele, J Yap, and D Sullivan. Consensus recommendations for the use of F-18-FDG PET as an indicator of therapeutic response in patients in national cancer institute trials. *Journal of nuclear medicine*, **47**[6]:1059–1066, June 2006.

[125] M J Siegel, B Schmidt, D Bradley, C Suess, and C Hildebolt. Radiation dose and image quality in pediatric CT: Effect of technical factors and phantom size and shape. *Radiology*, **233**[2]:515–522, November 2004.

[126] D A Silbersweig, E Stern, C D Frith, C Cahill, L Schnorr, S Grootoonk, T Spinks, J Clark, R Frackowiak, and T Jones. Detection of 30-second cognitive activations in single subjects with positron emission tomography - a new low-dose (H2O)-O-15 regional cerebral blood-flow 3-dimensional imaging technique. *Journal of cerebral blood flow and Metabolism*, **13**[4]:617–629, July 1993.

[127] P J Slomka, H Nishina, D S Berman, X P Kang, C Akincioglu, J D Friedman, S W Hayes, U E Aladl, and G Germano. "Motion-frozen" display and quantification of myocardial perfusion. *Journal of nuclear medicine*, **45**[7]:1128–1134, July 2004.

[128] Michael Souvatzoglou, Frank Bengel, Raymonde Busch, Coletta Kruschke, Helga Fernolendt, Denise Lee, Markus Schwaiger, and Stephan G Nekolla. Attenuation correction in cardiac PET/CT with three different CT protocols: a comparison with conventional PET. *European journal of nuclear medicine and molecular imaging*, **34**[12]:1991–2000, December 2007.

[129] I Suramo, M Paivansalo, and V Myllyla. Cranio-caudal movements of the liver, pancreas and kidneys in respiration. *Acta Radiologica-Diagnosis*, **25**[2]:129–131, 1984.

[130] S Tarte, J McClelland, S Hughes, J Blackall, D Landau, and D Hawkes. A non-contact method for the acquisition of breathing signals that enable distinction between abdominal and thoracic breathing. *Radiotherapy and Oncology*, **81**[1], 2006.

[131] Mika Teras, Tommi Kokki, Nicolas Durand-Schaefer, Tommi Noponen, Mikko Pietila, Jan Kiss, Erika Hoppela, Hannu T Sipila, and Juhani Knuuti. Dual-gated cardiac PET-Clinical feasibility study. *European Journal of Nuclear Medicine and Molecular Imaging*, **37**[3]:505–516, March 2010.

[132] M M Terpogossian, S R Bergmann, and B E Sobel. Influence of cardiac and respiratory motion on tomographic reconstructions of the heart - implications for quantitative nuclear cardiology. *Journal of Computer Assisted Tomography*, **6**[6]:1148–1155, 1982.

[133] Kris Thielemans and RM Manjeshwar. Lesion detectability in motion compensated image reconstruction of respiratory gated PET/CT. *Record, 2006. IEEE*, **2**[6]:3278–3282, 2006.

[134] Kris Thielemans, Shailendra Rathore, Fredrik Engbrant, and Pasha Razifar. Device-less gating for PET/CT using PCA. In *Nuclear Science Symposium and Medical Imaging Conference (NSS/MIC), 2011 IEEE*, pages 3904–3910, 2011.

[135] Charalampos Tsoumpas, Jane E Mackewn, Philip Halsted, Andrew P King, Christian Buerger, John J Totman, Tobias Schaeffter, and Paul K Marsden. Simultaneous PET-MR acquisition and MR-derived motion fields for correction of non-rigid motion in PET. *Annals of Nuclear Medicine*, **24**[10]:745–750, December 2010.

[136] S S Vedam, P J Keall, V R Kini, H Mostafavi, H P Shukla, and R Mohan. Acquiring a four-dimensional computed tomography dataset

using an external respiratory signal. *Physics in medicine and biology*, **48**[1]:45–62, January 2003.

[137] Linda M Velasquez, Ronald Boellaard, Georgia Kollia, Wendy Hayes, Otto S Hoekstra, Adriaan A Lammertsma, and Susan M Galbraith. Repeatability of F-18-FDG PET in a Multicenter Phase I Study of Patients with Advanced Gastrointestinal Malignancies. *Journal of Nuclear Medicine*, **50**[10]:1646–1654, October 2009.

[138] F R Verdun, D Lepori, P Monnin, J F Valley, P Schnyder, and F Gudinchet. Management of patient dose and image noise in routine pediatric CT abdominal examinations. *European Radiology*, **14**[5]:835–841, May 2004.

[139] Paul Viola and William M Wells III. Alignment by Maximization of Mutual Information. *International Journal of Computer Vision*, **24**[2]:137–154, 1997.

[140] D Visvikis, O Barret, T D Fryer, F Lamare, A Turzo, Y Bizais, and C C Le Rest. Evaluation of respiratory motion effects in comparison with other parameters affecting PET image quality. In *Nuclear Science Symposium Conference Record, 2004 IEEE*, **6**, pages 3668 – 3672 Vol. 6, 2004.

[141] D Visvikis, D C Costa, I Croasdale, a H R Lonn, J Bomanji, S Gacinovic, and P J Ell. CT-based attenuation correction in the calculation of semi-quantitative indices of [18F]FDG uptake in PET. *European journal of nuclear medicine and molecular imaging*, **30**[3]:344–53, March 2003.

[142] D Visvikis, D Griffiths, D C Costa, J Bomanji, and P J Ell. Clinical evaluation of 2D versus 3D whole-body PET image quality using a dedicated BGO PET scanner. *European Journal of Nuclear Medicine and Molecular Imaging*, **32**[9]:1050–1056, September 2005.

[143] Dimitris Visvikis, Olivier Barret, Tim Fryer, Alexandre Turzo, Frederic Lamare, C. Cheze Le Rest, and Yves Bizais. A

posteriori respiratory motion gating of dynamic PET images. In *Nuclear Science Symposium Conference Record, 2003 IEEE*, **5**, pages 3276–3280, 2003.

[144] Gerhard W. Goerres, Ehab Kamel, Thai-Nia H. PET-CT image co-registration in the thorax: influence of respiration. *European Journal of Nuclear Medicine and Molecular Imaging*, **29**[3]:351–360, March 2002.

[145] Y Wang, S J Riederer, and R L Ehman. Respiratory motion of the heart: kinematics and the implications for the spatial resolution in coronary imaging. *Magnetic resonance in medicine*, **33**[5]:713–9, May 1995.

[146] Y Wang, E Vidan, and G W Bergman. Cardiac motion of coronary arteries: Variability in the rest period and implications for coronary MR angiography. *Radiology*, **213**[3]:751–758, December 1999.

[147] R Glenn Wells, Terrence D Ruddy, Rob A DeKemp, Jean N DaSilva, and Rob S Beanlands. Single-phase CT aligned to gated PET for respiratory motion correction in cardiac PET/CT. *Journal of nuclear medicine*, **51**[8]:1182–90, August 2010.

[148] Huanmei Wu, Qingya Zhao, Ross I Berbeco, Seiko Nishioka, Hiroki Shirato, and Steve B Jiang. Gating based on internal/external signals with dynamic correlation updates. *Physics in Medicine and Biology*, **53**[24]:7137, 2008.

[149] Ting Xia, Adam M Alessio, Bruno De Man, Ravindra Manjeshwar, Evren Asma, and Paul E Kinahan. Ultra-low dose CT attenuation correction for PET/CT. *Physics in medicine and biology*, **57**[2]:309–28, January 2012.

[150] Rongping Zeng, Jeffrey A. Fessler, James M. Balter, and Peter A. Balter. Iterative sorting for four-dimensional CT images based on internal anatomy motion. *Medical Physics*, **35**[3]:917, 2008.